Incoherent Silicon Integrated Terahertz Arrays: A Study on Applications, Performance, and Limitations

BERGISCHE
UNIVERSITÄT
WUPPERTAL

Dissertation

Submitted in partial fulfillment of the requirements for the degree of

Doktor der Ingenieurswissenschaften

at the

University of Wuppertal, Germany

School of Electrical, Information, and Media Engineering

by

Robin Zatta

from Essen, Germany

October 7, 2021

The PhD thesis can be quoted as follows:

urn:nbn:de:hbz:468-20220207-094124-8
[http://nbn-resolving.de/urn/resolver.pl?urn=urn%3Anbn%3Ade%3Ahbz%3A468-20220207-094124-8]

DOI: 10.25926/gyk8-qp20
[https://doi.org/10.25926/gyk8-qp20]

Contents

Declaration

I, Robin Zatta, herewith declare that I have produced this thesis without the prohibited assistance of third parties and without making use of aids other than those specified; notions taken over directly or indirectly from other sources have been identified as such. This work has not previously been presented in identical or similar form to any other German or foreign examination board.

The thesis work was conducted from 2017–2021, under the supervision of Prof. Dr. rer. nat. Ullrich R. Pfeiffer at the Institute for High-Frequency and Communication Technology, University of Wuppertal, Germany. This work was partially funded by Deutsche Forschungsgemeinschaft (DFG) under SFB/Transregio MARIE projects C04 and C08 as well as individual grant projects "TErahertz Active Source ARrays (TEASAR)," "Silicon Integrated Smart Terahertz Source Arrays for Reciprocal Imaging (SI-STAR)," and "Spatially-Mapped Mobile Terahertz Spectroscopy (T-MAP)." In addition, Ticwave GmbH, Wuppertal, Germany, provided a CMOS THz camera for numerous experiments.

Acknowledgements

First and foremost, I express my sincere gratitude to my PhD advisor, Prof. Ullrich R. Pfeiffer, for giving me the opportunity to pursue my doctoral thesis at IHCT. This PhD and the associated research would not have been possible without his great guidance and the outstanding infrastructure he created regarding his lab.

In addition, I would like to thank my associate advisor, Prof. Anton Kummert, from the University of Wuppertal, who co-examined this thesis and gave me valuable suggestions for improving some aspects of it.

Special thanks go to Dr. Ritesh Jain and Dr. Daniel Headland. Dr. Ritesh Jain was my advisor during my Master-Thesis at IHCT and opened my eyes toward THz research. I have to say I learned a lot from him regarding lab work, scientific writing, and so much more. Dr. Daniel Headland had a six-month stay in my early days at our institute. During this time, he should have equipped me with the necessary knowledge required for almost everything related to my PhD and some ideas that finally ended up in my thesis.

I also thank the other colleagues and former members of the IHCT group with whom I have worked. These include (in no particular order) Martina Grabowski, Dr. Pedro Rodríguez, Marcel Andree, Eamal Ashna, Utpal Kalita, Dr. Dominika Warmowska, Dr. Thomas Schulz, Dr. Vishal S. Jagtap, Dr. Laven Mavarani, Hans M. Keller, Marc Hannapel, Dr. Philipp Hillger, Thomas Bücher, Dr. Stefan Malz, and Wolfgang Förster. Many of them have contributed directly or indirectly to my PhD work. Thomas Bücher, Dr. Phillip Hillger, and Dr. Stefan Malz helped me learn the RF design tools. Eamal helped me in some of the measurement tasks.

Last but not least, I thank DFG for providing financial support for this research and Ticwave GmbH Wuppertal, Germany, for providing the CMOS THz camera.

Abstract

The terahertz (THz) range situates between microwaves (below 0.1 THz) and optics (above 10 THz). Although THz waves have several unique properties that make them attractive for numerous potential uses, such as their ability to see through dielectric materials, the lack of efficient technologies makes the THz range the most underexploited frequency range. Established systems operating at THz frequencies are costly and bulky, limiting their utility to laboratory environments. Alternative solutions to massively reduce the cost and size of functional THz devices are needed to expedite this frequency band toward practical applications. Electronic integrated circuits lend themselves to miniaturization and mass production. Silicon process technologies, for example, have enabled the fabrication yield required to realize THz arrays of many incoherent sources or detectors on a single chip. The overarching aim of this thesis is to explore such devices for THz active imaging, THz spectroscopy, and THz antenna measurements to offer cost-effective and compact alternatives for these disciplines that may reach broader societies.

These devices are typically backside-coupled to a silicon lens to sample or illuminate an angular field of view. While devices based on incoherent sources are key components in overcoming the limitations of radiation power in the THz range, devices based on incoherent detectors are cameras that allow forming a THz image without the necessity for mechanical scanning. It was not fully understood how their combined far-field radiation pattern affects their performance in THz active imaging before this thesis. The original contribution of this thesis to knowledge is, on the one hand, to understand this aspect in full detail. It is derived how to operate these devices to achieve optimal performance in producing highly resolved images, which is crucial to offer a cost-effective and compact alternative for real-time THz active imaging applications. In this regard, a novel illumination concept based on THz source arrays is introduced. Beyond that, it is demonstrated how incoherent THz cameras can be repurposed for THz spectroscopy and how to use them for THz antenna measurements, thereby offering low-cost and compact alternatives for these disciplines.

With respect to the generation of highly resolved THz images, this thesis demonstrates that so-called super-resolution imaging can be leveraged to achieve a diffraction-limited spatial resolution. In a super-resolution imaging experiment performed at 0.652 THz with a CMOS camera that uses a 15-mm diameter lens, a spatial resolution of 1.43 mm was achieved at an illumination aperture of 50 mm. The achievable spatial resolution scales with the imaging aperture, with smaller ones being beneficial to resolution. In this context, the frequency-dependent limits in angular resolution are derived. This understanding is applied to a THz dispersive spectroscope that combines a CMOS THz camera and dispersive optics. This type of optics splits a broadband THz signal into its colors and assigns each frequency to a specific camera pixel. The average spectral resolution improved from 68.3 GHz to 34.2 GHz (factor of 2) within 0.75–0.9 THz, while the average frequency accuracy improved from 30 GHz to 1.65 GHz (factor of 18.2). A novel measurement concept for determining the far-field characteristics of THz radiation sources at a compact range using such cameras is also presented. The directivity, half-power beamwidth, and radiation power of a THz source with known far-field characteristics were determined within a root mean square accuracy of 0.85 dB, 1.1°, and 0.7 µW, respectively, in an experiment performed over a large frequency range of 0.6–1.1 THz. Furthermore, it is demonstrated how to operate an incoherent silicon integrated THz source array as a diffuse, uniform-intensity illumination source, thereby realizing a proof of concept using a device that radiates a record power of 10.3 dBm at 0.42 THz; the THz range lacked uniform illumination sources required to realize a constant dynamic range over the imaging plane. Based on this and a CMOS THz camera, an all-electronic, cost-effective, and compact solution for high-performance THz active imaging with real-time capabilities has been realized.

The contributions of this thesis pave the way for the realization of a low-cost, compact alternative for broadband THz spectrometry, which offers a means to inspect already packaged goods for material properties. To this end, the presented concept of repurposing an incoherent THz camera for spectroscopy must be expanded by a suitable THz multicolor source. Contemporary devices suffer from low radiation power. The illumination concept to create uniform illumination may be used to realize arrays of THz multicolor sources with greater overall radiation power combined into a single far-field beam.

Zusammenfassung

Die Anzahl praktischer Anwendungen für Terahertz(THz)-Strahlung, welche im Grenzbereich zwischen dem Mikrowellenbereich (unter 0,1 THz) und dem optischen Bereich (über 10 THz) liegt, sind heute noch stark limitiert. Etablierte Systeme werden aufgrund von Größe und Kosten überwiegend in Laboren eingesetzt. Es werden dringend kostengünstige und kompakte Lösungen benötigt, um "THz" praxistauglich einzusetzen, denn diese Strahlung bietet einige interessante Eigenschaften, wie z. B. die Fähigkeit, eine ganze Reihe von Materialien durchleuchten zu können. In Anbetracht dessen bieten elektronische integrierte Schaltungen, welche eine Massenproduktion sowie die Realisierung kompakter Lösungen erlauben, eine attraktive Alternative. Beispielsweise bringen Silizium-Technologien die erforderliche Fertigungsausbeute mit sich, um große THz-Detektor- und THz-Quell-Arrays auf einem einzigen Chip zu integrieren. Das übergeordnete Ziel dieser Thesis besteht darin, solche Komponenten in Hinblick auf deren Anwendbarkeit in der THz-Aktiv-Bildgebung, THz-Spektroskopie und THz-Antennenmessungen zu verstehen, um kostengünstige und kompakte Alternativen für diese Disziplinen zu realisieren und somit die Praxistauglichkeit von THz zu erhöhen.

Diese beiden Typen von THz-Arrays sind Komponenten, die ursprünglich für die THz-Aktiv-Bildgebung entwickelt wurden; Detektor-basierte Geräte, d. h. THz-Kameras, zum Aufnehmen eines Bildes und Quell-basierte Geräte zum Beleuchten eines Objekts. Hierbei ermöglicht die Kopplung an ein Objektiv die Abtastung bzw. Beleuchtung eines bestimmten Sichtfeldes. Als Objektiv werden üblicherweise Silizium-Linsen eingesetzt. Vor dieser Thesis war es weitestgehend unklar, wie sich das Abstrahlverhalten solcher Silizium-Linsen-gekoppelten THz-Arrays auf die Performanz in der mit ihnen realisierten Applikationen in der THz-Aktiv-Bildung auswirkt. Der wissenschaftliche Beitrag dieser Arbeit besteht zum einen darin, diesen Aspekt in all seinen Facetten zu verstehen. Daraus wird abgeleitet, wie solche Komponenten betrieben werden müssen, um eine vollelektronische, kompakte und kostengünstige Alternative für die Echtzeit-Bildgebung mit hoher

Performanz—hinsichtlich des Produzierens eines hochauflösenden THz-Bildes—zu realisieren. Im Zuge dessen wird ein neues Beleuchtungskonzept auf Basis von THz-Quell-Arrays eingeführt. Darüber hinaus wird auch gezeigt, wie THz-Kameras für die THz-Spektroskopie und THz-Antennenmessungen eingesetzt werden können, um auch in diesen Bereichen eine kompakte und kostengünstige Alternative zu bieten.

In Hinblick auf die Generierung hochauflösender THz-Bilder wird in dieser Thesis gezeigt, dass mit Linsen-integrierten THz-Kameras durch den Einsatz sog. superauflösender Bildgebungsverfahren immer eine beugungsbegrenzte Raumauflösung erzielt werden kann. Eine CMOS-THz-Kamera mit einer 15-mm Linse erzielte bei einer Bildfläche von 50 mm Durchmesser eine Raumauflösung von 1.43 mm in einem Experiment bei 0.652 THz. Dabei skaliert die erreichbare Auflösung mit der Bildfläche, wobei kleinere Bildflächen vorteilhaft sind in puncto Auflösung. In dem Zuge werden auch die allgemeinen Winkelauflösungsgrenzen solcher Kameras ermittelt. Das gewonnene Verständnis wird dann auf ein THz-Dispersiv-Spektroskop angewandt, welches solch eine Kamera mit dispersiven Optiken kombiniert. Diese Art von Optiken teilt ein breitbandiges THz-Signal räumlich in seine einzelnen Farben auf—ähnlich wie beim Regenbogen—und ordnet jede Frequenz einem bestimmten Kamerapixel zu. Im Bereich von 0.75–0.9 THz konnte somit die durchschnittliche Spektralauflösung von 68.3 GHz auf 34.2 GHz (Faktor 2) verbessert werden, während die Frequenzgenauigkeit sich im Mittel von 30 GHz auf 1.65 GHz (Faktor 18.2) verbesserte. Hierbei werden auch die Leistungsgrenzen des Geräts bzgl. dieser Parameter ermittelt. Zudem wird auf Basis der CMOS-THz-Kamera ein neues Messkonzept zur Bestimmung der Fernfeldcharakteristika von THz-Strahlungsquellen eingeführt. Dieses Messkonzept ermöglicht eine schnelle Erfassung des Fernfeld-Strahlungsmusters von THz-Quellen sowie deren Direktivität, Strahl-Halbwertsbreite und Sendeleistung. Diese Parameter wurden in Anbetracht einer Test-Quelle in einem weiten Frequenzbereich von 0.6–1.1 THz im quadratischen Mittel mit Genauigkeiten von 0.85 dB, 1.1° und 0.7 µW bestimmt. Zudem wurde hinsichtlich des neuen Beleuchtungskonzepts für die THz-Aktiv-Bildgebung erstmals ein diffuser, homogenen-verteilter Strahl aus einem THz-Quell-Array gewonnen, welche eine rekordträchtige Leistung von 10.3 dBm bei 0.42 THz abstrahlt; homogen beleuchtende Quellen sind dringend benötigte, jedoch vor dieser Thesis unerforschte und fehlende Komponenten für die THz-Aktiv-Bildgebung in Echtzeit, um einen gleichmäßigen Dynamikbereich hinweg über die Bildfläche zu gewährleisten. Auf Basis dessen und einer

CMOS-THz-Kamera konnte dann hochperformante Echtzeit-Bildgebung bei THz-Frequenzen vollelektronisch, kompakt und kostengünstig umgesetzt werden.

Diese Thesis legt zudem den Grundstein für die Realisierung einer kostengünstigen und kompakten Alternative für die breitbandige THz-Spektrometrie, welche die Möglichkeit zur Untersuchung von Materialeigenschaften bereits verpackter Güter bietet—für die industrielle Qualitätssicherung. Dazu muss das hier vorgestellte Konzept zur Nutzung inkohärenter THz-Kameras für die Spektroskopie allerdings um eine geeignete THz-Mehrfarben-Quelle erweitert werden. Die Performanz möglicher Quellen ist derzeit mit Hinblick auf deren Sendeleistung allerdings unzureichend. Hier kommt das vorgestellte Beleuchtungskonzept auf Basis von THz-Quell-Arrays ins Spiel, welches eine praktikable Lösung bietet, um die Sendeleistung von THz-Quellen im Allgemeinen zu erhöhen.

Publications

Journal Publications

1. **R. Zatta**, D. Headland, E. Ashna, R. Jain, P. Hillger, J. Grzyb, and U. R. Pfeiffer, "Silicon Lens Optimization to Create Diffuse, Uniform Illumination from Incoherent THz Source Arrays," in *J. Infrared Millim. Terahertz Waves*, pp. 947–959, vol. 42, Oct. 2021. DOI: 10.1007/s10762-021-00828-0.

   RZ conducted all imaging experiments and simulations, performed all analyses, and led the writing of the article.

2. **R. Zatta** and U. R. Pfeiffer, "Performance Limits of THz Dispersive Spectroscopes Employing Super-Resolution Imaging," in *IEEE Trans. Terahertz Sci. Technol.*, pp. 704–711, vol. 11, no. 6, Jun. 2021. DOI: 10.1109/TTHZ.2021.3088278.

   RZ formulated the idea, conducted all experiments and analyses, and led the writing of the article.

3. **R. Zatta**, V. S. Jagtap, J. Grzyb, and U. R. Pfeiffer, "Broadband Lens-Integrated CMOS Camera-Type THz Compact Antenna Test Range," in *IEEE Trans. Terahertz Sci. Technol.*, pp. 527–537, vol. 11, no. 5, Jun. 2021. DOI: 10.1109/TTHZ.2021.3088286.

   RZ formulated the idea, conducted all experiments, simulations, and analyses, and led the writing of the article.

4. **R. Zatta**, R. Jain, J. Grzyb, and U. R. Pfeiffer, "Resolution Limits of Hyper-Hemispherical Silicon Lens-Integrated THz Cameras Employing Geometrical Multi-Frame Super-Resolution Imaging," in *IEEE Trans. Terahertz Sci. Technol.*, pp. 277–286, vol. 11, no. 3, Mar. 2021. DOI: 10.1109/TTHZ.2021.3063839.

   RZ formulated the idea, conducted all experiments and analyses, and led the writing of the article.

5. D. Headland, **R. Zatta**, P. Hillger, and U. R. Pfeiffer, "Terahertz Spectroscope Using CMOS Camera and Dispersive Optics," in *IEEE Trans. Terahertz Sci. Technol.*, pp. 513–523, vol. 10, no. 3, Jun. 2020. DOI: 10.1109/TTHZ.2020.3004516.

   RZ conducted all experiments and full-wave simulations, performed a substantial part of the analyses, and assisted with the writing of the article.

6. **R. Zatta**, R. Jain, and U. R. Pfeiffer, "Characterization of the noise behavior in lens-integrated CMOS terahertz video cameras," in *J. Terahertz Sci. Technol.*, pp. 102–123, vol. 11, no. 4, Dez. 2018. DOI: 10.11906/TST.102-123.2018.12.10.

   RZ conducted all experiments and analyses and led the writing of the article.

Peer-Reviewed Conference Publications

1. **R. Zatta** and U. R. Pfeiffer, "Radial Distortion in Silicon Lens-Integrated THz Cameras," in *Proc. Int. Conf. Infrared Millim. Terahertz Waves*, Chengdu, China, Sep. 2021, pp. 1–2. DOI: 10.1109/IRMMW-THz50926.2021.9567497.

2. R. Jain, P. Hillger, J. Grzyb, E. Ashna, V. Jagtap, **R. Zatta**, and U. R. Pfeiffer, "A 32×32 Pixel 0.46-to-0.75THz Light-Field Camera SoC in 0.13µm CMOS," in *Proc. IEEE Int. Solid-State Circuits Conf.*, San Francisco, CA, USA, Feb. 2021, pp. 484–485. DOI: 10.1109/ISSCC42613.2021.9365832.

3. V. S. Jagtap, **R. Zatta**, S. Nellen, B. Globisch, J. Grzyb, and U. R. Pfeiffer, "Broadband Spectro-Spatial Characterization of CW Terahertz Photoemitter Using CMOS Camera," in *Proc. Int. Conf. Infrared Millim. Terahertz Waves*, Buffalo, NY, USA, Nov. 2020, pp. 1–2. DOI: 10.1109/IRMMW-THz46771.2020.9370841.

4. **R. Zatta**, V. S. Jagtap, J. Grzyb and U. R. Pfeiffer, "CMOS Camera-Type THz Compact Antenna Test Range for Far-Field Radiation Pattern Analysis," in *Proc. Int. Conf. Infrared Millim. Terahertz Waves*, Buffalo, NY, USA, Nov. 2020, pp. 1–2. DOI: 10.1109/IRMMW-THz46771.2020.9370372.

5. **R. Zatta**, V. S. Jagtap, J. Grzyb, and U. R. Pfeiffer, "CMOS THz Camera Used as Compact Antenna Test Range," in *Proc. Int. Worksh. Mob. Terahertz Syst.*, Essen, Germany, Jul. 2019, pp. 1–4. DOI: 10.1109/IWMTS49292.2020.9166379.

6. **R. Zatta**, R. Jain, J. Grzyb, and U. R. Pfeiffer, "Resolution Limits in Lens-Integrated CMOS THz Cameras Employing Super-Resolution Imaging," in *Proc. Int. Conf. Infrared Millim. Terahertz Waves*, Paris, France, Sep. 2019, pp. 1–2. DOI: 10.1109/IRMMW-THz.2019.8874510.

7. **R. Zatta**, R. Jain, D. Headland, and U. R. Pfeiffer, "Incoherent Power Combining of THz Source Arrays," in *Proc. Int. Conf. Infrared Millim. Terahertz Waves*, Paris, France, Sep. 2019, pp. 1–2. DOI: 10.1109/IRMMW-THz.2019.8874075.

8. V. S. Jagtap, **R. Zatta**, J. Grzyb, and U. R. Pfeiffer, "Performance Characterization Method of Broadband Terahertz Video Cameras," in *Proc. Int. Conf. Infrared Millim. Terahertz Waves*, Paris, France, Sep. 2019, pp. 1–2. DOI: 10.1109/IRMMW-THz.2019.8874478.

9. D. Headland, **R. Zatta**, and U. R. Pfeiffer, "Diffuse beam with electronic THz source array," in *Proc. Int. Conf. Infrared Millim. Terahertz Waves*, Nagoya, Japan, Sep. 2018, pp. 1–2. DOI: 10.1109/IRMMW-THz.2018.8509901.

10. D. Headland, P. Hillger, **R. Zatta**, and U. Pfeiffer, "Incoherent, spatially-mapped THz spectral analysis," in *Proc. Int. Conf. Infrared Millim. Terahertz Waves*, Nagoya, Japan, Sep. 2018, pp. 1–2. 10.1109/IRMMW-THz.2018.8510246.

11. R. Jain, **R. Zatta**, J. Grzyb, D. Harame, and U. R. Pfeiffer, "A Terahertz Direct Detector in 22nm FD-SOI CMOS," in *Proc. Eur. Microw. Integr. Circuits Conf.*, Madrid, Spain, Sep. 2018, pp. 25–28. 10.23919/EuMIC.2018.8539908.

Contributions of Others

The contributions of others to this work are listed below. Any research not listed below was conducted by myself.

Chapter 3. THz Dispersive Spectroscopy: Dr. Daniel Headland developed the THz dispersive spectroscope.

Chapter 5. THz Diffuse, Uniform Illumination Source: Dr. Daniel Headland developed the mathematical model to simulate the far-field radiation pattern of a single radiating element coupled to an extended hemispherical dielectric lens. He provided a MATLAB-based tool to perform single-pixel simulations. Eamal Ashna assisted with the far-field radiation pattern measurements.

List of Figures

List of Tables

List of Abbreviations

1-D	one-dimensional
2-D	two-dimensional
3-D	three-dimensional
6G	sixth generation
AUT	antenna under test
CATR	compact antenna test range
CMOS	complementary metal-oxide semiconductor
CMOS-NEMS	CMOS nanoelectromechanical systems
CW	continuous-wave
DC	direct current
DFG	Deutsche Forschungsgemeinschaft
EM	electromagnetic
FFT	fast Fourier transformation
FIR	far-infrared
FoV	field of view
FPA	focal-plane array
GHz	gigahertz
HEMT	high-electron-mobility transistors
HFSS	high-frequency structure simulator
HPBW	half-power beamwidth
IC	integrated circuit
IR	infrared
KID	kinetic inductance detectors
LED	light-emitting diode
MHz	megahertz

MMIC	monolithic microwave IC
mm-wave	millimeter wave
NEP	noise-equivalent power
PSNR	peak signal-to-noise ratio
PTFE	polytetrafluoroethylene
RCS	radar cross section
RF	radio frequency
RMS	root mean square
SiGe	silicon-germanium
SiGe-BiCMOS	SiGe bipolar CMOS
SiGe-HBT	SiGe heterojunction bipolar transistor
SNR	signal-to-noise ratio
SoC	system-on-a-chip
submm-wave	submillimeter wave
TM	transverse magnetic
THz	terahertz
THz-CWS	THz continuous-wave spectroscopy
THz-TDS	THz time-domain spectroscopy
T-MAP	Spatially-Mapped Mobile Terahertz Spectroscopy
UV	ultraviolet

Chapter 1

Introduction

This dissertation contributes to the research of the terahertz (THz) range—a frequency range that occupies a small portion of the electromagnetic (EM) spectrum. Fig. 1.1 serves to illustrate how the THz range is classified in the EM spectrum: it situates between the microwave range and infrared (IR), with frequencies loosely defined from 0.1–10 THz [1]. The millimeter wave (mm-wave) range, extending from 0.03–0.3 THz [2], partially overlaps with the THz range at lower frequencies. The far-infrared (FIR) range, spanning from 3–20 THz [3], does so at higher frequencies. Full overlap is given to the 0.3–3 THz submillimeter wave (submm-wave) band. Occasionally, this band is also referred to as the THz range [4]. All these different EM waves are ubiquitous in our surroundings. Some of them provide a whole range of benefits to our lives, either through active or passive use. For example, radio waves and microwaves allow us to transmit data on a wireless basis [5]. Furthermore, microwaves help us heat our meals quickly [6]. By far, the most obvious benefit comes from the visible light: it enables us to see [7]. In this regard, cameras operating at IR help generate images when our surrounding appears dark to our eyes, which is useful for military observations [8], among other things. X-rays allow us to look into the human body [9], which is of extraordinary benefit to medical diagnostics. In contrast to these more familiar classes of EM waves, the THz range is probably not well known to most people—most likely for a good reason.

The lack of efficient technologies still keeps THz waves from having a noticeable positive effect on our lives. Therefore, the THz range still lags behind neighboring frequency ranges in terms of usage and social impact. Established techniques include

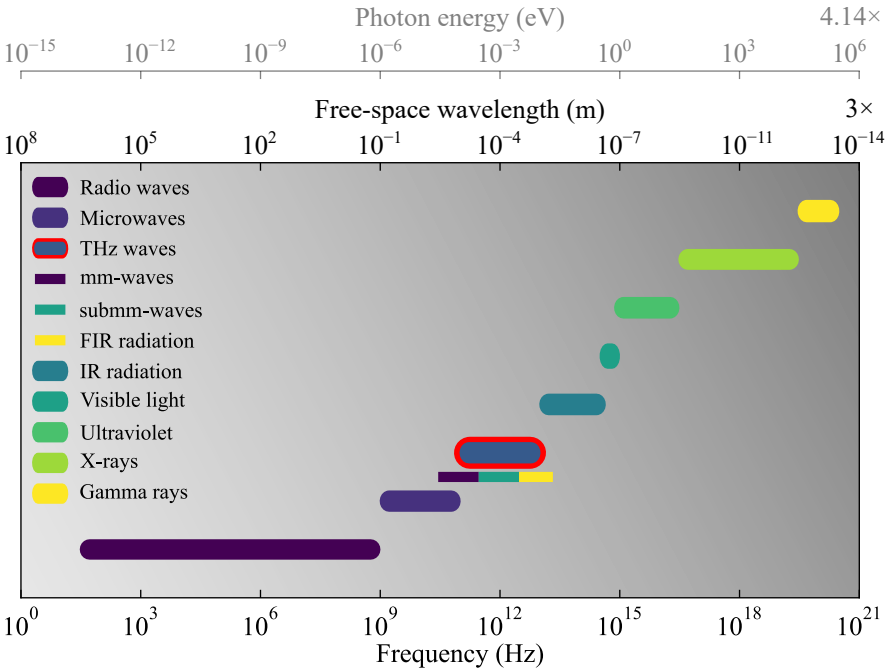

Figure 1.1. EM spectrum. Illustration of the EM spectrum, showing how the THz range is classified in terms of frequency and free-space wavelength. THz waves oscillate at frequencies of 0.1–10 THz, thereby showing relatively small wavelengths of 3–30 µm and low photon energy levels of 0.41–41 meV.

laser-based THz time-domain spectroscopy (THz-TDS) systems [10]–[12] and THz continuous-wave spectroscopy (THz-CWS) systems [13]–[16]. Such systems have been used to characterize the spectral response of many materials in transmission and reflection modes, and the results have been made available online [17], [18]. Thus, they have become an essential part of the THz range for numerous research purposes in active imaging and spectroscopy. However, the drawback of these coherently operated laser-based systems is that they are bulky and expensive and thus can only be used in laboratory environments—most people have never entered a lab. Unlike most socially relevant technologies for imaging and spectroscopy in other frequency bands, they operate coherently. In this regard, incoherent silicon integrated THz systems like large-scale arrays of incoherently operated sources [19], [20] and detectors [own1], [21] incorporated into a single chip can contribute to reducing the size and cost of functional systems significantly to make the THz range accessible to broader society, thereby increasing its usage and social impact. However, the impact of their combined far-field radiation pattern[1] on their performance in terms of spatial resolution in THz active imaging applications must first be fully understood. This understanding is crucial in order to understand how to operate such devices to

[1]This term refers to the beamform with which an antenna transmits or receives EM waves.

produce highly resolved THz images. It is also critical to extending their functionality toward other disciplines, such as THz spectroscopy and THz antenna measurements.

This introductory chapter provides a broader context and shows where this thesis connects to state of the art in research. The outline of this chapter is as follows. The unique properties of THz waves and their potential applications are discussed in Sec. 1.1. Available THz instrumentation and their drawbacks are summarized in Sec. 1.2. The transition to silicon process technologies for THz applications is motivated in Sec. 1.3, with a particular focus on the applicability of silicon integrated THz arrays of incoherently operated sources or detectors. In this context, a literature review of previous works on dielectric lens antennas is also conducted to identify the research gap addressed in this thesis. Section 1.4 introduces the central topic of this dissertation by posing the research questions that this dissertation answers, listing the key achievements of this dissertation, and outlining the subsequent chapters.

1.1 Applications of THz Waves

The unique properties of THz radiation make it suitable for a growing number of potential applications in imaging, sensing and ranging, and wireless communications. The following gives a more specific overview of the diverse fields.

The formation of images using THz radiation has numerous advantages. Most importantly, THz images provide complementary information to images produced with microwaves, IR, visible light, ultraviolet (UV), or X-rays [22]. Compared to lower-frequency waves, THz waves have a shorter wavelength, which translates into better diffraction-limited spatial resolution [23]. At the same time, THz waves are relatively transparent to many common materials, including common packaging materials such as cardboard, plastic, ceramic, paper, and fabric [24]. Therefore, they enable applications in security screening [25], [26] and industrial quality control [27]. In contrast to X-rays, THz waves are non-ionizing and thus biologically safe, which makes them a better, safe alternative for see-through imaging [23], [28]. In addition, THz waves provide better image contrast than X-rays for soft packaging materials [29]. The interested reader is referred to [30] providing the latest roadmap of THz imaging, focusing on the most recent advances in this field.

Since THz radiation is strongly absorbed by water [28], it can be used to determine the water content in biological tissue [31]. However, the spatial resolution achievable through far-field imaging is insufficient to support this aim. In contrast, near-field methods can be leveraged to achieve a subwavelength resolution. The recently developed THz near-field imaging sensor presented in [32] allows producing THz images with a subwavelength resolution of 0.018 λ at a frequency of 0.53 THz. This device has been used to detect breast cancer tissue [33], [34]. The interested reader may refer to [35], [36] for more information about THz near-field methods and associated applications.

The unique interaction between matter and THz waves causes individual spectral fingerprints of materials at their oscillation frequencies. Fundamentally, these THz fingerprints are due to molecular resonances [37]–[39]. Due to the ability of THz radiation to see through many commonly used packaging materials—as discussed above in the context of THz imaging—in combination with these unique fingerprints, THz spectroscopy makes it possible to inspect already packaged goods for material properties [40], [41]. Since water, explosives, amino acids, and drugs also show spectral fingerprints at THz frequencies [42]–[46], THz spectroscopy can also be used for security purposes. In this regard, the pharmaceutical sector can also benefit from THz spectroscopy [47].

In addition to THz imaging and sensing modalities, the large bandwidth available with THz waves can be used to transmit data with ultra high speed, which will be of great benefit to future sixth generation (6G) wireless communications. Initial standardization efforts regarding IEEE 802.15.3d have already been made [48], with the lower-end THz range being addressed. This shows a promising prospect for realizing future 100+-Gb/s data rates [49]–[51]. Future 6G networks operating at these frequencies are anticipated to reach data rates on the order of 1 Tb/s [52]. In this regard, the first wireless communication links with data rates of 100 Gb/s have already been demonstrated [53], [54], with the first cited work implemented in a mass-producible silicon process technology. This demonstration is a crucial step toward supporting the exponentially growing mobile data traffic.

1.2 THz Instrumentation

As alluded to in the preceding discussions, the THz range presents some challenges in realizing practical applications due to the lack of efficient technologies. Ultimately, the realization of practical applications depends upon the availability of low-cost, high-performing sources and detectors of THz radiation. It should be noted that THz passive imaging can use natural ambient (blackbody) radiation [55], [56], eliminating the necessity of an active illumination source. In contrast, THz active imaging relies upon the use of such a source. The problem with passive imaging is that detectors of THz light must show exceptional performance in terms of noise-equivalent power (NEP), as natural ambient THz radiation is extremely weak [4]. The best-performing detectors are cryogenically cooled high-electron-mobility transistors (HEMT), kinetic inductance detectors (KID), superconducting junctions, or microbolometers [57], which allow performing passive imaging at THz [58]. However, these types of detectors are not made for practical use. Despite ongoing advances in THz technology, it is still a challenge to realize practically relevant THz detectors with a high level of sensitivity [59], [60]; the same applies to the realization of THz sources as regards radiation power. Thus, they cannot be transferred to the THz range, and as a result, the THz range manifests as a technological gap referred to as the THz gap [61]. This gap has stemmed from the fact that both electronic and photonic technologies exhaust their performance at THz frequencies; electronic systems are used below THz frequencies and photonic systems above. In this regard, alternative solutions for the realization of THz sources and detectors were investigated using different technologies and different design approaches to bridge this gap. In [62] and [57], in-depth reviews of various THz source and detector technologies can be found, respectively.

Established THz systems—based on lasers, as mentioned upfront, or semiconductor-based monolithic microwave ICs (MMICs) coupled to metallic waveguide blocks [63], [64]—are associated with high bandwidth, high signal-to-noise ratio (SNR), and other well-performing application-specific metrics. Besides cost and size, their complexity limits the scope of practical applications. Admittedly, the complexity of these systems was necessary to realize well-performing systems that allowed access to the THz range in the first place. However, the task now is to reduce the size, cost, and complexity in order to make the THz range accessible to broader society and everyday applications. Silicon integrated integrated circuits (ICs) are extremely useful to support this aim, as they enable miniaturization and mass production.

1.3 Silicon Process Technologies for THz Applications

The transition to silicon process technologies is motivated by the opportunity to reduce the size and cost of functional THz devices. The low-cost production aspect stems from the possibility of mass production due to economies of scale. The aspect of size reduction, on the other hand, relates to the fact that THz waves are small in wavelength—at THz frequencies, the size of these passive structures (e.g., inductors, capacitors, and antennas) becomes small enough to integrate entire systems on a single silicon chip. Silicon process technologies, thereby, offer other advantages, such as low electrical direct current (DC) power consumption, compactness, high integration density, mixed-signal monolithic integration, and reliable operation. Most importantly, they offer a high fabrication yield, which cannot be achieved with better-performing III-V semiconductor technologies. The aspect of high fabrication yield goes hand in hand with scalability, which makes silicon process technologies ideal for implementing monolithic ICs operating at THz frequencies.

The low speed of silicon integrated transistors as compared to their III-V counterparts has caused silicon integrated THz IC design to remain a challenging task. Despite ongoing advances in silicon process technology, it is expected that these will only enable practical THz systems operating up to 1 THz in the not-too-distant future [65]. This is because the fastest SiGe heterojunction bipolar transistors (SiGe-HBTs) available today are still limited to a unity power-gain cutoff frequency, f_{max}, below 1 THz [66]. In this regard, thanks to continuous efforts supported by the EU-funded projects DOTFIVE [67] and DotSeven [68], the complementary metal-oxide semiconductor (CMOS) process compatible SiGe-HBTs have become fast enough for THz circuits operating below 1 THz [65], [69]–[72]. The compability with CMOS devices allows realizing THz systems-on-chips (SoCs) using fast silicon-germanium (SiGe) transistors, which is of great benefit.

In [69], several silicon-based solutions for THz imaging and sensing applications below 1 THz have already been presented, including computed tomography, compressed sensing, spectroscopic imaging, radar imaging, and near-field imaging. The cited work also provides a detailed overview of the performance of THz sources and detectors implemented in different silicon process technologies. In [70], solutions for THz imaging, sensing, and communications applications have been presented, such as high-resolution imaging, high medium/long-term stability timekeeping, high-speed wireline/wireless communications, and miniaturization of radio frequency (RF)

tags, as well as THz packaging technologies. In [71], the benefit of silicon THz ICs has been highlighted, and some of the design challenges for realizing silicon THz ICs are discussed in [72].

Probably the most mature silicon integrated components are the recently released SoCs based on THz arrays of incoherently operated sources [19] and detectors [own1]. These particular SoCs facilitate a range of practical THz applications by taking advantage of the high fabrication yield and mixed-signal integration capabilities provided by silicon process technologies.

1.3.1 THz Applications Using Incoherent Silicon Integrated Arrays of Sources and Detectors

The very first THz image was presented 45 years ago by mechanically scanning a single-pixel detector [73]. Since mechanical scanning is slow, the ultimate aim was to develop THz cameras, which combine a focal-plane array (FPA) and an objective lens. Detectors of THz light that constitute such FPAs can operate on either the heterodyne or the direct detection principle. While heterodyne detectors have orders of magnitude better NEP than their direct detection counterparts [69], they carry a power generation network to provide a local oscillator signal. Therefore, only THz direct detectors underlying an incoherent detection principle have qualified for large-scale FPA integration. In particular, a 32×32-pixel CMOS THz camera has been realized [21]. Many THz applications have been demonstrated with this camera, including active imaging [own2], [own3], [21], [69], [74], light-field imaging [75]–[77], power metering [own4], [own5], spectroscopy [own6]–[own8], compact-range far-field radiation pattern characterization of sources [own9]–[own12], and beam monitoring [78]; some emerged from this work. Other silicon integrated devices with similar pixel counts have also been demonstrated [79], [80], [own1]. THz cameras have also been realized with microbolometer arrays [81]–[89], showing even larger pixel counts. However, while silicon integrated antenna-coupled direct power detectors of THz radiation utilize the electrical nonlinearity of transistors, microbolometer cameras rely on thermal detection. Thermal detection covers not only THz radiation but also IR radiation, and hence external filters are required to remove IR radiation. These filters are costly with regard to the price of such cameras. Given the advantage of their practicability, the objective of this work

is to explore CMOS THz cameras for the disciplines of THz active imaging, THz spectroscopy, and THz antenna measurements.

As for incoherently operated THz detector arrays in silicon, its signal generation counterpart can also benefit from incoherent system approaches. High-power radiation sources, for example, integrated into silicon process technologies, are components that may enable to bridge the THz gap effectively. However, the radiation power of single THz sources decreases dramatically with respect to increasing frequency [69], [90]. In this regard, multiple sources can be operated together to realize THz source arrays of higher total radiation power. Silicon integrated technologies, thereby, are a viable means as they offer the high-yield fabrication needed to realize single-chip solutions. Remarkable efforts have been already dedicated to the realization of both coherent [91]–[98] and incoherent [19], [20], [99]–[101] single-chip THz source arrays. The key difference between these two solutions is that coherent devices need on-chip synchronization to ensure phase-locking among the source elements. Phase-locking may impose performance and array size constraints, although it should be noted that highly scalable devices have been realized [94], [97] due to progress in efficient on-chip synchronization mechanisms. However, incoherent devices continue to scale better and produce higher radiation power [19]. In the cited work, an 8×8-pixel SoC radiating about 10 mW (10 dBm) of power at 0.42 THz has been presented. This amount of radiation power is at least three times higher than the best-reported THz power from any silicon-based source above 0.3 THz [69]. Apart from array size and radiation power, there are other critical differences between the two approaches. Most importantly, coherent radiation can prove detrimental to the image fidelity due to speckles forming because of wave interference, which is detrimental to the overall image quality [102], [103]; for incoherent devices, this is a non-issue. Furthermore, unlike applications in THz wireless communications and THz radar, amplitude-only THz active imaging does not require a coherent signal. For these reasons, this work aims to explore incoherent silicon integrated THz source arrays for THz active imaging applications.

1.3.1.1 Lens-Coupling

Incoherent silicon integrated THz arrays employ an extended hemispherical silicon lens [19], [21], [99], [own1], as illustrated in Fig. 1.2, to suppress undesired substrate modes, extract or receive THz power, provide some directivity to the pixels, and

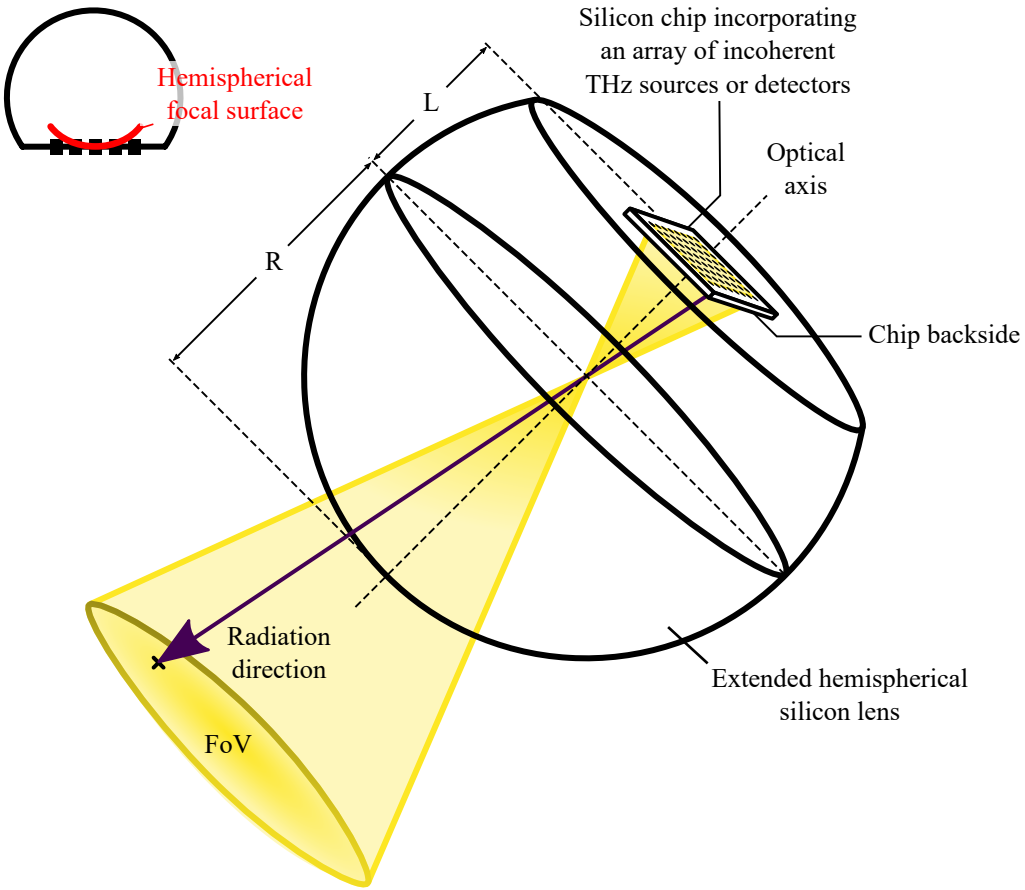

Figure 1.2. Chip-to-lens assembly. Incoherent silicon integrated THz arrays are typically backside-coupled to an extended hemispherical silicon lens. Parameters like directivity of the pixels and FoV of the array are adjustable via the ratio of lens extension length, L, to lens radius, R. As indicated in the upper left, there is a hemispherical focal surface with inverted orientation to the hemispherical portion of the lens surface. The closer a pixel is to this surface, the better it is focused.

project the array aperture onto an angular field of view (FoV). This figure serves to illustrate the chip-to-lens assembly and its effect on far-field characteristics on such devices qualitatively. A more quantitative view on these aspects is provided in the subsequent chapters.

The extended hemispherical silicon lens is a simpler-to-fabricate version of an extended hemielliptical silicon lens by mimicking the elliptical curvature when compensating for the height difference between the hemiellipse and the hemisphere. In the literature, a single lens-coupled antenna is referred to as a "dielectric lens antenna," studied in detail prior to this work. The literature has found the following. The directivity of a dielectric lens antenna depends on the in-silicon position of the feed. Essentially, there exists a hemispherical focal surface within the volume of the

extended hemispherical silicon lens, as indicated in Fig. 1.2. Only if placing a feed along this focal surface, maximum directivity can be achieved. In this regard, the first observations have been reported in [104]. Following this, a more comprehensive study on this aspect has been conducted in [105]. A ratio of lens extension length, L, to lens radius, R, of $L/R = 0.38$–0.39 has been reported to provide the largest directivity for a double-slot antenna placed along the optical axis of the lens. The exact position is frequency-dependent and depends upon the type of antenna used, for which reason only full-wave simulations can identify the exact location that yields maximum directivity. The type of antenna essentially means a different feed directivity. The influence of feed directivity has been studied in [106]. It has been found that increased feed directivity does not necessarily mean reduced directivity of the dielectric lens antenna in the far-field. One step ahead, off-axis properties of the dielectric lens antenna have been studied comprehensively [107]. The observations have shown that off-axis displacements accompany deteriorated directivity, but an adjustment in lens extension length can compensate for this, at least up to some extent. This makes perfect sense, as an adjustment in lens extension length causes to bring the feed into the elliptical focus along the hemispherical focal surface mentioned above. Complex reflections inside the dielectric occur if extended hemielliptical or hemispherical dielectric lenses do not have an antireflection coating [108]. Antireflection coatings may be employed to reduce the effect of internal reflections in order to optimize directivity. However, these coatings are narrowband and therefore cannot be used in the context of broadband radiating ICs like incoherent silicon integrated THz FPAs. It has also been found that edge illumination affects the directivity achievable with dielectric lens antennas due to internal reflections occurring [109]; edge illumination means the ratio of power directed toward lens edges to that in the broadside. In addition to improving directivity, coupling silicon chips to extended hemispherical silicon lenses eliminates substrate modes [110], improves the front-to-back radiation ratio [111], and adds mechanical rigidity and thermal stability to chips [105]. For these reasons, the most integrated THz sources [16], [112], [113] and detectors [114]–[117], [own13] are backside-coupled to a silicon lens.

Despite the many studies on dielectric lens antennas, open questions remain regarding far-field radiation characteristics of incoherent silicon integrated THz arrays backside-coupled to an extended hemispherical silicon lens. The first aspect is that there has been no comprehensive study to understand the image formation and associated resolution limitations of silicon integrated THz cameras using an

extended hemispherical silicon lens. This understanding is critical to operating such cameras to achieve the best possible image quality. The first works that have approached this aspect are [75] and [118] providing an ideal camera image formation model and a closed-form relation between scan angle and feed position, respectively. In this context, the second cited work derived design considerations to achieve optimal FoV sampling. Such optimal sampling, however, can only be realized for a single radiation frequency, and hence the question arises of how this affects the performance of a broadband camera in actual THz active imaging applications. The second aspect is that understanding the shape of the composite far-field beam generated for various lens dimensions was limited, as previous studies were restricted to single radiating elements. While the first aspect relates more to arrays of incoherent detectors, the second aspect points to arrays of incoherent sources. These two aspects are contributed by this thesis, which helped develop novel application and illumination concepts using such devices.

1.4 This Dissertation

The preceding discussions aimed to equip the reader with the necessary preliminary knowledge about applications of THz waves and the available instrumentation associated with them. These discussions have highlighted that the traditionally used photonic and electronic platforms suffer from severe drawbacks for practical use, including high cost, low level of integration, and low reliability. With this in mind, the case for incoherent silicon integrated THz arrays of sources and detectors backside-coupled to an extended hemispherical silicon lens was made because of their practicability due to low cost, small size, high integration levels, and high scalability. While the former are vital pieces to overcome radiation power limitations at THz frequencies, their signal reception counterparts allow producing a THz image without the necessity for mechanical scanning. Increasing the element count and improving performance on parameters that ultimately determine the SNR achievable in THz active imaging applications have been the primary research focus regarding these components in recent years. Although single radiating elements equipped with an extended hemispherical silicon lens are well understood, the fundamental understanding of how the combined far-field radiation pattern of such devices affects their performance in THz active imaging applications was limited prior to this thesis. Therefore, the overarching aim of this thesis is, on the one hand, to understand this aspect in full detail. This understanding is critical to know how to operate these

devices together to achieve optimal performance in terms of spatial resolution. On the other hand, this is crucial to provide a cost-effective, compact alternative for THz active imaging with real-time capabilities. Furthermore, this thesis aims to extend the functionality of such devices toward THz spectroscopy and THz antenna measurements to provide cost-effective and compact alternatives for these disciplines as well. In this context, this section formally introduces the subject matter of this dissertation in terms of research questions, key achievements, and thesis outline.

1.4.1 Research Questions

This dissertation is aimed at answering the following research questions:

Research Questions

1. How to operate an incoherent silicon integrated THz camera to achieve the best possible image quality in terms of spatial resolution?
2. What are the fundamental performance limits of a silicon-based THz dispersive spectroscope in terms of spectral resolution and frequency accuracy?
3. Can an incoherent silicon integrated THz camera be employed to determine far-field characteristics of an AUT at a compact range?
4. How to create diffuse, uniform illumination from incoherent silicon integrated THz source arrays?

1.4.2 Key Achievements

The following key achievements were obtained from the research reported in this dissertation:

1. The individual research grant proposal “Spatially-Mapped Mobile Terahertz Spectroscopy (T-MAP)” was funded by DFG. The design of dispersive optics was envisaged to convert a frequency-unselective, incoherent silicon integrated THz camera from an imaging device into a spectroscope, and super-resolution imaging was to improve its performance in terms of spectral resolution and frequency accuracy.

2. A study on the image formation and associated resolution limitations of silicon integrated THz cameras was communicated in a peer-reviewed scientific journal [own2]. This study serves to guide how to operate such cameras to produce highly resolved images in THz active imaging applications.

3. A THz dispersive spectroscope using a CMOS camera and dispersive optics has been presented in a peer-reviewed scientific journal [own6]. In a follow-up article in the same journal, its performance limits in spectral resolution and frequency resolution using low- and super-resolution imaging were discussed in detail [own7].

4. A novel THz antenna measurement concept was developed with which far-field characteristics of an antenna under test (AUT) can be conveniently determined over a broad frequency range by using an incoherent silicon integrated THz camera. This novel measurement concept and its experimental validation were communicated in a peer-reviewed scientific journal [own9].

5. A previously developed incoherent THz source array was converted into a THz diffuse, incoherently-combined, uniform-intensity illumination source by tailoring the geometry of the backside-coupled lens—without the need for any modification to the IC itself. This will be communicated in a scientific journal; submission of the manuscript is completed, and it is currently under review.

1.4.3 Thesis Structure

This thesis is divided into a total of six chapters. They are organized as follows:

Chapter 1. Introduction draws out the research motivation, embeds this dissertation scientifically, poses the research questions, and lists key achievements as well as thesis outline.

Chapter 2. Resolution Limits of Silicon Integrated THz Cameras discusses the fundamental frequency-dependent angular and spatial resolution limits achievable using incoherent silicon integrated THz cameras for low- and super-resolution imaging. In this context, we discuss how such cameras must be operated to produce highly resolved THz images.

Chapter 3. THz Dispersive Spectroscopy briefly presents the THz dispersive spectroscope. Experimental characterization and verification of this device are

provided. Furthermore, a study to understand the performance limits of such devices in terms of spectral resolution and frequency accuracy is conducted.

Chapter 4. THz Compact Antenna Test Range presents the application concept of the THz compact antenna test range (CATR) based on an incoherent silicon integrated camera facilitating a convenient means to perform far-field characteristics determination of radiation sources. The capabilities of this instrument regarding far-field characteristics determination are evaluated, and design considerations for new devices are derived.

Chapter 5. THz Diffuse, Uniform Illumination Source presents the method to convert an array of incoherently operated THz sources into a diffuse, uniform illumination source, thereby realizing a functional device.

Chapter 6. Conclusion and outlook presents the end conclusions and future outlook for incoherent silicon integrated THz arrays of sources and detectors backside-coupled to an extended hemispherical silicon lens.

Chapter 2

Resolution Limits of Silicon Integrated THz Cameras

2.1 Chapter Introduction

As with any other camera, the two key parameters that determine the image quality when using incoherent silicon integrated THz cameras are SNR and spatial resolution [119]. While SNR is more a technological matter related to the NEP of the THz detectors [69], the spatial resolution achievable in an image refers to the diffraction-limited angular resolution of the camera lens [120]. A high angular resolution implies that the camera can resolve finer details of an object. The ultimate aim is to produce images with diffraction-limited spatial resolution. To this end, a camera must oversample its FoV, as illustrated in Fig. 2.1(a). On the other hand, if a camera undersamples its FoV [Fig. 2.1(b)], the spatial resolution achievable in an image will be geometrically limited to the beam separation angle between two adjacent camera pixels and the distance to the object. In this case, only super-resolution[1] imaging can help produce images of diffraction-limited resolution.

This chapter equips the reader with a general understanding of the fundamental frequency-dependent angular resolution limits of incoherently operated THz cameras integrated into silicon process technologies. A theoretical framework is provided in this regard, which is supported by experimental investigations. Specifically, two

[1] This imaging method relies upon acquiring multiple images under different exposures and overlapping them accordingly, which facilitates oversampling. More under Sec. 2.3.

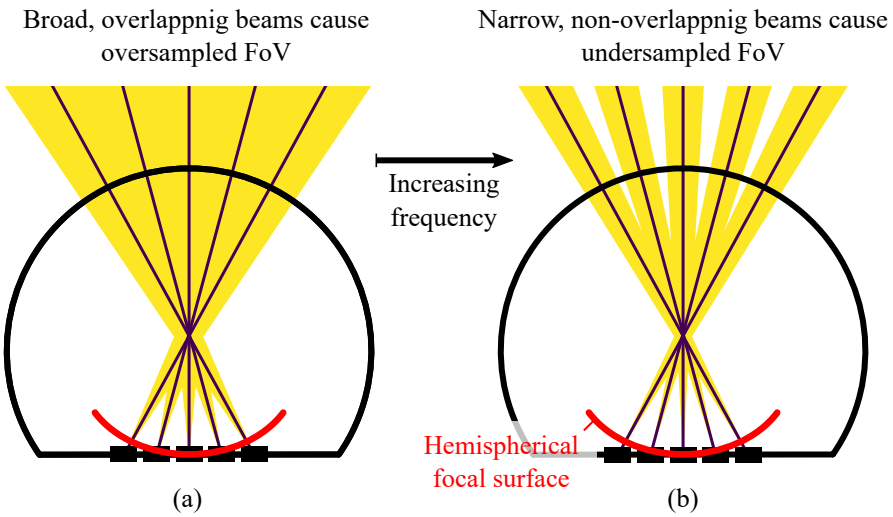

Figure 2.1. FoV over- and undersampling. Illustrations of FoV over- (a) and undersampling (b). In constrast to an oversampled FoV, an undersampled one may benefit from super-resolution imaging to reach the diffraction-limited angular resolution provided by the camera lens. This is because, in case of an undersampled FoV, beam divergence is smaller than beam separation.

experimental studies were performed at 0.652 THz. These are about super-resolution imaging and the determination of the complete far-field characteristics of the camera. While the former demonstrates how to operate such devices to effect a diffraction-limited spatial resolution in imaging, the other provides a quantitative picture of the resolution achievable over the imaging plane with respect to off-axis aberrations and radial distortion. The experimental studies presented are chiefly concerned with a commercially available 32 × 32-pixel CMOS THz camera from Ticwave GmbH, Wuppertal, Germany, which employs the FPA from [21]. Nevertheless, the investigations and discussions are general in nature and thus apply to any incoherent silicon integrated THz camera. With respect to the discussions in Sec. 1.3.1.1, the contribution of this chapter to knowledge is to understand how to operate such devices to produce highly resolved THz images. Also, the content of this chapter forms the foundation for the other three main chapters.

This chapter is a modified, expanded version of [own2], and it is outlined as follows; another related work is [own3]. In Sec. 2.2, details of the CMOS THz camera relevant to the present study are given. In this context, the theoretical framework is discussed. Section 2.3 explains the THz super-resolution imaging method used. Section 2.4 is about the performed THz super-resolution imaging experiment. In Sec. 2.5, experimental results obtained from the full far-field radiation pattern analysis are provided. Finally, a conclusion is drawn in Sec. 2.6.

2.2 CMOS THz Camera

The $5 \times 5 \times 5$-cm^3 large CMOS THz camera consists of the FPA from [21] backside-coupled to an extended hemispherical silicon lens. The FPA bears 32×32 pixels of incoherently operated THz direct power detectors incorporated into a single silicon chip of 3×3.2 mm^2. The FPA is implemented in 65-nm CMOS process technology, thereby rendering it amenable to mass production, engendering a significant reduction in per-unit cost under high-volume manufacturing. Each camera pixel consists of a resistive self-mixing circuit coupled to a broadband ring antenna. This circuit converts incident THz power into DC voltage, which is subsequently converted into a digital signal. This signal is processed with a desktop computer via a USB interface. Peak detector integrated video-rate NEP of 17 nW occurs at 0.822 THz [own4], and the camera spans a 0.265-THz 6-dB operating bandwidth from 0.725–0.990 THz [own14]. The silicon lens has a diameter of 15 mm and an extension length of 2.75 mm. The lens dimensions are optimized toward realizing maximum directivity, according to [107]. Specifically, the ratio of lens extension length to lens radius of 0.367 yields an experimentally-tested maximum directivity ranging between 39.5 dBi and 43.5 dBi from 0.64–1.028 THz, while projecting the FPA imaging aperture to an experimentally-tested FoV of 46° [21].

2.2.1 Angular Resolution Limits

The angular resolution limits of the CMOS THz camera employing super-resolution imaging are associated with the diffraction-limited angular resolution provided by its extended hemispherical silicon lens. Several criteria approximating the angular resolution limit of a lens are known from the literature [121], [122]. The three most commonly applied criteria are the Rayleigh criterion, Sparrow criterion, and half-power beamwidth (HPBW) criterion. In the following, they are compared in terms of applicability with regard to the camera.

Understanding the angular resolution limits comes along when looking at the Airy disks of two individual point sources of equal intensity placed side by side. Figures 2.2(a), (b), and (c) illustrate the summation of two individual point source diffraction patterns using the Rayleigh criterion, Sparrow criterion, and HPBW criterion, respectively. The Rayleigh criterion describes the threshold where the maximum intensity position of one Airy disk coincides with the first minima of the

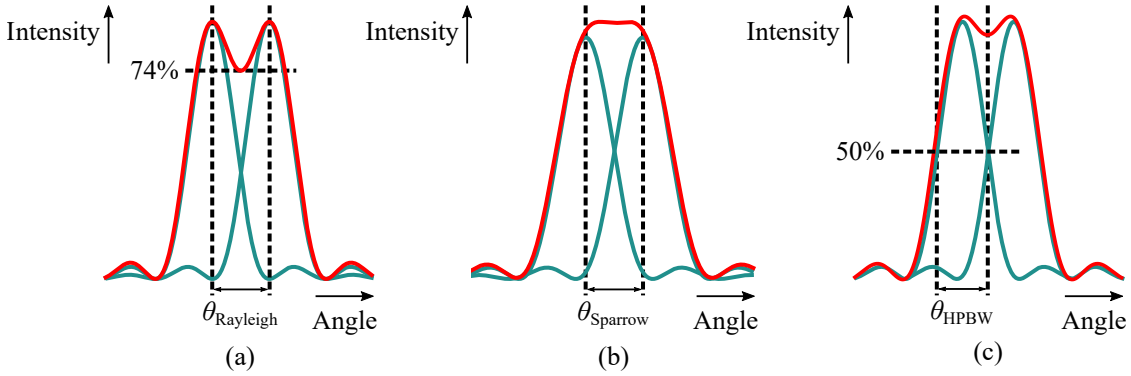

Figure 2.2. Angular resolution criteria. Illustration of three commonly applied resolution criteria, such as (a) Rayleigh criterion, (b) Sparrow criterion, and (c) HPBW criterion with angular resolutions θ_{Rayleigh}, θ_{Sparrow}, and θ_{HPBW}, respectively, with respect to diffraction patterns of two point images at various separations. The Rayleigh resolution limit is reached if the dip between the two maxima is 26%. The Sparrow limit, however, says that the limit is reached if the first and second derivates of the combined intensity pattern vanish. The HPBW criterion is a close measure to the Rayleigh criterion. Here, two Airy disks are said to be resolved, when they entirely overlap below their 50% intensity level.

other Airy disk. For circular apertures, the intensity dip in between the two image points in the combined diffraction pattern is 26%. In contrast, the Sparrow criterion is a stricter criterion. It allows detection of the image duplicity, although there is no minimum between the maxima from the two point source diffraction patterns. The Sparrow criterion represents a measure to the physical limit of diffraction, whereas the Rayleigh criterion is way more conservative. The third criterion, the HPBW criterion, is close to the Rayleigh criterion, and it describes the point where the intensity levels of two Airy disks fully overlap below their 50% intensity level. The angular resolution limit of optical systems, such as lenses or mirrors, associated with the Rayleigh criterion, θ_{Rayleigh}, Sparrow criterion, θ_{Sparrow}, and HPBW criterion, θ_{HPBW}, is expressed by the following equations:

$$\theta_{\text{Rayleigh}} = \frac{1.22 \cdot \lambda_0}{D_{\text{Lens}}}, \tag{2.1}$$

$$\theta_{\text{Sparrow}} = \frac{0.94 \cdot \lambda_0}{D_{\text{Lens}}}, \tag{2.2}$$

$$\theta_{\text{HPBW}} = \frac{\lambda_0}{D_{\text{Lens}}}, \tag{2.3}$$

where λ_0 and D_{Lens} denote the free-space radiation wavelength and the lens diameter, respectively.

As stated earlier, the HPBW criterion only differs slightly from the Rayleigh criterion, still representing a quite conservative measure to the angular resolution, unlike the Sparrow criterion. For camera pixels, the HPBW, which relates to the directivity, is readily measurable through a far-field radiation pattern scan, thus facilitating a convenient means to estimate the angular resolution. Furthermore, the HPBW directly relates to the 10–90% rising edge criterion commonly used to determine the spatial resolution achieved in an image [123], [124]. For these reasons, the HPBW is employed throughout this thesis as a measure for angular resolution.

Having discussed the angular resolution limits of optical systems in general, we now introduce the theoretical framework concerning the angular resolution limits of CMOS THz cameras. To this end, we must understand how fixed design parameters (beam incidence angle, beam separation angle, and FoV) are fundamentally related to frequency-dependent parameters (directivity and HPBW). The following calculations refer to the two-dimensional (2-D) dielectric lens antenna model from [75], [118] that is illustrated in Fig. 2.3; further insight regarding this model is provided by Fig. 2.4.

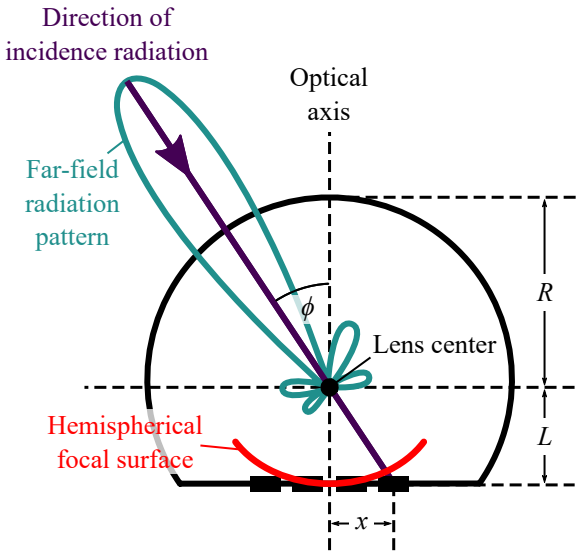

Figure 2.3. The 2-D dielectric lens antenna model. Illustration of the 2-D model of a dielectric lens antenna. Feeds are placed at the in-silicon focal plane of the dielectric lens, at a position x. This particular position is associated with a beam incidence angle, ϕ, with respect to the optical axis of the lens. This angle is defined by the lens extension length, L. As can be seen, the lens radius, R, does not influence the beam incidence angle. According to [75] and [118].

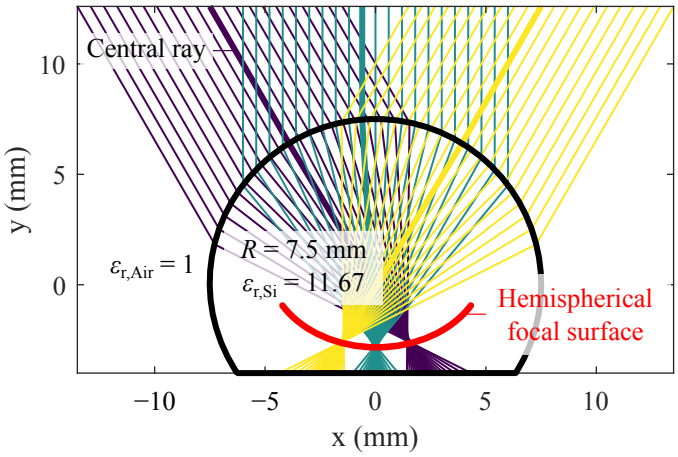

Figure 2.4. Ray-tracing calculations for CMOS THz camera. Ray-tracing calculations for the CMOS THz camera under investigation here using actual lens parameters and Snell's law of refraction. Here, ray-tracing is shown for three different angles of incidence. Bundles of parallel rays striking the camera lens under a particular angle focus on a certain predictable point on a hemispherical focal surface within the dielectric. Consequently, maximum directivity can be achieved with a pixel placed along this focal surface, as we discussed in the context of Sec. 1.3.1.1. The common choice is to place central camera pixels in focus, which lies in this specific case beyond the lens center. It is noted that the hemispherical focal surface may change in radius and position with respect to the lens dimensions and lens dielectric.

The beam separation angle between two adjacent camera pixels is associated with the difference in their beam incidence angles. According to [75], [118], the beam incidence angle of a pixel, ϕ, can be calculated as

$$\phi = \tan^{-1}\left(\frac{x}{L}\right), \tag{2.4}$$

where x stands for the pixel position with respect to the optical axis of the lens, and L is the lens extension length. It is interesting to note that the beam incidence angle does not depend on the lens radius, R, but only on the lens extension length. From Eqn. (2.4), it follows that the beam separation angle between two adjacent central camera pixels, $\delta\phi$, can be calculated as

$$\delta\phi \approx 2 \cdot \tan^{-1}\left(\frac{\frac{p}{2}}{L}\right), \tag{2.5}$$

where p is the pixel pitch. This equation, however, only holds for central pixels fulfilling conditions for small-angle approximation. The definition that is valid

for any two adjacent camera pixels is

$$\delta\phi = \tan^{-1}\left(\frac{x_{\mathrm{i}} - x_{\mathrm{i+1}}}{L + \frac{x_{\mathrm{i}} \cdot x_{\mathrm{i+1}}}{L}}\right), \tag{2.6}$$

where x_{i} and $x_{\mathrm{i+1}}$ denote the position of one pixel and another subsequent one, both with respect to the optical axis of the lens. The constant radius camera FoV, Φ, being the beam separation angle between the two outermost pixels along the horizontal or vertical of the FPA, can therefore be calculated as

$$\Phi = 2 \cdot \tan^{-1}\left(\frac{\frac{N-1}{2} \cdot p}{L}\right), \tag{2.7}$$

where N stands for the camera pixel count of either of the laterals. The frequency-dependent directivity, D, can be estimated from the effective antenna aperture of the camera lens [125] as

$$D = \frac{4\pi A_{\mathrm{eff}}}{\lambda_0^2}, \tag{2.8}$$

where λ_0 denotes the free-space radiation wavelength, and A_{eff} represents the cross-section area of the camera lens, with $A_{\mathrm{eff}} = \pi R^2$, where R is the lens radius. This directivity estimation only applies to camera pixels placed along the hemispherical focal surface inside the silicon lens. According to [125], the relation between HPBW, θ_{HPBW}, which describes the HPBW criterion, and directivity can be approximated with

$$D = \frac{32400}{\theta_{\mathrm{HPBW}}^2}. \tag{2.9}$$

From Eqns. (2.8) and (2.9), the HPBW, θ_{HPBW}, can be calculated as

$$\theta_{\mathrm{HPBW}} = \frac{\lambda_0}{2 \cdot R}, \tag{2.10}$$

which is in perfect alignment with Eqn. (2.3), the HPBW criterion.

Beam separation angle [Eqn. (2.6)] and HPBW [Eqn. (2.10)] are independent. The beam separation angle depends on the pixel pitch and the lens extension length, which are fixed design parameters. In contrast, the HPBW depends on the lens radius, which is a fixed parameter, and the incident radiation frequency, which is variable. This causes frequency regions where the camera over- and undersamples

its FoV. Oversampling refers to broad, overlapping pixel beams [Fig. 2.1(a)]. On the other hand, if beams are narrow and do not overlap, the camera undersamples its FoV [Fig. 2.1(b)]. Since this depends on the radiation frequency, there exists a crossover frequency, f_o, below and above which over- and undersampling frequency regions exist. Below this crossover frequency, the HPBW is larger than the beam separation angle. Thus, the camera performs oversampling as indicated in Fig. 2.5(a). At the crossover frequency, the beam divergence angle crosses below the beam separation angle. This means that from now on a camera will undersample its FoV, as shown in Fig. 2.5(b). As the frequency increases, camera pixel beams become narrower and narrower [Fig. 2.5(c)], and consequently, the undersampling becomes more pronounced.

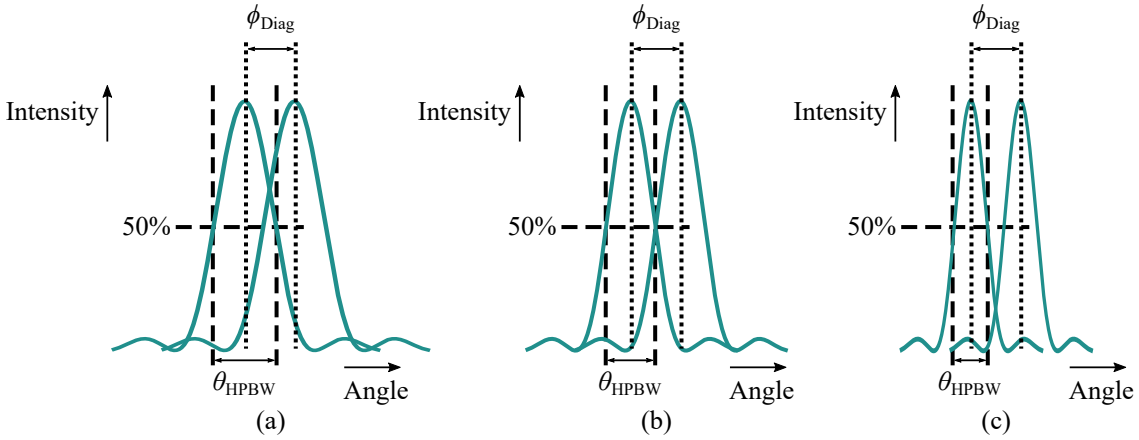

Figure 2.5. Adjacent pixel far-field radiation patterns. Illustration of the overlap between two adjacent camera pixels situated in an FPA diagonal for different scenarios. In all of them, the diagonal beam separation angle, ϕ_{Diag}, is fixed. In contrast, the HPBW, θ_{HPBW}, is frequency-dependent. More specifically, it decreases with respect to increasing frequency. There are cases where beam divergence is under beam separation (a), matches beam separation (b), and is above beam separation (c). The first two are associated with oversampling and the last one with undersampling. The "middle" case is associated with the crossover frequency f_0. After [own2] © 2021 IEEE.

Multi-frame super-resolution imaging can improve the angular resolution at frequencies where the HPBW is under the beam separation angle. Briefly, several images are acquired at angular offsets and superimposed to produce an oversampled image. The overarching aim of using super-resolution imaging is to realize maximum resolution across the full radiation pattern, FPA, or an image acquired with the camera. In order to achieve a diffraction-limited spatial resolution over the entire imaging plane, the diagonals of the radiation pattern must be oversampled. Related to the on-chip spacing between camera pixels situated in the FPA diagonal and the

HPBW criterion, the crossover frequency is located at 0.486 THz, as indicated in Fig. 2.6, showing the derived model capable of predicting the angular resolution limits of the camera with respect to frequency for low- and super-resolution imaging. It is noted that a different criterion, such as the Rayleigh criterion or Sparrow criterion, would yield a slightly offset crossover frequency, and hence the given crossover frequency should be treated as approximate. Furthermore, what this figure shows is, of course, tied to the camera concerned here. Nevertheless, the prediction model of the angular resolution can easily be adapted to any other camera, regardless of the FPA constitution or design of the extended hemispherical silicon lens. Therefore, this model is a meaningful tool to predict the maximum achievable, diffraction-limited resolution with a camera of this sort and to identify over- and undersampling regions. The identification of these regions is essential to anticipate whether or not super-resolution imaging will yield an enhancement in angular resolution, translating into a spatial resolution in an actual THz image.

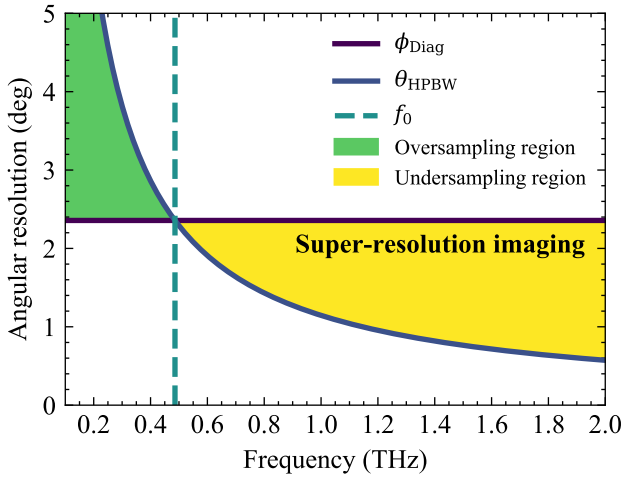

Figure 2.6. Prediction of angular resolution. The maximum angular resolution, θ_{HPBW}, achievable with the 15-mm diameter camera lens, is plotted along with the beam separation angle between camera pixels situated in the chip diagonal, ϕ_{Diag}. The angular resolution follows the maximum achievable angular resolution (i.e., HPBW) when using low-resolution imaging until reaching the crossover frequency. After that, for higher frequencies, the angular resolution is limited to the beam separation angle. Super-resolution imaging can be employed to reach back the maximum achievable angular resolution in undersampling cases. Therefore, the crossover frequency separates an over- from an undersampling frequency region. After [own2] © 2021 IEEE.

When it comes to THz active imaging, the angular FoV of the camera must be transformed into a spatial illumination aperture. To this end, the camera can be extended by a collimating lens, as illustrated in Fig. 2.7. Here, the camera lens

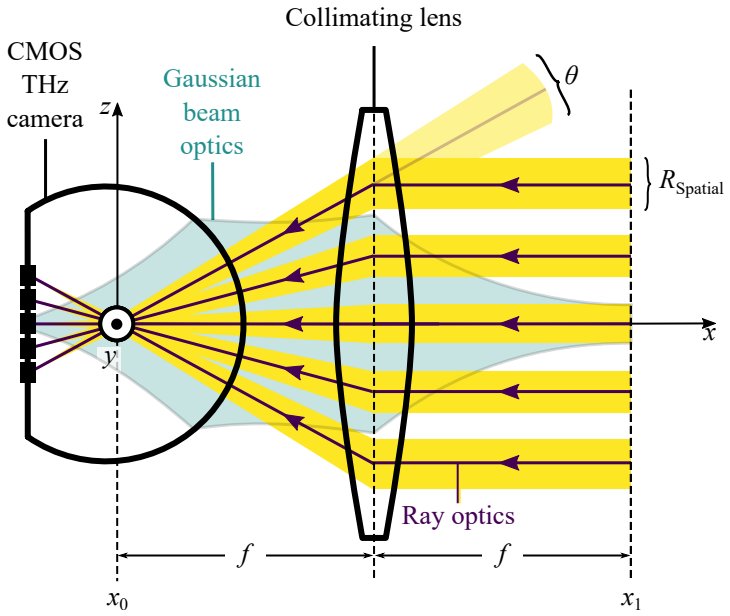

Figure 2.7. Transformation from angular FoV to spatial illumination aperture. Illustration of how the angular FoV of the camera is projected onto a spatial illumination aperture by a collimating lens. The transformation from angular FoV to spatial illumination aperture causes the angular resolution, θ, to translate into a spatial resolution, R_{Spatial}, to be observable in the imaging plane, x_1. This figure makes use of a ray-optics representation, which aligns at x_1 with its Gaussian-beam-optics counterpart—if the pixels were transmitting—as indicated for the center pixel.

must be placed so that the camera lens center coincides with the focal point of the collimating lens. In this figure, this point is marked as x_0. As a consequence of transforming the angular FoV into a finite illumination aperture through a collimating lens, the angular resolution of the camera is translated into a spatial resolution, to be observable in the object plane, x_1. It should be noted that the ray-optics representation that this figure makes use of is a simplification and that this representation applies only to placing an imaging target in the object plane. To clarify, ray optics only applies when far-field conditions prevail, which is only the case in the imaging plane. The object must therefore be placed precisely at this position. It should be clear that the camera can only produce an image with maximum, diffraction-limited spatial resolution when the object is in its focus. If placing an object far away from this position, blurred images will be produced. Furthermore, here the case is made for an undersampled object plane, where super-resolution imaging will be required to achieve the diffraction-limited spatial resolution. On the other hand, of course, there is an oversampled object plane when the camera oversamples its FoV. The spatial resolution realized in the object plane, R_{Spatial}, can be calculated as the product of the angular resolution in radians, θ_{HPBW}, and the distance between

the camera lens and the collimating lens, which is to say, the focal distance, f:

$$R_{\text{Spatial}} = f \cdot \theta_{\text{HPBW}}. \tag{2.11}$$

Accordingly, the spatial resolution is a function of the object magnification, which is intuitive: the larger the distance from an object, the fewer details one can identify.

2.2.2 Design Considerations

The preceding discussions aimed to equip the readers with necessary preliminary knowledge about parameters influencing the angular resolution achievable with an incoherent silicon integrated THz camera. In this regard, the following design considerations concerning the pixel pitch required for optimal sampling can be derived from the previous discussions by substituting Eqn. (2.5) into Eqn. (2.10). By substitution, it follows that the pixel pitch, p, required to yield camera pixel beams overlapping at their HPBW is

$$p = \frac{\lambda_0}{2} \cdot \frac{L}{R}, \tag{2.12}$$

where λ_0 is the free-space radiation wavelength, L is the lens extension length, and R denotes the lens radius, in agreement with [118]; the feed-dependent coefficient used in the cited work is neglected here for simplicity. This derived equation adds some physical insights into the design process of incoherent silicon integrated THz arrays backside-coupled to extended hemispherical silicon lenses, regardless of whether that array constitutes a number of sources or detectors. The L/R-ratio must, for a silicon lens, be about 0.367 to realize maximum achievable directivity, according to [107]. In the design of a broadband THz camera, the pixel pitch optimization becomes particularly challenging since Eqn. (2.12) is wavelength- or frequency-dependent. Here, the optimal pixel pitch can only be realized for one particular frequency. Therefore, the pixel pitch must be selected so that the far-field beams of adjacent camera pixels show the required overlap at their highest radiation frequency. This causes that a small pixel pitch is required in a broadband THz camera, which is practically impossible to realize. One major concern, thereby, represents the mutual pixel coupling. This form of coupling can arise from the parasitic EM fields between two nearby antennas or substrate modes occurring from reflections within the substrate of the FPA. Grounding shields should be placed around the camera pixels

to prevent the EM field leakage [19], [21] in order to minimize pixel pitch. The other issue is lessened by backside-coupling the FPA to an extended hemispherical silicon lens [105]. In [126], the mutual coupling—when using such a lens—was found to be on the order of –25 dB to –30 dB. However, the footprint of a camera pixel is also affected by the DC biasing network required. Ultimately, the minimum pixel pitch is limited by these factors. Thus, a broadband THz camera employing an extended hemispherical silicon lens as its objective can never oversample its FoV for all frequencies; this also applies to cameras of other sorts. That is to say, for high radiation frequencies, super-resolution imaging will be required to mitigate any FoV undersampling.

2.3 Method of THz Super-Resolution Imaging

Super-resolution imaging, in general, is an imaging method primarily targeted toward accomplishing better spatial resolution observable in an actual image. This method can further be divided into optical super-resolution imaging and geometrical super-resolution imaging. The former is used to break the physical diffraction barrier [127], whereas the latter is intended to approach the diffraction-limited resolution of a camera or any other optical system [128]. Geometrical super-resolution imaging can be further divided into single-frame geometrical super-resolution imaging and multi-frame geometrical super-resolution imaging. Both of these imaging methods work on the principle of subpixel shifting. As the terminologies imply, geometrical single-frame super-resolution imaging performs subpixel shifting based on a single frame, whereas its multi-frame counterpart performs subpixel shifting based on multiple frames. The latest research on single-frame methods deals with neural networks [129]–[131]. The media has been abuzz about Google's just-released single-frame super-resolution neural network-based imaging tool for upscaling low-resolution photos. Unlike neural network-based geometrical single-frame super-resolution imaging, multi-frame methods do not require any data post-processing. Also, as opposed to neural network-based single-frame super-resolution imaging, multi-frame methods reflect the actual scene. To clarify, neural networks are used in the context of single-frame super-resolution imaging to render images of enhanced spatial resolution from low-resolution images, however, by incorporating details that are not there in reality. These modifications to the original image data are so minor that the observer cannot determine whether an image is of originality or not. Instead, with geometrical multi-frame super-resolution imaging, multiple images of the same scene are acquired at angular offsets, as

illustrated in Fig. 2.8. Through the superimposition of these angularly offset images, a super-resolution image can be produced. This way, gaps in the FoV of an imaging system can be filled accordingly. The typical wording used for the process of acquiring several angularly offset images is *dithering*. Many astronomical cameras, for instance, are operated in the so-called dithered mode, with slight shifts between different exposures [132], [133]. The process of superimposition in this context is termed *drizzling*. In other words, geometrical multi-frame super-resolution imaging combines dithering and drizzling. In particular, dithering together with drizzling, as performed with geometrical multi-frame super-resolution imaging, can reconstruct the information lost because of spatial undersampling. Recently, a black hole was imaged for the first time based on this [134].

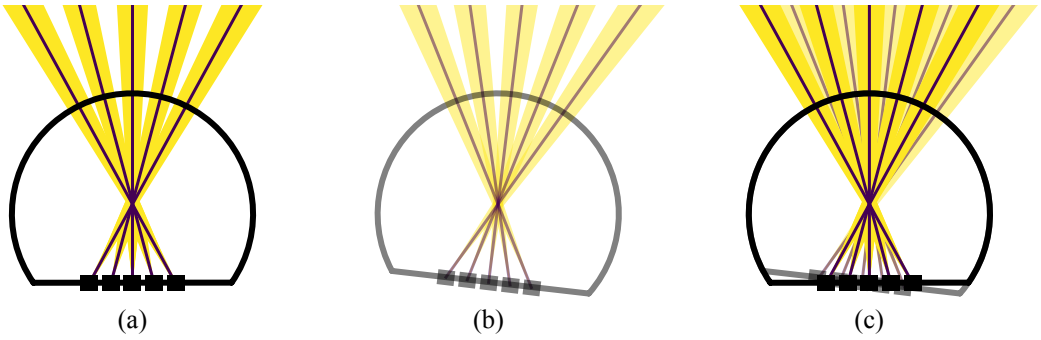

Figure 2.8. Concept of multi-frame super-resolution imaging. In this example, the camera exposes the scene under view from two different angles: under a normal angle to the optical axis of the lens (a) and an angular offset (b). The two exposures themselves would yield producing undersampled (or low-resolution) images because the camera undersamples its FoV. Nevertheless, an oversampled image can be created by combining these low-resolution images, as shown in (c), since the scene under view is essentially oversampled when combining those angularly offset exposures.

In the case of the CMOS THz camera, dithering can be performed with raster-scanning. Remember that this camera must be coupled to a collimating optic to project its angular FoV to a spatial illumination aperture, rendering an object plane. By reciprocity, if the imaging target is raster-scanned in this object plane, the imaging target is projected onto the camera lens under different beam incidence angles. In other words, when raster-scanning an object in a collimated beam, the object is viewed under different exposures. This way, a set of images with small angular shifts between different exposures is acquired, representing the process of dithering. The beauty of this is that each raster scan position is known, which makes drizzling convenient. In this case, drizzling for the creation of a super-resolution image based on $I \times J$ low-resolution images can be performed utilizing the algorithm

from [135]. This algorithm is illustrated in Fig. 2.9, based on 2×2 low-resolution images with 3×3 pixels each. This figure just serves as an example to illustrate the process of drizzling, and it should be clear that the whole process is scalable.

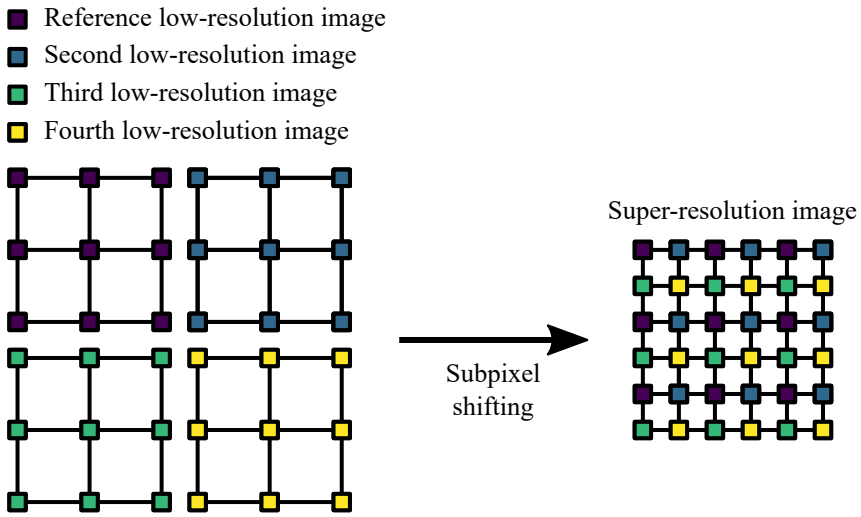

Figure 2.9. Super-resolution imaging method. Illustration how 2×2 low-resolution images with 3×3 pixels acquired at angular offsets by dithering are drizzled into a 36-pixel super-resolution image. This process is scalable. From [own2] © 2021 IEEE.

The following is a more general description of the super-resolution algorithm implemented in this work:

$$SR = \begin{pmatrix} LR_{0,0,0,0} & \dots & LR_{0,\mathrm{J},0,\mathrm{L}} \\ \vdots & \ddots & \vdots \\ LR_{\mathrm{I},0,\mathrm{K},0} & \dots & LR_{\mathrm{I},\mathrm{J},\mathrm{K},\mathrm{L}} \end{pmatrix}, \tag{2.13}$$

where $LR_{\mathrm{i,j,k,l}}$ represents the measurement performed by a camera pixel with pixel coordinates (i, j) at the position (k, l) of the raster scan. The digital resolution, R_{Digital}, is calculated as

$$R_{\mathrm{Digital}} = I \cdot J \cdot K \cdot L, \tag{2.14}$$

where I and J stand for the pixel count in the respective dimension of the FPA, and K and J are the number of low-resolution images in the respective dimension of the raster scan. Thus, the digital resolution is improved by the number of low-resolution images $(K \cdot L)$. However, an increased number of low-resolution images does not necessarily mean better spatial resolution achieved in a drizzled image. This does depend upon the fact of the severity of undersampling for a low-resolution image. To clarify,

a small set of low-resolution images will be sufficient to produce a super-resolution image of diffraction-limited spatial resolution just above the crossover frequency of a camera for optimal FoV sampling. With increasing deviation from this frequency, however, an increased number of low-resolution images will be required.

On one hand, super-resolution imaging helps break the geometrical angular resolution limit of a broadband THz camera. On the other hand, it is also clear that improved angular resolution is generated at the cost of increased image acquisition time, which is at least somewhat compensated by a higher SNR. To clarify, in imaging, SNR is described as the ratio of signal power to root mean square (RMS) image noise. The signal power increases by acquiring multiple images, while the RMS image noise remains constant. Consequently, the SNR increases. The improvement in SNR is even more pronounced at frequencies where the camera undersamples its FoV. When undersampling occurs, there are gaps in the camera FoV that are not sampled because there are radiation-insensitive regions between the camera pixels. Super-resolution imaging for oversampling can fill these gaps in the FoV, as different exposures upon the camera cause previously unseen portions of an incident radiation wavefront to migrate into radiation-sensitive regions of the FPA.

2.4 THz Super-Resolution Imaging Experiment

In this section, the theoretical framework [Sec. 2.2.1] is experimentally verified with a THz super-resolution imaging experiment. In the following, the experimental setup and the experimental results are presented one after another.

2.4.1 Experiment

For THz super-resolution imaging, the experimental setup that is illustrated in Fig. 2.10 was employed; it is reminded of the fact of simplification of ray-optics representation. This setup represents a collimated beam setup, and it works as follows. The radiation source on the right provides diverging wavefronts that are collected by a polytetrafluoroethylene (PTFE) lens. This source radiates 2 mW at 0.652 THz and is equipped with a 25-dBi standard gain horn antenna, while the camera pixels exhibit a video-rate NEP of around 28 nW at this frequency [own4]. The focal length of 100 mm defines the distance between the radiation source and this lens. According to the Fraunhofer distance, this distance is larger than the far-field

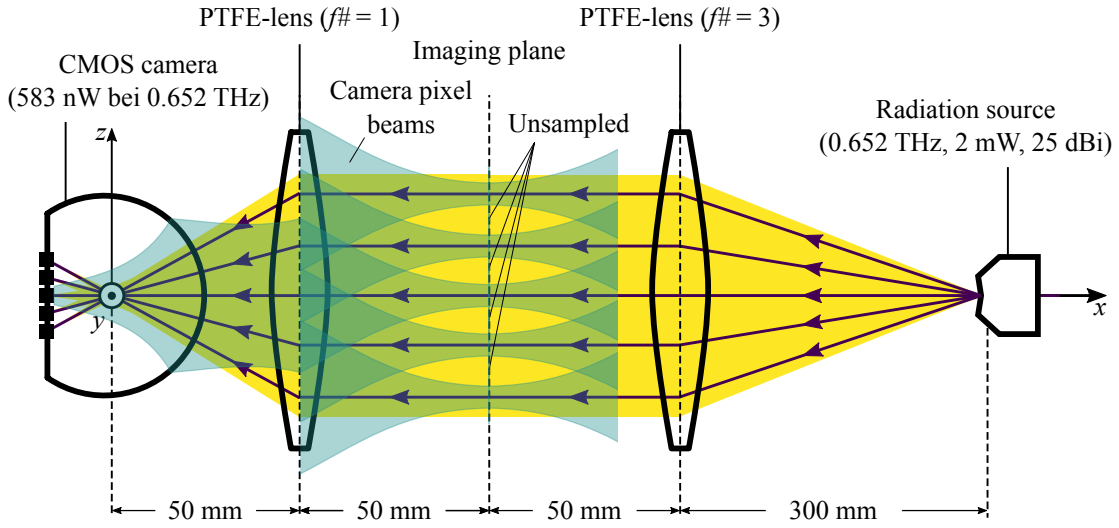

Figure 2.10. THz super-resolution imaging setup. Illustration of the experimental setup employed for THz super-resolution imaging. The setup comprises a THz radiation source, the investigated camera, and an optical train consisting of two PTFE lenses. This optical system provides a collimated beam in the object plane. In this collimated beam, a metallic annular disc was raster-scanned, and at each location of the raster scan, a low-resolution image was acquired with the camera, which may be drizzled to produce a super-resolution image.

distance of the radiation source of ∼25 mm at 0.652 THz related to its aperture diameter of 2.4 mm. The phase center of the radiation source coincides with the focal point of the lens. Thus, collimated radiation wavefronts create an object plane to the left of the collimating PTFE lens. The illumination aperture is determined by the 50-mm diameter of the PTFE lens since its f-number closely corresponds to the HPBW of the radiation source of 10°. The collimating wavefronts are collected by another 50-mm diameter PTFE lens. Compared to the right-handed PTFE lens, this one has a smaller f-number of 1 that closely corresponds to the camera FoV of 46°, and it projects the object plane onto the hemispherical portion of the camera lens, with the camera undersampling its FoV causing not to cover the entire object place, as indicated with the blank spaces. Finally, the camera lens causes the object plane to appear as an inverted image on the FPA. Since the camera lens center coincides with the focal point of the right-handed collimating lens, all converging wavefronts cross at this exact point, according to [75]. All components except the radiation source were mounted in a cage system to provide mechanical stability to the optical system.

In the object plane, an imaging target was raster-scanned. The imaging target was a 1-mm thin metallic annular disc, with an outer diameter of 50 mm and a cutout diameter of 15 mm. At each position of the raster scan, an image was acquired with

the camera. Thereby, the camera readout was averaged over a total of 1024 frames to ensure high imaging of 53 dB, according to SNR [own4], at a relatively moderate overall measurement time of 16 minutes. The total distance of this raster scan in each dimension was 1.45 mm. The lateral step size, thereby, was 181.25 µm. Thus, a total of 8×8 low-resolution images was acquired. The corresponding angular step size concerning the beam incidence angle of the camera is $\sim 0.2°$. Superimposing a subset of low-resolution images yielded creating super-resolution images of different matrix sizes, characterized by different spatial resolutions as well as different digital resolutions.

2.4.2 Measured Results

Figure 2.11 shows a low-resolution image and several super-resolution images drizzled from different numbers of low-resolution images. More specifically, the low-resolution image is shown in Fig. 2.11(a), whereas the subfigures (b), (c), and (d) show super-resolution images created from 2×2, 3×3, and 4×4 low-resolution images. All these images are normalized to their maximum intensity pixel, with the colorbars giving image intensity as normalized power. As can be observed qualitatively, the spatial resolution in actual images improves with respect to an increasing number of low-resolution images used to produce a super-resolution image.

One of the primary goals of performing this experiment was to verify the fundamental frequency-dependent angular resolution limits of the camera. To support this aim, the edges along the image diagonals were inspected for their edge response to identify the enhancement in spatial resolution by drizzling with respect to an increasing number of low-resolution images. The spatial resolution enhancement can then be translated into an angular resolution enhancement, according to Eqn. (2.11).

To provide a qualitative picture of that, Fig. 2.12 shows the edge response in the upper left image diagonal, plotted as normalized power as a function of the distance (primary x-axis) and the beam incidence angle (secondary x-axis). More specifically, a small portion of the upper left image diagonal is plotted, as indicated by the solid lines in Fig. 2.11. To clarify, edges along the diagonals were selected because the undersampling is most pronounced in the FoV diagonal of the camera due to a $\sqrt{2}$ larger beam separation angle than in their lateral counterparts.

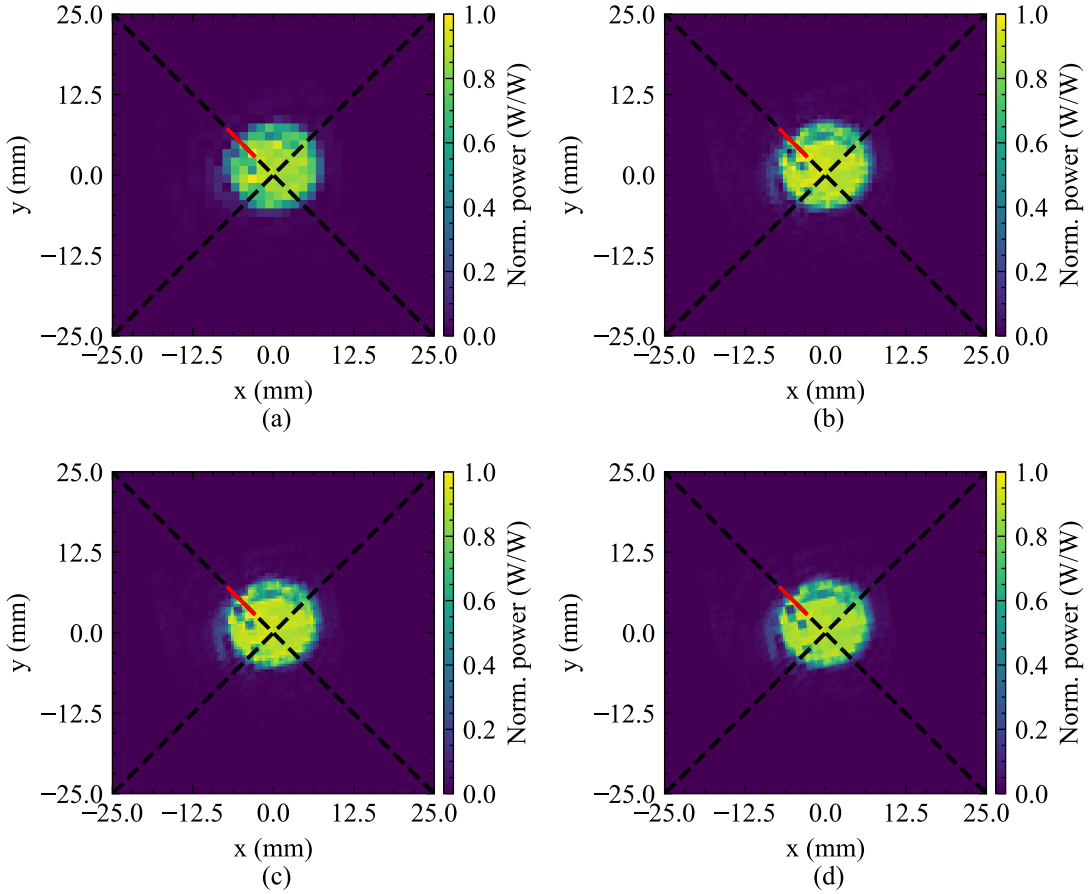

Figure 2.11. THz super-resolution imaging results. Measured low-resolution image (a) and different super-resolution images (b), (c), and (d) superimposed from 2×2, 3×3 , and 4×4 low-resolution images. The edges along the image diagonals were inspected for their edge response functions, as indicated by the dashed lines. The solid lines indicate the portions for which cross-section cuts are provided in the following.

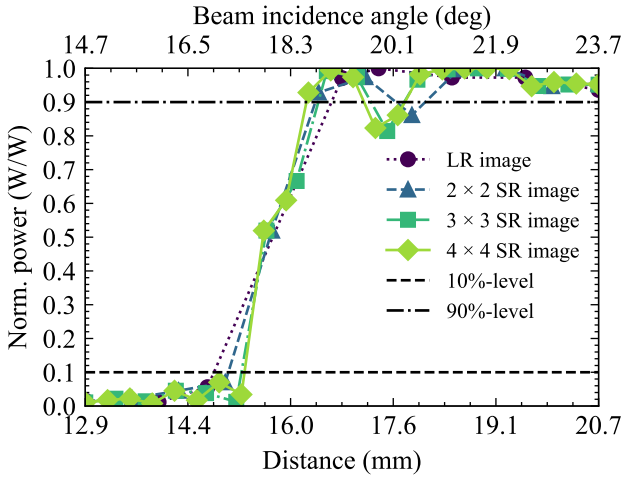

Figure 2.12. Results of edge response. Results of edge responses for a low-resolution image and super-resolution images drizzled from different numbers of low-resolution images. After [own2] © 2021 IEEE.

The quantitative picture of the spatial and angular resolution enhancement is provided with another investigation. To this end, the spatial resolution was determined for all edges along all four diagonals from the 10–90% rising edge criterion, as motivated earlier [Sec. 2.2.1], and translated into an angular resolution using Eqn. (2.11). The enhancement in angular resolution is shown in Fig. 2.13. In this figure, both spatial resolution and angular resolution obtained from the measured low-resolution and super-resolution images are compared to the theoretical limitations given by the Sparrow criterion [Eqn. (2.2)] and HPBW [Eqn. (2.3)]. From inspection of this figure, it is evident that low-resolution imaging entails an angular resolution limited to the beam separation angle between two adjacent pixels if FoV undersampling is concerned, while super-resolution yields achieving the diffraction-limited resolution given by the lens. Diffraction-limited performance was achieved for 4×4 low-resolution images used to produce a super-resolution image. As such, the multi-frame super-resolution image that leads to oversampling at 0.652 THz has about 16k pixels. The estimated measurement time is 4 minutes related to the 1024 frames used for averaging.

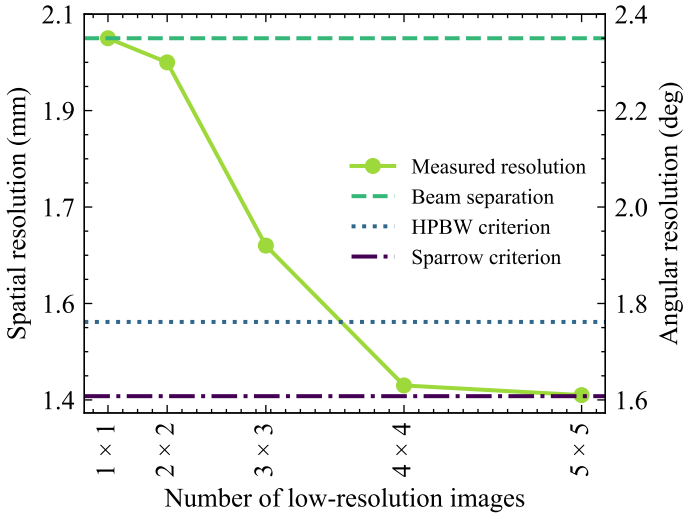

Figure 2.13. Measured angular and spatial resolution. Angular and spatial resolution obtained from edge responses for a low-resolution image and super-resolution images with respect to increasing matrix size. After [own2] © 2021 IEEE.

2.4.3 Discussions

The quantitative analysis on the spatial and angular resolution achievable through low- and super-resolution imaging proves that the theoretically calculated resolution limits are valid for the camera. Hence, the frequency-dependent angular resolution

of an incoherent silicon integrated THz camera that comes along with an extended hemispherical silicon lens can be estimated with commonly used resolution criteria. According to the more conservative criterion, the HPBW criterion [Eqn. (2.3)], the experimentally tested camera module can reach an expected angular resolution of 1.39° at 0.822 THz, where it exhibits optimum NEP. According to the Sparrow criterion [Eqn. (2.2)], the camera can reach an angular resolution of 1.3° at this frequency. It is noted that the angular resolution naturally improves with respect to increasing frequency, according to the principle of physical diffraction. HPBW criterion and Sparrow criterion predict an angular resolution of 1.15° and 1.06° at 1 THz. Employing a larger lens would enhance these numbers even further. However, then, the angular FoV would be compromised.

As elaborated earlier, the camera needs to be coupled to a collimating lens to translate its angular FoV into a spatial illumination aperture to create an object plane. Therefore, this additional lens also translates the angular resolution of the camera into a spatial resolution. In that case, the spatial resolution, observable in the object plane, is determined by the focal length of the additional lens and the angular resolution of the camera [Eqn. (2.11)]. Here, the camera was combined with an external lens that helped create an imaging plane of 50 mm in diameter. Therefore, it reached a measured spatial resolution of 1.43 mm at 0.652 THz. The estimated spatial resolution at 0.822 THz is 1.14 mm. The spatial resolution would improve for smaller imaging apertures. For example, if the camera FoV was translated to a 30-mm diameter spatial illumination aperture through a collimating lens with an f-number of one, the achievable spatial resolution would be 1 mm at 1 THz.

2.5 Far-Field Radiation Pattern Characterization

This section presents the complete far-field characterization of the camera, which aims to quantify the resolution variation across the full camera frame with respect to off-axis aberrations and radial distortion. Understanding and quantifying these aberrations is crucial because they directly affect the beam divergence of the camera pixels and the beam separation between two of them, which we know determine the overlap of the associated far-field beams and thus affect the spatial resolution observable in an actual image. In the following, the experimental setup is shown before providing insights into the measured results; here, off-axis aberrations are treated before radial distortion.

2.5.1 Experiment

The experimental setup that is illustrated in Fig. 2.14 was employed to perform the far-field characterization. The setup consists of a radiation source and the camera under investigation. The radiation source is the same as in the imaging experiments discussed in this chapter, namely a ×48 multiplier chain-based 0.652-THz 2-mW radiation source equipped with a standard gain horn antenna that adds a directivity of 25 dBi. This source and the camera were placed at a far-field distance of 1 m. The camera was mounted onto a six-axis table-top UR5 robot arm to facilitate a rotational raster scan. In this regard, a polar raster scanning was performed. Specifically, the camera was scanned over a $\pm 25° \times \pm 25°$-sector of the hemisphere. With this, all camera pixels were covered since the camera bears an FoV of 46°. The step size was 0.5°. At each angular position, a 32×32-pixel camera frame was acquired. The camera was operated at 30 fps, and the camera readout was averaged over 1024 frames to ensure a sufficiently high SNR, according to [own4].

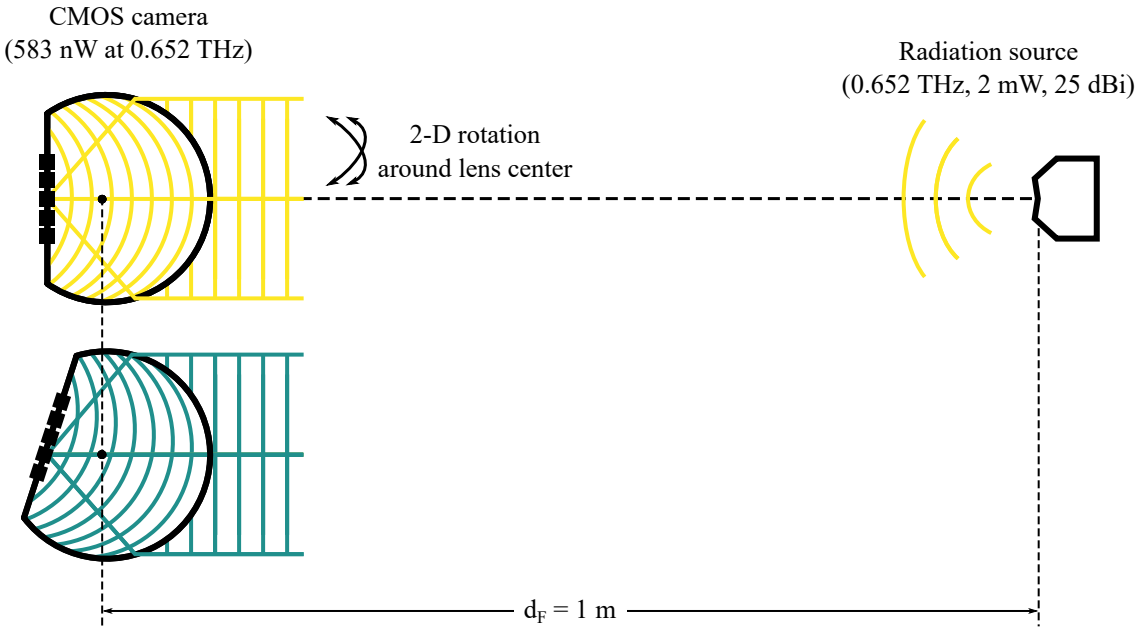

Figure 2.14. Far-field radiation pattern setup. Illustration of the experimental setup that was employed for the full far-field radiation pattern characterization of the camera. The setup comprises a 25-dBi 2-mW 0.652-THz source and the investigated camera module, which are separated by a 1-m far-field distance. The camera was mounted onto a six-axis table-top UR5 robot arm for rotational scanning.

2.5.2 Measured Results and Discussions

Figure 2.15 shows 2-D single-pixel radiation patterns for four pixels situated in an FPA diagonal with normalized off-axis displacements of $x/R = -0.005$ (a), $x/R = 0.048$ (b), $x/R = 0.101$ (c), and $x/R = 0.155$ (d). Figure 2.16 shows one-dimensional (1-D) cross-section cuts along the E-plane (a) and H-plane (b) for the entire FPA diagonal. Here, E-plane and H-plane refer to the horizontal and vertical cross-section cuts through the point of maximum intensity of the far-field radiation patterns as indicated by the dashed lines in the 2-D plots. In figures of 1-D representations, single-pixel far-field radiation patterns are related to the normalized off-axis displacement of the corresponding camera pixel, with normalized off-axis displacements being calculated as the ratio of off-axis displacement to lens radius. From inspection of these figures, it is clear that pixel beams broaden with respect to increasing normalized off-axis displacement, indicating deteriorated directivity, resulting in higher noise. In addition to that, it can be obtained from the 1-D cross-section cuts that the centers of gravity of the pixel beams curve somewhat inward with respect to increasing normalized off-axis displacement. These observations already provide a qualitative picture of off-axis aberrations and radial distortion. The following sections go one step beyond that by providing quantitative analyses on these aspects.

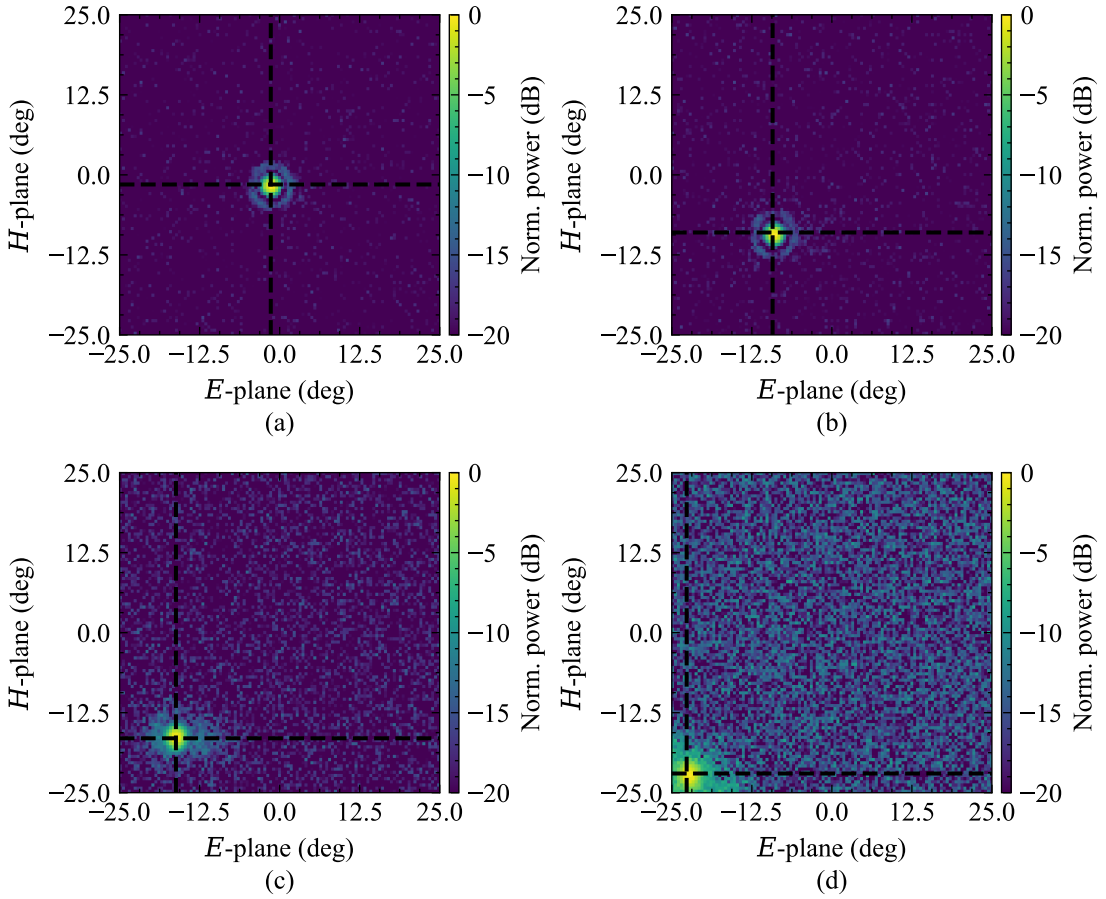

Figure 2.15. 2-D single-pixel far-field radiation patterns. Normalized single-pixel radiation pattern for four pixels in a chip diagonal underlying normalized off-axis displacements of $x/R = -0.005$ (a), $x/R = -0.048$ (b), $x/R = 0.101$ (c), and $x/R = 0.155$ (d).

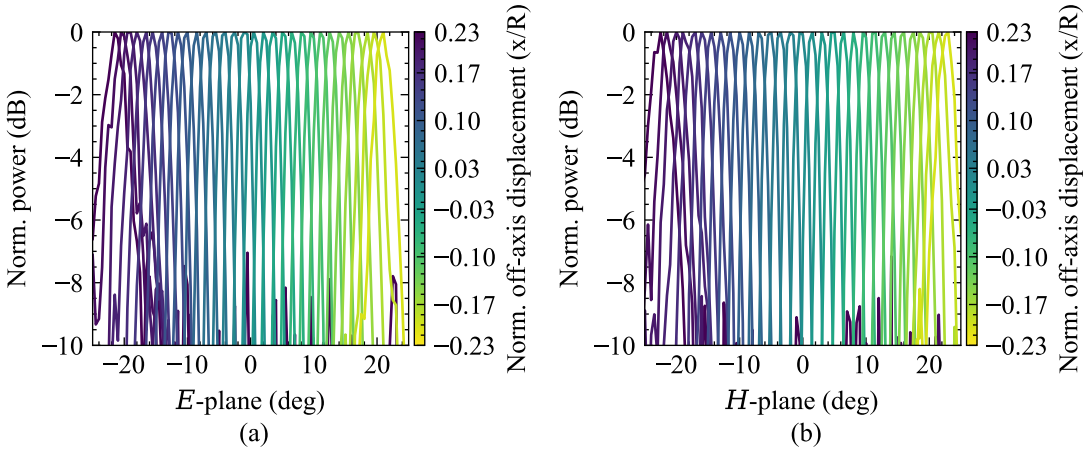

Figure 2.16. 1-D single-pixel far-field radiation patterns. Normalized single-pixel radiation pattern cross-section cuts for pixels situated in a chip diagonal along the E- (a) and H-plane (b). Colorbars indicate the normalized off-axis displacement with respect to the plotted curves.

2.5.2.1 Off-axis aberrations

Off-axis aberrations, such as coma and astigmatism, cause blurring toward image edges [121]. The simple cause for this is that source pixel beams become broader and broader with respect to increasing off-axis displacement, and this can be described quantitatively through either the HPBW or the directivity variation across the full camera frame. HPBW and directivity were determined from measured single-pixel far-field radiation patterns for each pixel to provide a quantitative picture of the angular resolution behavior across a full camera frame, as shown in Fig. 2.17(a) and (b), respectively. The former shows the HPBW represented as a 2-D function of normalized off-axis displacement in both lateral dimensions, whereas the latter does accordingly for the directivity. HPBW values were extracted directly from single-pixel radiation patterns. In contrast, directivity values were calculated as the ratio of maximum power to total power on a linear scale for each camera pixel, whereafter this linearly-scaled value was converted to dBi-scale. This figure provides a quantitative picture of the achievable angular resolution across the full camera frame at the frequency of investigation (0.652 THz) by giving the real HPBW or directivity variation. Although this quantitative picture cannot hold for other frequencies, it does hold qualitatively.

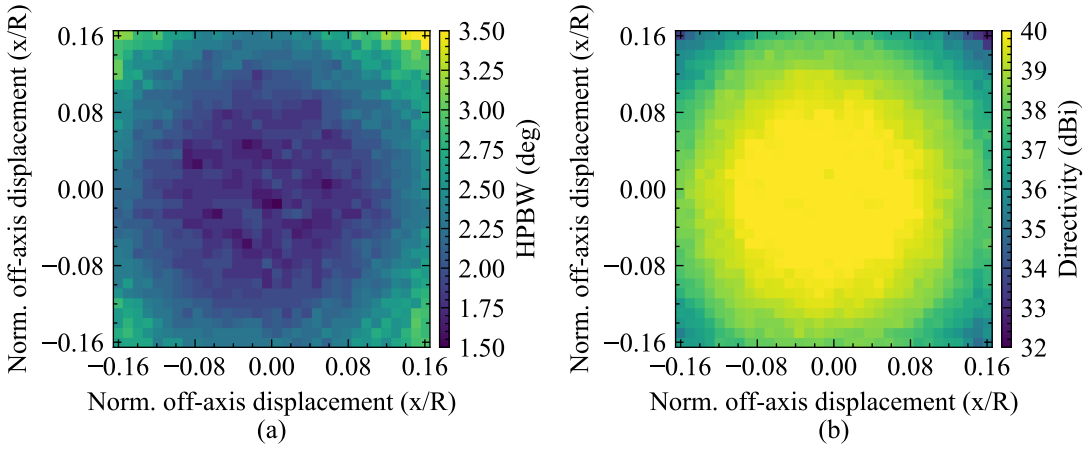

Figure 2.17. Measured HPBW and directivity of values. HPBW (a) and directivity (b) as a 2-D function of the normalized off-axis displacement in both dimensions of the FPA obtained from single-pixel far-field radiation pattern measurements performed at 0.652 THz for the 32.6-λ diameter silicon camera lens. Subfigure (b) is after [own2] © 2021 IEEE.

The analysis of the HPBW variation across the FPA further verifies the validity of the measured results obtained from super-resolution imaging. It is remembered

that the maximum angular resolution achieved was 1.6°. The average HPBW for the 10 × 10 camera pixels located in the center is 1.8°. Scaling with the conversion factor between the HPBW criterion and the Sparrow criterion yields an angular resolution of 1.68° by the Sparrow criterion, which is in excellent agreement with the diffraction-limited angular resolution of 1.6° achieved in the super-resolution imaging experiment.

2.5.2.2 Radial distortion[2]

Because of the physics of light, every lens produces imperfect, distorted images [121]. This distortion is not to be confused with off-axis aberrations, which causes blurring toward the edges of the image. In contrast, lens distortion describes the deviation from a straight-line projection of a scene under view. Radial distortion is usually divided into three main types: *radial distortion*, *decentering distortion*, and *thin prism distortion*. Radial distortion is the predominant component in most cases. The two main types in this regard are *barrel distortion* and *pincushion distortion*. As the terminologies imply, barrel distortion means that straight lines are curved inward in the shape of a barrel, while pincushion distortion means that straight lines are curved outward in pincushion shape. Most of the time, both types of radial distortion are highly undesirable in imaging, but they can be corrected in data post-processing [136], [137]. Although this type of distortion is not to be confused with off-axis aberrations, it does affect the achievable resolution when using super-resolution imaging. For instance, Barrel distortion causes a decreasing beam separation angle as the distance from the optical axis of the lens increases, which increases the beam overlap between two adjacent pixels. Therefore, it is crucial to know the type of radial distortion in the camera to solidify further the qualitative picture of the image formation and associated resolution limitations. Prior to this thesis, radial distortion in extended hemispherical silicon lenses has not been researched, although remarkable efforts have been dedicated to studying the scan angle [75], [107], [118]. While the simulation results in [107] have indicated that, for small angles, the scan angle depends linearly on the feed position, [75], [118] have pointed out that lenses of this sort are essentially thick lenses and hence defined a better, closed-form relation that refers to the central ray. However, the question arises as to how accurate such an approximation can be since a far-field radiation pattern is generally a much more complex phenomenon than a single ray. This is where radial distortion comes into play.

[2]This section is a modified version of [own15].

In order to identify the type of radial distortion, a beam incidence angle grid was generated. To this end, the 2-D beam incidence angle coordinate was determined for each camera pixel. Here, the 2-D moment of associated single-pixel far-field radiation patterns was calculated, considering only the main lobe, i.e., values equal to or greater than –3 dB were set to zero. This is reasonable since the main lobe determines the angular resolution. Figure 2.18 shows the beam incidence angle grid generated, indicating Barrel distortion. In Fig. 2.19, the diagonal values along the E- and H-plane, as marked in Fig. 2.19(a), are compared with the values calculated using the equation provided in [75], [118] [see Eqn. (2.4)]. From this figure, it is clear that this equation is a good approximation for pixels that are located close to the optical axis of the lens since the RMS error (right axis) is close to zero. With increasing distance from the optical axis, the RMS error increases quadratically. The main problem regarding this equation is that it only considers the central beam—far-field radiation patterns of off-axis displaced pixels may not be symmetrical. Figure 2.19(b) shows the beam separation angle determined obtained from deriving the beam incidence angle curves. The beam separation angle is largest for pixels situated toward the lens center and decreases with respect to increasing normalized off-axis displacement. Accordingly, beam overlap in super-resolution imaging increases with respect to increasing distance from the optical axis.

Besides further solidifying the qualitative picture of image formation and associated resolution limitations in the camera, the beam incidence angle grid will allow for better geometric camera calibration. This will be particularly valuable for light-field imaging [75], [own1] and applications based on it, such as spectral analysis [own6] and far-field radiation pattern analysis [own9] of radiation sources. In addition, the findings will be important for beam switching applications other than THz active imaging, such as THz communications or THz radar, as radial distortion traces back to the intensively studied scan angle, as mentioned earlier.

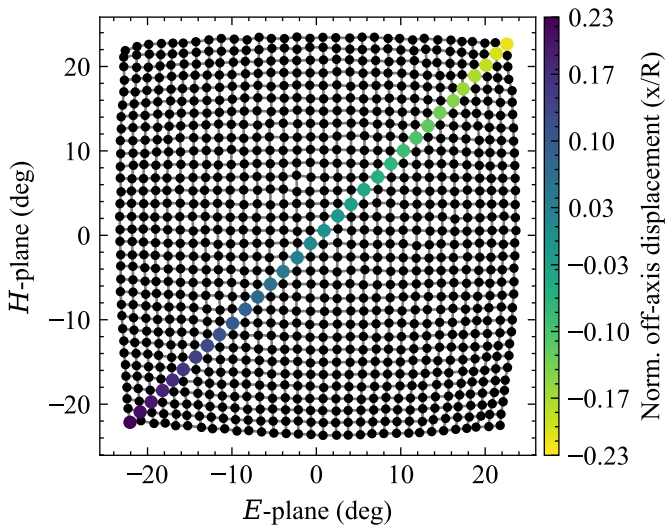

Figure 2.18. Measured beam incidence angle grid. Measured beam incidence angle grid, indicating barrel distortion; the colorbar describes the normalized off-axis displacement for camera pixels situated in the FPA diagonal. From [own15] © 2021 IEEE.

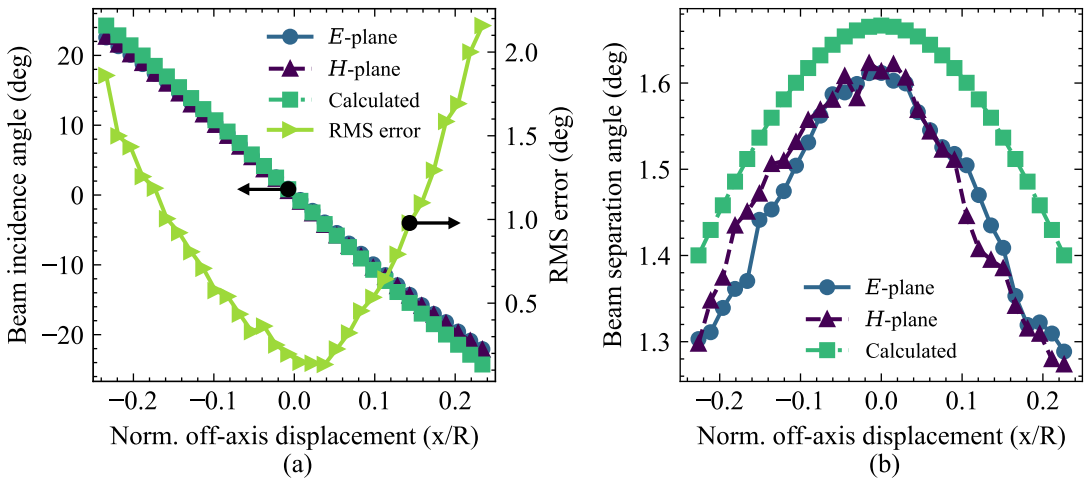

Figure 2.19. Beam incidence and beam separation angle. (a) Beam incidence angle values along the E- and H-plane for such pixels compared with calculated ones and the RMS error of calculated values based on measured ones, both plotted as a function of the normalized off-axis displacement. (b) Beam separation angle (the derivative of the beam incidence angle) as a function of the normalized off-axis displacement. Subfigure (a) is from [own15] © 2021 IEEE.

2.5.3 Discussions

The complete far-field radiation pattern analysis has provided both a qualitative and a quantitative picture of the image formation and associated resolution limitations of the CMOS THz camera. Off-axis aberrations in terms of HPBW or directivity variation across the FPA and radial distortion have been obtained from this analysis. Deteriorated performance in HPBW or directivity with respect to increasing distance from the optical axis has been observed, which is in agreement with previous findings from [19], [21], [107], [138], [139]. In addition, Barrel distortion has been identified, meaning that the beam separation angle decreases with increasing distance from the optical axis. It is remembered that HPBW and beam separation angle determine the crossover frequency between over- and undersampling frequency regions. Thus, it can be stated that this frequency shifts to higher frequencies for off-axis displaced camera pixels, and hence the room for resolution enhancement by super-resolution imaging is lower for such camera pixels or toward image edges. The results are general in nature and should apply to any broadband THz camera that employs an extended hemispherical dielectric lens with an elliptical focus along its optical axis.

2.6 Chapter Conclusion

In this chapter, the angular resolution limits of incoherent silicon integrated THz cameras using an extended hemispherical silicon lens have been identified for both low- and super-resolution imaging. A mathematical model was developed to predict the achievable frequency-dependent angular resolution for such cameras. All experimental studies were performed with the FPA from [21] coupled to a 15-mm diameter 2.75-mm extended hemispherical silicon lens. However, they are general in nature and therefore apply to any THz camera regardless of the FPA constitution and the design of the extended hemispherical dielectric lens.

The following has been found. The broadband operation causes regions of FoV over- and undersampling. The latter is due to narrow, non-overlapping pixel beams, which cannot be prevented for broadband operation, being the overarching aim in the first place. In such cases, super-resolution imaging can be employed to effect the maximum achievable angular resolution, which is to say, the diffraction-limited angular resolution given by the lens. A diffraction-limited resolution of 1.64° was achieved with the camera in the super-resolution imaging experiment performed

at 0.652 THz. Since this aligns closely with a conventionally employed criterion for determining the angular resolution of optical systems, namely the Sparrow criterion, this criterion can be used for prediction purposes. At 1 THz, the predicted angular resolution that can be achieved by using super-resolution imaging is 1.1°. This diffraction-limited angular resolution primarily depends on the frequency and the silicon lens dimensions. Besides a higher radiation frequency, a larger lens is advantageous in terms of angular resolution. However, for fixed FPA dimensions, a larger lens comes at the cost of a smaller FoV.

Although the angular resolution provides a more comprehensive picture of the achievable resolution, the spatial resolution ultimately determines the image quality in THz active imaging. To clarify, the spatial resolution combines the angular resolution and the camera-to-object distance. In other words, the spatial resolution is a 2-D function of the angular resolution and object magnification. THz active imaging has been demonstrated by coupling the camera to an optical train consisting of two lenses to build a collimated beam setup. This way, an object plane was created in between the two collimating lenses. The spatial resolution scales with the distance between the camera lens and the collimating lens in front of it. A measured spatial resolution of 1.43 mm was achieved in the experiments, which closely corresponds to the Sparrow criterion. A smaller object magnification would accompany a better performance. For example, a 1-mm spatial resolution could be reached at 0.652 THz using a 30-mm diameter collimating lens with an f-number of one, which will improve further for higher frequencies.

Every camera exhibits off-axis aberrations and radial distortion due to the hemispherical curvature of its objective lens. These aspects have been experimentally investigated for the CMOS THz camera. Regarding off-axis aberrations and radial distortion, it has been found that camera pixel beams broaden with increasing off-axis displacement, while their separating angle decreases because of Barrel distortion, which increases beam overlap toward images edges; this observation will hold for any camera of this sort. Consequently, the room for resolution enhancement by super-resolution imaging reduces with respect to increasing off-axis displacement.

Chapter 3

THz Dispersive Spectroscopy

3.1 Chapter Introduction

THz spectroscopy describes the analysis of the interaction between matter and EM THz waves [140]–[142]. Because of the see-through capabilities of THz waves, THz spectroscopy enables the examination of already packaged goods for material properties, which is of great use, for example, in industrial quality control. Established systems that can be used to perform THz spectroscopy are THz-TDS systems [10]–[12], [42] and THz-CWS systems [13]–[16]. As per the previous discussions in Chap. 1, they are outstanding in operating bandwidth, spectral resolution, and frequency accuracy but are incompatible with conventional microelectronics and have high manufacturing costs and low integration capabilities. For these reasons, they are currently only used for research purposes. In order to make THz spectroscopy accessible to broader society, the cost and size must be massively reduced.

THz spectroscopy systems implemented in silicon process technologies are superior over these above-discussed established solutions in terms of costs, size, and integration complexity, as described in Sec. 1.3. Recent research indicates that silicon-based front-ends offer a cost-effective alternative for THz gas spectroscopy. In particular, a 0.5-THz SiGe-HBT transmitter with 4.1% bandwidth [143] and a 0.245-THz SiGe-HBT sensor system with 4.5% bandwidth [144] have been presented. Most recently, dual-band operation allowed building SiGe-HBT transmitter and receiver components with 19.5% bandwidth around 0.246 THz [145]. However, these systems

are too narrowband to characterize spectral masks of solids. Due to required resonant LC impedance matching networks, it is impossible to realize coherently operated spectroscopy systems in silicon process technologies operating from DC to, say, 1 THz. In addition, power amplification above half of the maximum oscillation frequency, f_{max}, of transistors is not possible. One approach to overcome the bandwidth limitations is to operate multiple harmonics simultaneously [146], which is a form of THz signal comb generation and reception. The cited work has demonstrated multicolor imaging within a considerably large bandwidth of 0.16–1.05 THz, operating at multiples of the fundamental frequency of ∼164 GHz. However, contiguous spectral coverage is not achieved. In contrast, the approach of signal comb generation and reception based on pulse generation has emerged as a possible solution for medium-bandwidth THz spectroscopy applications [147], [148]. However, all these coherent systems lack the bandwidth requirements, for example, to characterize the spectral masks of solids or the harmonic content of THz radiation sources.

In contrast to the above coherent approaches, the realization of THz spectroscopy THz systems with silicon-based components by spatially mapping the radiation onto multiple antenna-coupled direct power detectors represents an incoherent approach. Silicon-based spatially-mapped systems have already been realized, such as SiGe-HBT on-chip spectroscopes based on a multimode antenna [149], [150] and dispersive spectroscopes based on a CMOS camera [own6], [own8]. Compared to coherent solutions, they are all far superior in terms of bandwidth. Although multimode antenna-based spectrographs are single-chip solutions, they require significant calibration and post-processing to extract frequency information. For these reasons, their range of practical applications is limited. In comparison, CMOS camera-based devices are superior in simplicity, scalability, and manufacturing costs. These advantages go hand in hand with a wider range of practical applications. For example, they can be used to characterize the harmonic content of THz radiation sources in free space. Upgraded with a suitable broadband THz radiation source, such as that presented in [151], solids could be inspected for their spectral masks. Other direct power detectors can, in principle, replace the CMOS detectors, such as microbolometers [152], CMOS nanoelectromechanical systems (CMOS-NEMS) [153], SiGe-HBTs [114], and Schottky barrier diodes [154].

This chapter starts by presenting the THz dispersive spectroscope presented in [own6] and providing results from experimental testing; for details of the design procedure, the associated optical simulations, and the manufacture of the mirror-type

spectrograph, the reader is referred to the cited work and the supplementary material given there. Unlike the spectroscopes presented in [own8], [155], [156], the herein presented device employs mirrors instead of lenses for beam manipulation, yielding better spectroscope efficiency due to less severe signal propagation losses, being beneficial to SNR. The main findings gained from experimental testing are that this spectroscope covers an operating bandwidth of ∼0.8 THz, but has only a moderate spectral resolution and frequency accuracy of several tens of gigahertz (GHz); bandwidth may be increased by using other dispersive optics targeting different design frequencies. Essentially, the spectral resolution and frequency accuracy are affected by the large operating bandwidth. The main reason is the limited number of camera pixels. Reducing the operating bandwidth for a better tradeoff in terms of the other performance parameters is not desirable. Given this fact, this chapter discusses the utility of super-resolution imaging for the spectroscope discussed here to compensate for the limited number of camera pixels. At this point in this thesis, this route seems to be the logical one to take since the spectroscope under discussion is based on the previously discussed CMOS THz camera, and we are now familiar with the concept of super-resolution imaging and its implications, following the discussions in Chap. 2. As we discussed in that chapter, super-resolution leads to a diffraction-limited angular resolution of the camera. The question arises whether or not this limit directly correlates to the spectral resolution of the spectroscope, which we anticipate since the frequencies are spatially mapped. Another question is whether super-resolution imaging continues to improve frequency accuracy to an infinite extent. To answer these questions, insights are provided into the fundamental performance limitations in terms of spectral resolution and frequency accuracy employing super-resolution imaging. The contribution of this chapter to knowledge is the demonstration of incoherent, spatially-mapped THz spectroscopy and to provide a general understanding of the fundamental frequency-dependent performance limits on the parameters discussed in the context of this application concept.

This chapter brings together some of the contents of [own6] and the contents of [own7]; another related work is [own8]. It is organized as follows. Section 3.2 describes the working principle of the THz dispersive spectroscope. In Sec. 3.3, the measured results of the extensive instrument tests performed as part of this thesis are compared with simulative expectations to verify the intended functionality. Section 3.4 is about the performance limits of such devices in terms of spectral resolution and frequency accuracy. Finally, a conclusion is drawn in Sec. 3.5.

3.2 THz Dispersive Spectroscope

Figure 3.1 shows a conceptual system view of the THz dispersive spectroscope. This device combines a CMOS THz camera and custom-machined spectrograph. The spectrograph bears two collimating mirrors and one reflective dispersive optic. Thereby, this spectrograph performs the spectral–spatial mapping, projecting each frequency of radiation emanating from a THz source to a different beam incidence angle of the camera. As we know, the camera lens maps each angle of incidence to a particular pixel. Consequently, a broadband beam emitted from a THz radiation source scans along a given central row of the FPA. This process converts the CMOS THz camera from an imaging device into a spectroscope. The beauty of this system is that it allows, for example, free-space spectrum analysis of THz radiation sources to determine their radiation frequency and harmonic content.

In order to transform this spectroscope into a silicon-only device capable of performing spectrometry, a THz source will be required, and the mirror-based optical subsystem must be expanded, as shown in the conceptual system view. In particular, additional collimating mirrors are needed to focus the source beam on where the THz source is located in the spectroscope configuration. Forming a focal point is necessary if an object is to be studied in the spectrometer configuration. In that case, one wants to ensure that all radiation passes through a material under a normal angle of incidence and is not deflected into a different direction, which would result in a systematic error that effectively reduces spectral resolution and frequency accuracy.

In the following, the most critical performance parameters of a THz dispersive spectroscope are introduced: spectral resolution and frequency accuracy. Of course, operating bandwidth is another important aspect besides these two parameters, but this one should be easy to understand and hence does not require any extra explanation.

3.2.1 Spectral Resolution

It is remembered that the spectroscope under investigation maps radiation of frequencies spatially. Because of this spectral–spatial mapping, the diffraction-limited spectral resolution of the spectroscope is associated with the Rayleigh criterion for two incoherent light sources. As we know from Sec. 2.2.1, the HPBW criterion is a close measure to the Rayleigh criterion, thereby being readily measurable and

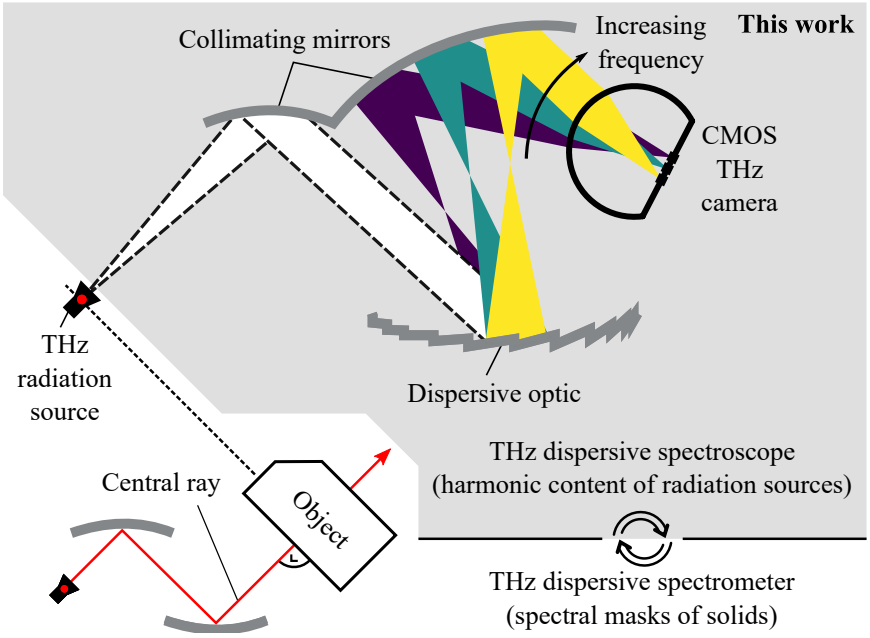

Figure 3.1. Conceptual system view of THz dispersive spectroscope. Conceptual system view of the mirror-based THz spectroscope using a CMOS camera and a dispersive optic. As shown, by converting the spectroscope into a spectrometer, one can replace the source with an object and thus characterize its material properties. For this purpose, the mirror-type optical subsystem (i.e., the spectrograph) must be extended by additional collimating mirrors that focus the source beam. For accurate spectrometry measurements, a normal angle of incidence must be ensured for the central ray. After [own7] © 2021 IEEE.

hence being applicable here in order to experimentally identify the diffraction-limited spectral resolution of the THz dispersive spectroscope. It should be noted that the diffraction-limited spectral resolution can only be achieved for a huge pixel count. To clarify, at least one separating pixel is required between two further ones to determine whether their intensity levels overlap at or above their HPBW. As we also know, the number of pixels can be boosted by super-resolution imaging. In this sense, the following gives a theoretical framework to describe the fundamental limits in terms of spectral resolution for low- and super-resolution imaging cases one after another.

Given the above, the spectral resolution of a THz dispersive spectroscope is associated with an incident two-tone signal. More precisely, it indicates the maximum resolvable frequency difference of such a signal. Assume that the number of pixels sets the limit for spectral resolution, as is the case, for example, with low-resolution imaging. In this case, the number of spectral peaks resolvable by such a spectroscope, $N_{\text{peaks,resolvable}}$,

is equal to half the number of the (used) camera pixels:

$$N_{\text{Peaks,resolvable}} = \frac{N_{\text{Pixels}}}{2}. \tag{3.1}$$

This is, essentially, because one pixel is always required between two others to identify a detectable dip, as shown in Figs. 3.2 (a) and (b). Consequently, for low-resolution, the average spectral resolution, $\delta\overline{f}_{\text{LR}}$, is

$$\delta\overline{f}_{\text{LR}} = \frac{BW}{N_{\text{Peaks,resolvable}}} = 2 \cdot \frac{BW}{N_{\text{Pixels}}}, \tag{3.2}$$

where BW is the bandwidth of the system (or subsystem) bandwidth, and N_{Pixels} represents the number of pixels into which this (sub)system bandwidth is mapped. An average spectral resolution is considered because the spectral–spatial mapping performed by the spectrograph may be of nonlinear nature. Let us assume that the number of pixels is not the limiting factor, as in super-resolution imaging. In this case, the spectral resolution limit discussed above can be broken [Figs. 3.2(c) and (d)]. According to Eqn. (3.2), the spectral resolution should approach a value of zero. However, this is not the case. In this case, the Rayleigh criterion must be considered, which we know from the previous discussion on the angular resolution limits of optical systems [Sec. 2.2.1]. It applies to a spectroscope of this type because spatially-mapped incident frequencies can be considered as different light sources. Thus, the angular resolution will limit the spectral resolution when the finite number of pixels is no longer the limiting factor. In terms of a mathematical expression, for super-resolution imaging, the average spectral resolution, $\delta\overline{f}_{\text{SR}}$, is:

$$\delta\overline{f}_{\text{SR}} = \frac{BW}{N_{\text{Pixels}}}. \tag{3.3}$$

Consequently, the average spectral resolution becomes the average pixel bandwidth when using super-resolution imaging to boost the number of camera pixels synthetically. To a first approximation, the pixel bandwidth of a spectroscope of this sort is the spectral representation of the angular resolution of the camera. This is not true in all circumstances, as each pixel receives a range of frequencies, and angular resolution is a frequency-dependent measure. However, the error should be negligible. Therefore, super-resolution imaging should enhance the spectral resolution at least by a factor of two compared to low-resolution imaging, provided that the angular resolution of the spectrograph is as good as or better than the angular resolution of

the camera. This assumption can be made since the spectrograph is larger than the camera lens, and we know that directivity scales with antenna size. Consequently, the angular resolution of the camera should be the limiting factor when it comes to super-resolution imaging in the context of a THz dispersive spectroscope. Therefore, the HPBW defines a convenient means to measure the spectral resolution.

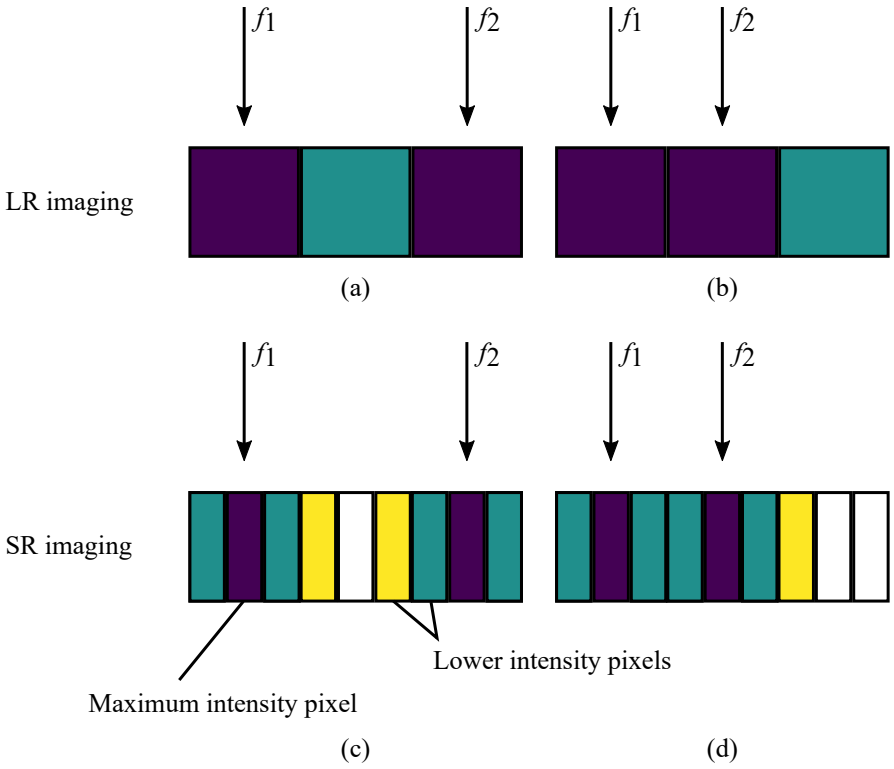

Figure 3.2. Effect of low- and super-resolution imaging on spectral resolution and frequency accuracy. The rationale for improving spectral resolution and frequency accuracy by using superresolution imaging. In (a), radiation from two incident frequencies, f_1 and f_2, excites two pixels separated by a third. In this case, f_1 and f_2 are resolved, and super-resolution imaging can only improve the frequency accuracy associated with the maximum intensity pixels, as indicated in (c). In (b), f_1 and f_2 exciting two adjacent pixels are unresolved, and super-resolution imaging can improve spectral resolution in addition to frequency accuracy, as shown in (d). From [own7] © 2021 IEEE.

3.2.2 Frequency Accuracy

In a THz dispersive spectroscope, the frequency accuracy describes the deviation of the measured frequency from that radiated by a source. In the spectroscope, it relates to the pixel of maximum intensity, as given in Fig. 3.2(c). Since this maximum intensity pixel determines the frequency accuracy, this performance

parameter is limited by a finite number of pixels like the spectral resolution, as becomes clear from inspection of Figs. 3.2(a)–(d). Therefore, synthetically increasing the number of pixels by super-resolution imaging will improve the performance of a THz dispersive spectroscope in terms of frequency accuracy {[Fig. 3.2(a) versus Fig. 3.2(c)] and [Fig. 3.2(b) versus Fig. 3.2(d)]}. For low-resolution imaging, the limit of average frequency accuracy should be the average pixel bandwidth, to a first approximation. For super-resolution imaging, there is, in principle, no limit on the frequency accuracy. Ultimately, however, the frequency accuracy will be limited by the interaction of various noise sources, including pixel noise, measurement alignment inaccuracy, and the surface tolerances of the optical components.

3.3 THz Dispersive Spectroscope Testing

This section provides the results of the THz dispersive spectroscope characterization concerning spectral–spatial mapping, efficiency, and spectral resolution. Thereby, two dispersive optics were employed to test different design frequencies of 0.85 THz and 0.46 THz to demonstrate the modularity of the spectroscope. In the course of this chapter, the dispersive optic concerned with the higher frequency is referred to as "dispersive optic #1," while the one concerned with the lower frequency is referred to as "dispersive optic #2." In the following, the experiment and the measured results are subsequently discussed.

3.3.1 Experiment

The experimental setup shown in Sec. 3.3 was employed to test the THz dispersive spectroscope for its performance in terms of spectral–spatial mapping, efficiency, and spectral resolution. In this experiment, a widely tunable, spectrally-clean continuous-wave (CW) THz photo-mixer emitter[1] was employed. This source is a favorable candidate because of its large bandwidth of 0.035–1.32 THz and its spectral purity, with a frequency accuracy of 20–30 kHz. Thereby, the source radiation power varies between ∼300 µW at 0.35 THz and ∼2.5 µW at 1 THz. It is noted that the transverse magnetic (TM) polarization with respect to the spectrograph was used because of its greater diffraction efficiency at the design

[1]https://www.toptica.com/products/terahertz-systems/frequency-domain/terascan/

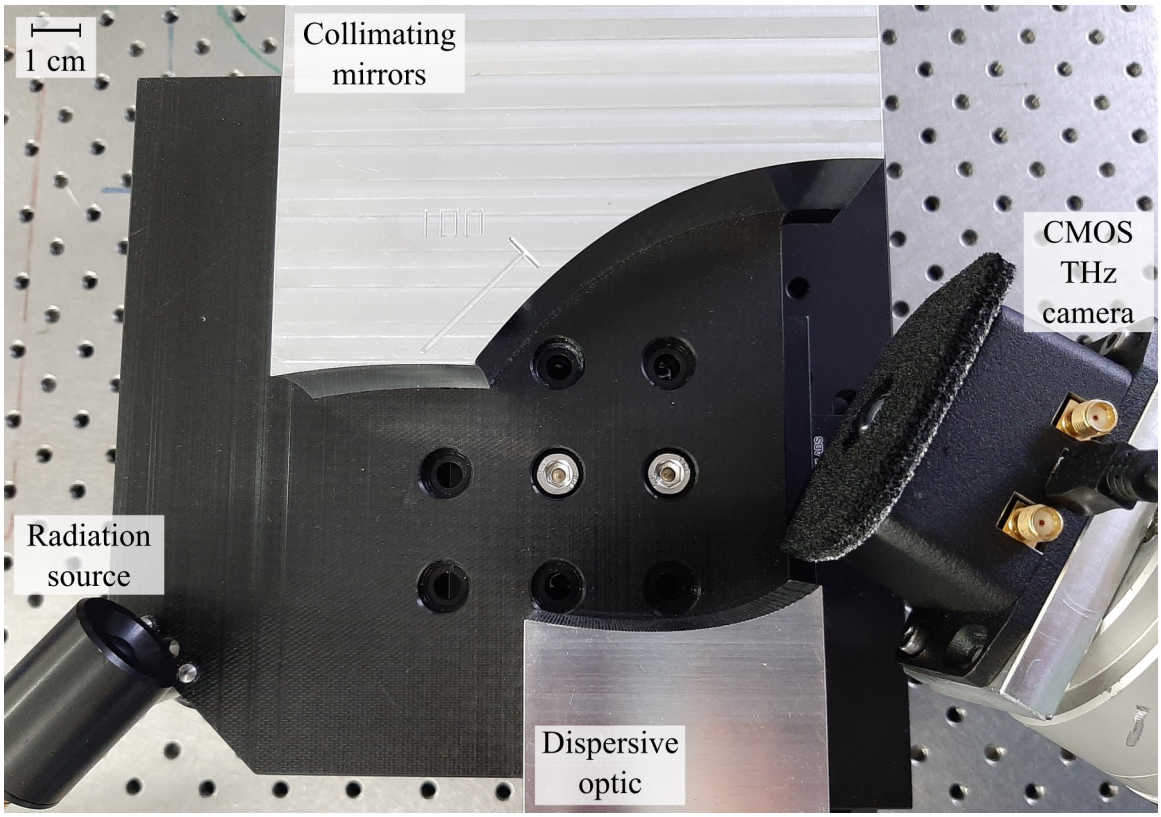

Figure 3.3. Experimental setup for spectroscope testing. Photograph of the experimental setup employed to characterize the THz dispersive spectroscope composed of two collimating mirrors combined in a single metal block, a dispersive optic, and a CMOS THz camera. For spectroscope testing, a broadband photomixer-based THz radiation source was employed because of its spectral purity. After [own6] © 2020 IEEE.

frequency, as identified through full-wave simulations performed in high-frequency structure simulator (HFSS)[own6].

In terms of the measurement procedure, the spectroscope employing dispersive optic #1 was tested first by sweeping the source radiation frequency in the range from 0.4–1.2 THz, while the camera readout was extracted at 1-GHz intervals. Frame averaging of 1024 frames was applied to improve upon SNR, according to [own4]. Following this, dispersive optic #1 was replaced with the lower-frequency element, namely dispersive optic #2, and the experiment was repeated from 0.1–1.2 THz.

3.3.2 Measured Results

In this section, measured results concerning spectral–spatial mapping, efficiency, and spectral resolution are conducted. Spectral–spatial mapping and efficiency were

analyzed for both dispersive optics targeting different frequency bands to demonstrate the modularity of the spectroscope. Unlike the spectral–spatial mapping and efficiency, the analysis of the spectral resolution is restricted to dispersive optic #1 because it fits the camera better in terms of frequency, which results in better SNR and thus more accurate measurements. This section is organized as follows. First, a qualitative picture of the spectral–spatial mapping is transported by showing a set of selected images (or 2-D camera readouts) using dispersive optic #1. Thereafter, results are limited to 1-D camera readouts of the given rows probed using both dispersive optics to transport a quantitative picture. Efficiency is treated before closing this section by handing the results obtained from the spectral resolution analysis.

3.3.2.1 2-D Camera Readouts at Selected Frequencies

Figure 3.4 shows a set of images obtained from measurements performed from 0.7–1 THz using dispersive optic #1 to provide a qualitative picture of the spectral–spatial mapping and associated aspects. Each image is normalized to the maximum of the entire frequency scan, and they are shown on a logarithmic scale. From inspection of this figure, several things become clear. First, radiation is centered upon a given central row, as indicated by the dashed lines. Second, radiation moves from the left to the right as the frequency increases, which means that the beam scans along a given row. And third, the SNR varies with respect to frequency.

3.3.2.2 1-D Camera Readouts Using Probed Row

Figure 3.5 shows normalized 1-D camera readouts as a function of the frequency, with (a) obtained using dispersive optic #1 and (b) to dispersive optic #2. Each column in these image plots corresponds to a 1-D camera readout at a particular frequency; here, row #15 was selected because the alignment was performed such that the direction of the beam associated with the design frequency coincides with the optical axis of the lens, as indicated by the horizontal and vertical lines. In other words, the alignment was done so that the beams of the design frequencies landed upon the very center camera pixel. The shown 1-D camera readouts further confirm the findings observed from inspection of their 2-D counterparts.

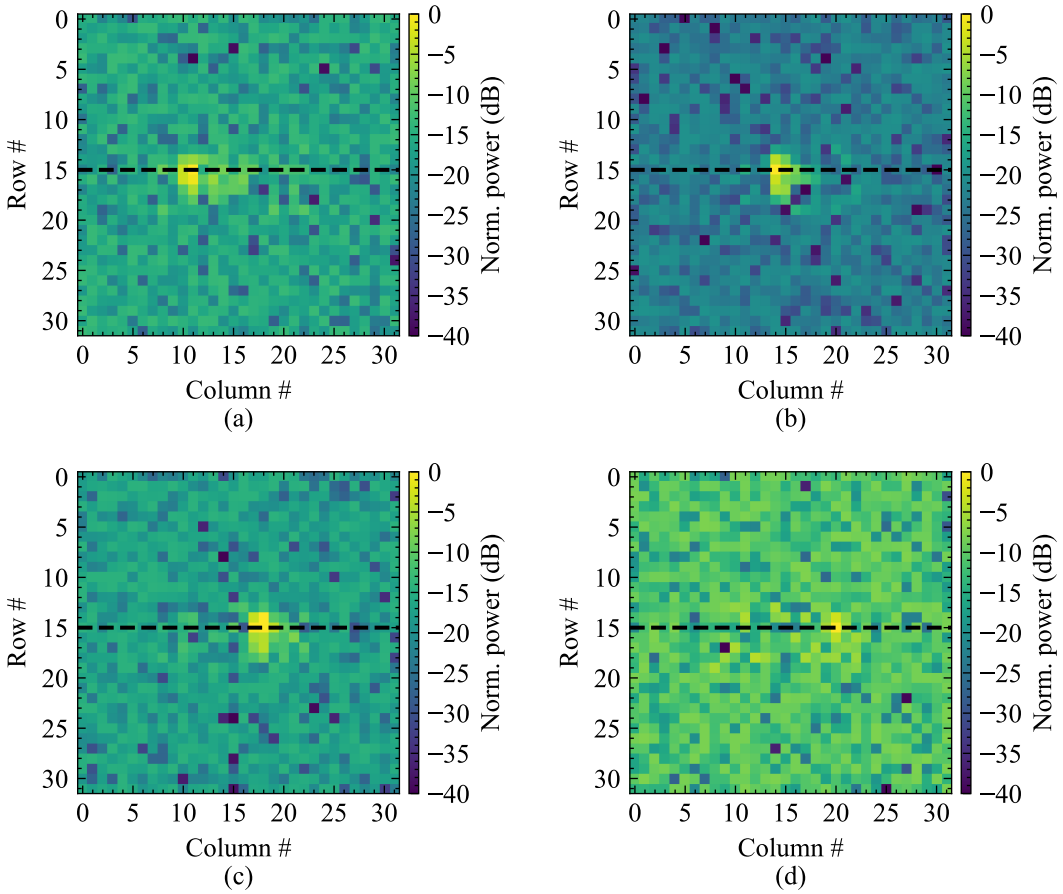

Figure 3.4. 2-D camera readouts at selected frequencies using dispersive optic #1. Normalized power obtained from the 2-D camera readout at specific frequencies [(a) 0.7 THz, (b) 0.8 THz, (c) 0.9 THz, (d) 1.0 THz] using dispersive optic #1.

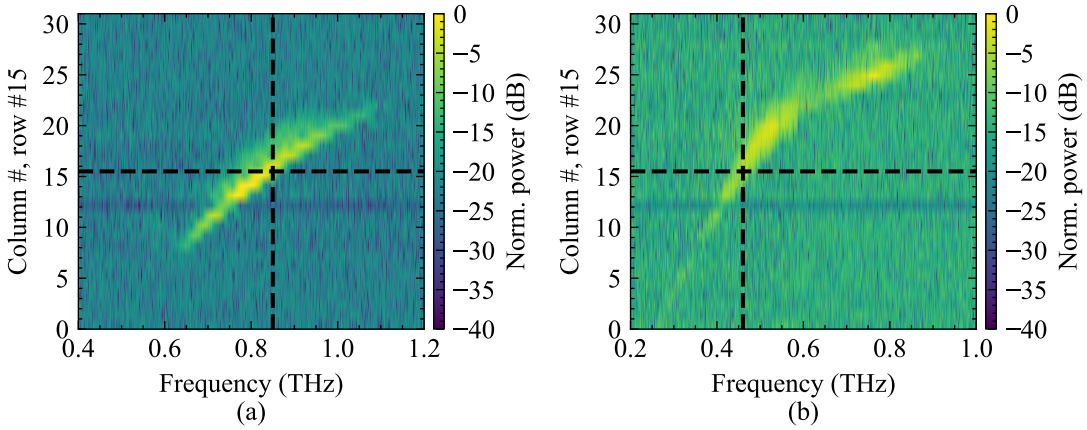

Figure 3.5. 1-D Camera Readouts of Probed Row. Normalized power as a function of the frequency using the dispersive optic #1 (a) and dispersive optic #2 (b).

3.3.2.3 Spectral–Spatial Mapping

Figure 3.6 shows the spectral–spatial mapping obtained from 1-D camera readouts for both dispersive optics compared to the expectations from the simulations.

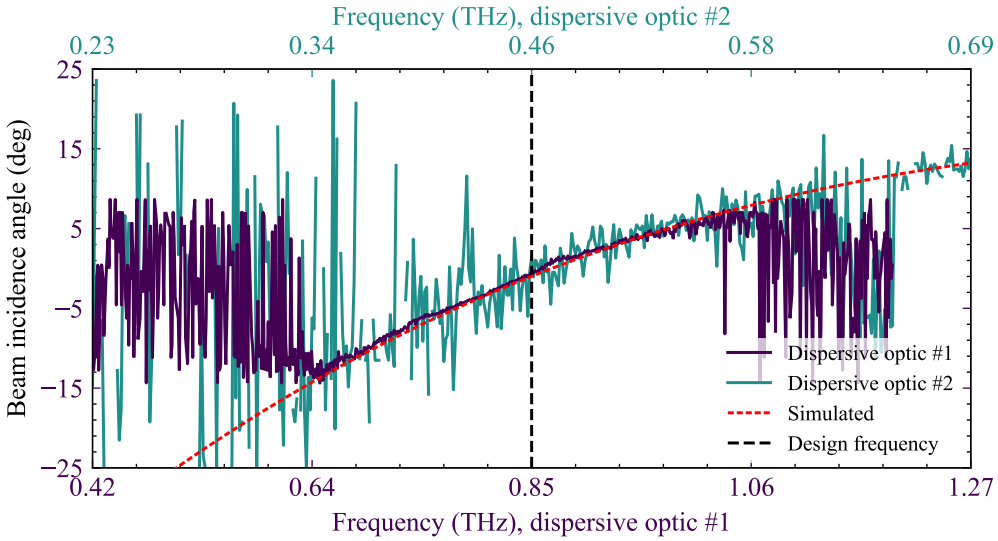

Figure 3.6. Spectral–spatial mapping. Spectral–spatial mapping of the spectroscope device, as extracted from the camera readout, for both dispersive optics tested. The measured results are plotted along with simulated ones for comparison between measurement and expectation. After [own6] © 2020 IEEE.

The measured trends were obtained by calculating the center of gravity for each frequency using the data shown in Fig. 3.5. Thereby, a global threshold of 0-dB SNR was applied to reduce the effects of noise that can obscure the pattern of incidence radiation on the camera. These calculated values were converted to a beam incidence angle via a geometric argument [Eqn. (2.4)]. The simulated trend of the beam incidence angle upon the THz camera was extracted from the Huygens' principle-based simulation detailed in [own6]. From this figure, it can be seen that good agreement is obtained with the overall trend of the simulated results. However, there is a non-negligible deviation in the measured results, especially at frequencies below 0.5 THz and above 1 THz. This deviation can be attributed to the low SNR. The peak signal-to-noise ratio (PSNR) was evaluated as a function of frequency. The PSNR achieved is 28.8 dB and 11.0 dB for dispersive optics #1 and #2, respectively. The lower SNR in the case of the lower-frequency element is due to the frequency mismatch between camera and radiation source. Although the low SNR does not affect the incident angle of the beam itself, it affects the weighted average used to determine the center of gravity. Since NEP of the THz camera and the diffraction

efficiency of the dispersive optic are both highest near 0.85 THz, a degradation of the SNR away from this frequency is expected.

3.3.2.4 Efficiency

It is desirable to characterize the efficiency of the spectroscope to determine its useful bandwidth. This efficiency includes diffraction efficiency of the dispersive element, beam shape mismatch between the spectrograph and camera lens, and Fresnel losses at the camera lens surface due to oblique incidence. In order to determine this efficiency, the results of the spectroscope measurements must be compared with reference measurements made based on a single collimating mirror. To this end, the experimental setups that are shown in Figs. 3.7 (a) and (b) were used, where (a) is the spectroscope configuration and (b) is the reference configuration. The efficiency was calculated as the ratio of power obtained from the spectroscope measurements to that from reference measurements, both integrated over 2-D camera readouts. This procedure was applied to both dispersive optics. To this end, they were exchanged during the experiments without altering the optical alignment. In both spectroscope and reference measurements, the camera readout was averaged over a total of 1024 frames to improve SNR, according to [own4]. The measured efficiency of the spectroscope is shown in Fig. 3.8.

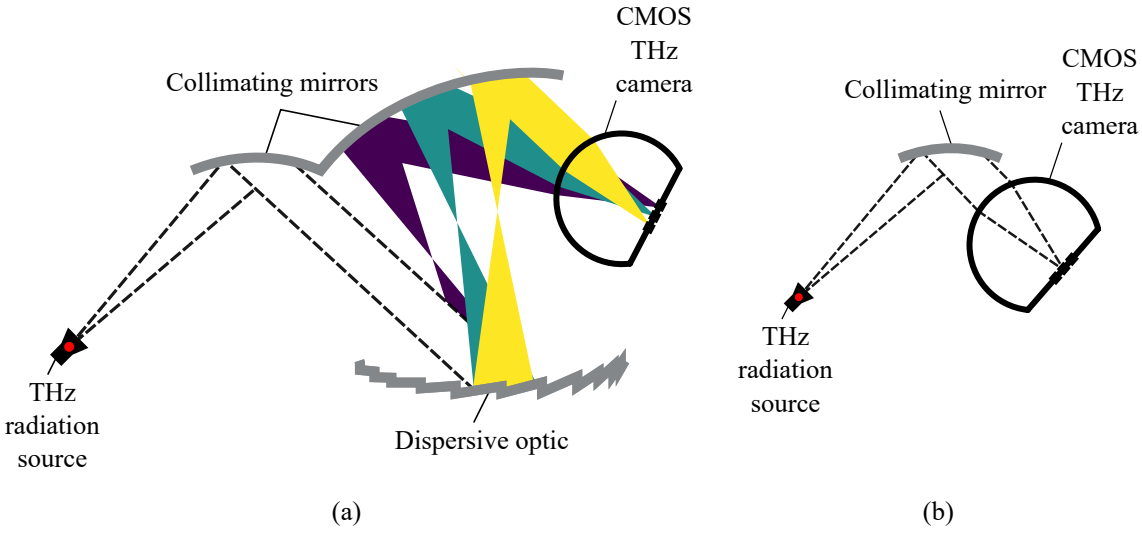

Figure 3.7. Experimental setups for efficiency determination. Illustrations of the experimental setups employed to determine the efficiency of the spectroscope, showing (a) spectroscope configuration and (b) reference measurement. By relating integrated power from spectroscope measurements to that from reference measurements, the efficiency of the spectroscope can be determined. After [own6] © 2020 IEEE.

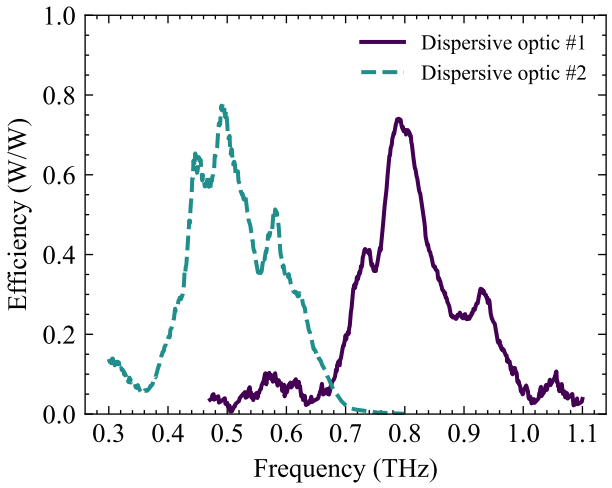

Figure 3.8. Measured efficiency of spectroscope. The overall efficiency of the THz dispersive spectroscope as a function of the frequency using the two dispersive optics targeting different frequency bands, taking into account not only losses due to diffraction efficiency but also those due to camera scan loss. After [own6] © 2020 IEEE.

From inspection of Fig. 3.8, it is evident that the efficiency decreases progressively as the frequency deviates from that associated with peak efficiency. This diminishing efficiency contributes to the fluctuations in spectral–spatial mapping shown in Fig. 3.6. In the context of that figure, it has been stated that the variation in spectral–spatial mapping results increases significantly at frequencies above 1 THz, for example. In Fig. 3.8, it can be seen that the overall efficiency of the spectroscope has decreased to ∼5% in this range. A transition is observed near 0.68 THz, where both dispersive optics have low efficiencies of ∼5%. Therefore, neither of the dispersive optics provides high SNR in this range. To address this issue, it may be beneficial to further exploit the modularity of the spectroscope by developing a third dispersive optic that targets a center frequency of 0.68 THz. Similarly, the total usable bandwidth of the spectroscope can be extended by adding additional dispersive optics. The ability to exploit the modularity of the optical subsystem provides a route to realizing low-cost spectroscopes covering the 0.15–1.50 THz band, which is a decade of THz bandwidth.

3.3.2.5 Spectral Resolution

Following previous discussions [Sec. 3.2.1], multiples of the pixel bandwidth (1× and 2× pixel bandwidth) were determined from the frequency-response data shown in Fig. 3.9(a) using the HPBW criterion, restricting it to the dispersive optic #1 since it provides better SNR than the other dispersive optic developed, and the

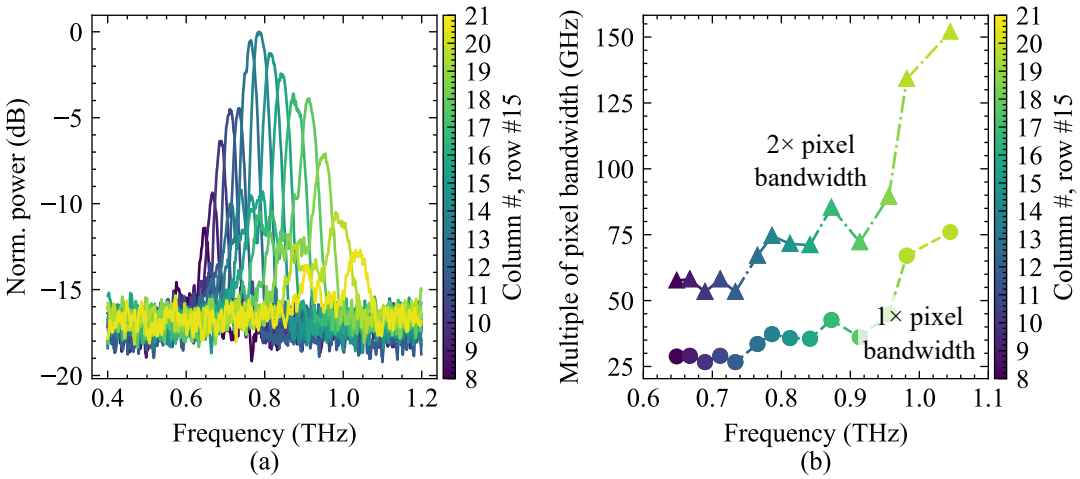

Figure 3.9. Analysis of spectral resolution using low-resolution imaging. (a) Normalized sum of radiation power incident upon column #'s of the FPA. (b) Multiples of the pixel bandwidth extracted as the HPBW from corresponding curves plotted in (a). Here, "2× pixel bandwidth" represents the pixel column#-dependent spectral resolution of the spectroscope device, while 1× pixel bandwidth refers to the theoretical limit employing super-resolution imaging. After [own6] © 2020 IEEE.

result is shown in Fig. 3.9(b). It is remembered that pixel bandwidth refers to the range of frequencies seen by a camera pixel in spectroscope configuration. In both figures, the colors of the plotted lines refer to the column # corresponding to the pixel under investigation at fixed row #15, recognizable via the respective colorbars. As we know from Sec. 3.2.1, "2× pixel bandwidth" relates to the spectral resolution limited by a finite pixel count, while "1× pixel bandwidth" relates to the diffraction-limited spectral resolution. Both trend upward as the frequency increases, which is attributed to the nonlinear behavior of the spectrograph: lesser and lesser pixels are used toward higher frequencies for spectral–spatial mapping. Low-resolution imaging is associated with an average spectral resolution of 78.4 GHz, and super-resolution imaging is, theoretically, associated with a spectral resolution of 39 GHz on average. The spectral resolution limit using super-resolution imaging must be verified with another experiment, elaborated in the following.

3.4 Performance Limits in Spectral Resolution and Frequency Accuracy

As elaborated until this point, the performance of the THz dispersive spectroscopes is limited in spectral resolution and frequency accuracy due to a finite pixel count.

This section demonstrates that increasing the synthetic effective pixel count by exploiting super-resolution imaging improves the performance. In addition to conducting how to achieve enhanced spectral resolution and frequency accuracy, the experimental analysis presented here gives insights into the fundamental performance limits of spectral resolution and frequency accuracy. Specifically, super-resolution is aimed toward reaching the diffraction-limited spectral resolution given as "1× pixel bandwidth" in Fig. 3.9. In addition, it aims to improve frequency accuracy substantially. Because of SNR limitations concerned with spectroscope efficiency constraints, the efforts were concentrated on analyzing the spectroscope from 0.75–0.9 THz. Next, the super-resolution imaging method employed is explained. After that, details regarding the experiment and the measured results are provided.

3.4.1 Method of Super-Resolution Imaging

Sections 3.2.1 and 3.2.2 have motivated the use of super-resolution imaging to improve spectral resolution and frequency accuracy. Here, the method employed previously in the frame of Chap. 2 [Sec. 2.3] was used but restricted to one dimension. In contrast to that method, the acquisition of 1-D vectors is sufficient here, as it is not necessary to probe all 1024 camera pixels because a broadband beam scans along a given central row of the camera. Accordingly, a simplified version of the super-resolution algorithm from Eqn. (2.13) was used, illustrated in Figure 3.10. This illustration is an example based on three 1-D low-resolution vectors. The entire process is scalable, with the pixel count of the 1-D super-resolution vector determined by the number of pixels in a pixel row and the number of low-resolution 1-D vectors.

In very general terms, the 1-D super-resolution vector can be described as

$$SR = \left(LR_{0,0}, LR_{0,1}, LR_{1,0}, LR_{1,1} \quad \dots \quad LR_{\mathrm{I,J}}\right), \tag{3.4}$$

where $LR_{\mathrm{i,j}}$ contains information of a single camera pixel with the column #, i, situated in a given pixel row at a certain predictable angular position, j. Dithering is realized by rotation around the center of the camera lens. As illustrated in Fig. 3.10(b), this form of rotation entails moving along an FPA row. This movement essentially represents a radiation pattern scan for each pixel, limited to a rather small angular range.

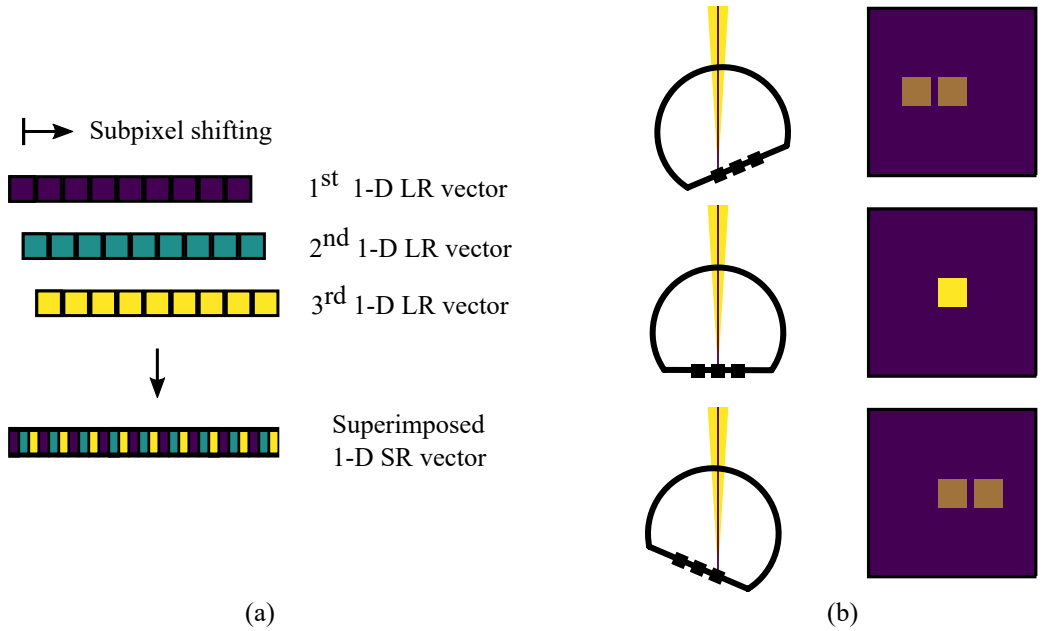

Figure 3.10. Super-resolution imaging method. (a) Illustration of the geometrical multi-frame super-resolution algorithm used in this work. Several 1-D low-resolution vectors acquired at angular offsets are combined into a 1-D super-resolution vector through subpixel shifting. (b) Illustration of the measurement procedure to acquire multiple low-resolution images or 1-D low-resolution vectors at angular offsets. Rotation around the camera lens center causes incident radiation to move along the FPA. After [own7] © 2021 IEEE.

3.4.2 Experiment, Measured Results, and Discussions

3.4.2.1 Experiment

The experimental setup used to perform the super-resolution imaging experiment to examine the performance limits of the spectroscope in terms of spectral resolution and frequency accuracy is essentially the same as the one shown earlier in [Fig. 3.3]. Here, a 0.75–0.9 THz CW radiation source with a 24.9–26.5 dBi standard gain horn antenna was used. The camera was attached to a six-axis table-top UR5 robot arm for rotation. In the frequency range of interest, the radiation power of the source ranges between 0.5 µW and 8.8 µW, and the integrated video-rate NEP of the camera and the efficiency of the spectroscope (dispersive optic #1) are between 17.6 nW and 36.2 nW [own14] and 24.3% and 71.1% [own6], respectively.

In terms of the measurement procedure, the camera was horizontally scanned over a total of 1.66° angular range, corresponding to the beam separation angle between two adjacent pixels, with 1.66°/22 intervals. At each position of this rotational scan, the source was swept from 0.75–0.9 THz at 1-GHz intervals. The camera

readout was averaged over 1024 frames to achieve an PSNR greater than 30 dB for all source radiation frequencies within 0.75–0.9 THz, according to [own4]. With this, the measurement lasted 75 minutes.

Regarding data post-processing, the super-resolution 1-D vectors were produced using Eqn. (3.4). Super-resolution 1-D vectors are superior over their low-resolution counterparts in terms of pixel count (704 subpixels) and angular resolution, aiming at improving spectral resolution and frequency accuracy of the spectroscope, thereby identifying fundamental performance limits in these parameters.

3.4.2.2 Measured Results and Discussions

Figs. 3.11 (a) and (b) show normalized 1-D camera readouts as a function of the frequency for low- and super-resolution imaging, respectively. As can be observed qualitatively, super-resolution imaging supports the identification of more spectral features because of the improved angular resolution of the camera and better PSNR [Sec. 2.3]. The two vertical strikes observable in the super-resolution image are due to pixel-to-pixel variations in terms of responsivity.

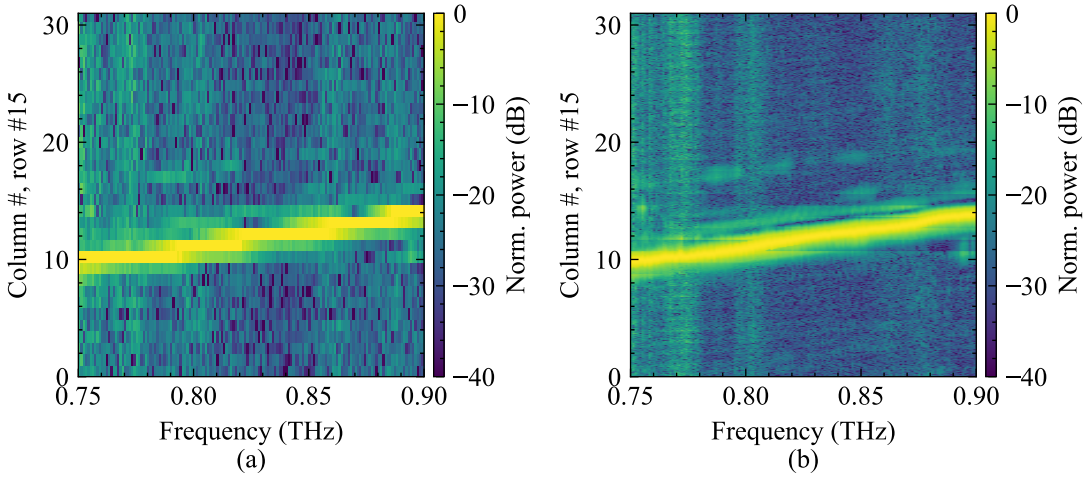

Figure 3.11. 1-D camera readouts of probed row. The normalized power as a 2-D function of frequency and column # and subpixel column # using low-resolution (a) and super-resolution (b) imaging, respectively, by stacking row #15. After [own7] © 2021 IEEE.

Figure 3.12(a) shows the spectral resolution and pixel bandwidth as a function of the frequency. The spectral resolution was extracted from normalized 1-D super-resolution vectors using the HPBW, following the previous discussions

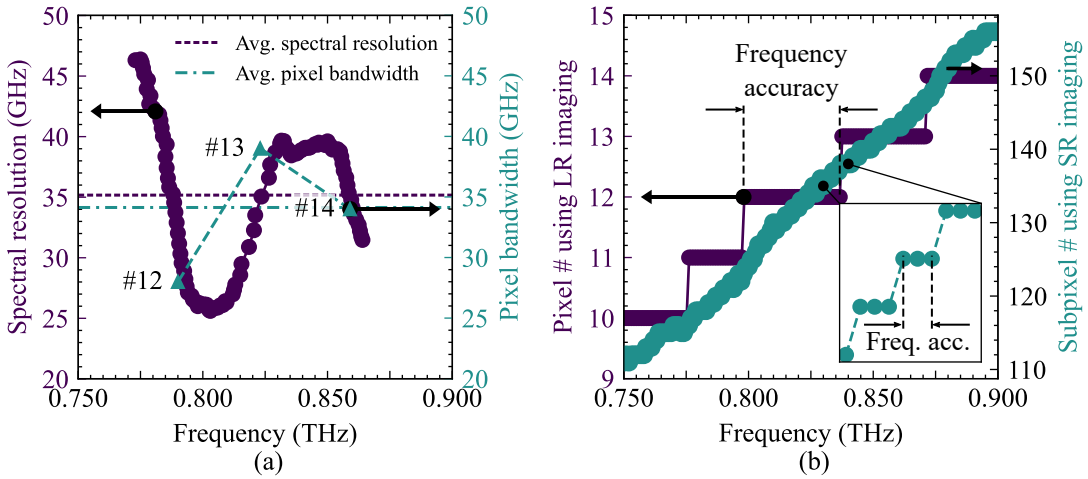

Figure 3.12. Measured spectral resolution and frequency accuracy. (a) Spectral resolution using super-resolution imaging compared with pixel bandwidth. (b) Maximum intensity pixel #- and subpixel#-to-frequency mapping using low-resolution and super-resolution imaging, respectively. After [own7] © 2021 IEEE.

from Sec. 3.2.1. These vectors were normalized to determine spectral resolution independent of frequency-dependent spectroscope sensitivity and source radiation power. The pixel bandwidth values were determined by inspection of the single-pixel responses with respect to frequency, considering the HPBW. From inspection of this figure, it is evident that super-resolution imaging entails achieving an average spectral resolution of about as low as the average pixel bandwidth. In numbers, the spectral resolution achieved on average is 35.17 GHz, while the average pixel bandwidth is 34.15 GHz. It should be noted that the spectral resolution varies. Specifically, it fluctuates within an RMS deviation of 5.95 GHz; a similar trend is observed for pixel bandwidth. The pixel-to-pixel transitions observable from inspection of Fig. 3.11 may explain the wavelike trends. This study confirms that super-resolution imaging enhances the average spectral resolution by at least a factor of two compared to low-resolution imaging [own6], as intended. Therefore, the factor that sets the limit on the spectral resolution is apparent: it is the angular resolution of the camera pixels.

Figure 3.12(b) shows maximum intensity pixel #-to-frequency and maximum intensity subpixel #-to-frequency mapping generated using low- and super-resolution, respectively. From these trends, the frequency accuracy was determined as the frequency step size for which a monotonically increasing (sub)pixel column #-to-frequency mapping holds, as indicated in this figure. While low-resolution imaging yields an average frequency accuracy of 30 GHz, super-resolution imaging improves this to 1.65 GHz. The improvement in frequency

accuracy is a factor of 18.2. It is remembered that 22 low resolution 1-D vectors were used to produce a super-resolution 1-D vector. Pixel noise, measurement alignment inaccuracies, and surface tolerances of the camera lens and spectrograph are factors that prevent achieving the theoretical maximum improvement of 22.

Table 3.1 compares the performance obtained here with that of state-of-the-art silicon-based THz spectroscopy systems. In comparison, a large bandwidth is achieved at moderate spectral resolution and considerable frequency accuracy, at least for super-resolution imaging. Furthermore, the best power consumption by far is achieved.

Table 3.1. Silicon-based THz sepctroscopy systems. A comparison of the performance achieved here to that of state-of-the-art silicon-based THz spectroscopy systems of both incoherent and coherent nature. After [own7] © 2021 IEEE.

Reference	Technology	System operation mode	Operating bandwidth (THz)	Avg. spectral resolution (GHz)	Avg. frequency accuracy (GHz)	DC power consumption (mW)
[143]	130-nm SiGe	Coherent	0.238–0.245	0.00138	≤0.00138	1,467
[144]	130-nm SiGe	Coherent	0.494–0.5	0.0005	≤0.0005	1,100
[145]	130-nm SiGe-BiCMOS	Coherent	0.222–0.270	-	-	-
[146]	250-nm SiGe-BiCMOS	Coherent	0.16–1.05[a]	-	-	600
[147]	90-nm SiGe-BiCMOS	Coherent	0.050–0.5	16.67	-	40
[148]	130-nm SiGe-BiCMOS	Coherent	0.1–1.1	-	-	45
[149]	130-nm SiGe-BiCMOS	Incoherent	0.04–0.33	0.01	≤0.01	212
[150]	130-nm SiGe-BiCMOS	Incoherent	0.04–0.99	0.01[b]	0.01	212
[own8]	65-nm CMOS	Incoherent	0.35–0.5/0.7–0.825	-	-	0.035[f]
This work	**65-nm CMOS**	Incoherent	**0.6–1.1**[c]	**78.4**[d]**/39.2**[e]	**30**[d]**/1.65**[e]	**0.035**[f]

[a]Divided into six subbands; [b]predicted from calculations, [c]can be increased by other dispersive optics, [d]using low-resolution imaging, [e]using super-resolution imaging; [f]for 14 pixels probed, following [21].

3.5 Chapter Conclusion

In this chapter, the application concept of THz dispersive spectroscopy has been demonstrated, which is based upon extending an incoherent silicon integrated THz camera with dispersive optics. This spectroscope functions similarly to a prism spectroscope. Therefore, each frequency is mapped into a particular camera pixel. The beauty of this system is its broadband operation, which takes advantage of the broadband incoherent detection mode of the camera. The broad bandwidth has been experimentally verified regarding spectral–spatial mapping and efficiency for two dispersive optics targeting different frequency bands, demonstrating modularity by changing the dispersive optic without changing the optical alignment. Specifically, two dispersive optics with design frequencies of 0.46 THz and 0.85 THz ended up covering the 0.3–1.1 THz band; other dispersive optics may be employed to increase the bandwidth further. The capabilities of this incoherent system approach far exceed those of coherent systems in terms of bandwidth. However, the considerable operating bandwidth of the spectroscope is achieved at the cost of low spectral resolution and frequency accuracy. This is where super-resolution imaging comes into play. To clarify, the low spectral resolution and frequency accuracy are caused by the limited number of pixels in the camera, as the broadband operation was the overarching aim in the first place. Super-resolution imaging can be used to increase the synthetic effective pixel count. By this, the spectral resolution was enhanced from 68.3 GHz to 34.2 GHz (factor of 2), while the frequency accuracy was improved from 30 GHz to 1.65 GHz (factor of 18.2).

Super-resolution imaging will be of general use as a technique for a THz dispersive spectroscope to effect maximum achievable spectral resolution and substantially improve upon frequency accuracy. The minimum improvement in spectral resolution expected from this technique is a factor of two, thereby reaching the angular resolution limit of the camera. Assuming sufficiently high SNR is realized, the frequency accuracy should scale approximately with the number of low-resolution images acquired to produce a super-resolution image. A larger lens would be required to improve the spectral resolution further, allowing the camera to reach a better diffraction-limited angular resolution. However, a larger lens is not only associated with better angular resolution but also with a lower FoV. Thus, there is a design tradeoff between spectral resolution, frequency accuracy, and operating bandwidth for a spectroscope of this sort related to the choice of the camera lens.

Chapter 4

THz Compact Antenna Test Range

4.1 Chapter Introduction

For both THz active imaging and the sensitivity characterization of THz receivers, it is crucial to know the far-field characteristics of the radiation source used, such as shape, profile, directivity, HPBW, and radiation power. Regarding THz active imaging, beam artifacts can be distinguished from an illuminated object if the far-field radiation pattern of the source is known. Concerning sensitivity characterization of THz receivers, radiation power incident upon a receiver can be calculated using the Friis transmission equation if both the directivity and the radiation power of the source are known. That is why it is crucial to determine the far-field radiation pattern of a THz radiation source. The problem with this is that it is often impractical or impossible at a far-field range [157]. THz antenna measurements typically last hours—for a single radiation frequency. When broadband sources are concerned, this can quickly scale up to several days. Moreover, a second measurement setup based on an absolute power meter is typically required to determine the radiation power.

With the above constraints in mind, far-field radiation patterns are often estimated from near-field measurements. Mainly three techniques are known for accomplishing this [158]. The first technique employs near-field distributions of amplitude and phase measured with a scanning probe. Numerical calculations can then be utilized to produce the far-field radiation pattern based on Huygen's principle. In the second technique, the AUT is focused in its radiative near-field region. Here, near-field radiation patterns are recorded and subsequently refocused to infinity. The third

technique is about CATRs. In conventional CATRs, a feed-coupled collimating optic outputs approximately plane EM waves incident upon an AUT, thereby creating far-field conditions at a compact range. Historically, a radiation source has been used as a feed to characterize the AUT of a receiver. On the other hand, this approach has also been used for radar cross section (RCS) measurements [159]. Accepted collimating optics are dielectric lenses [158], [160]–[163] and reflectors [158], [164], [165]. The main benefit of CATRs over the other two methods is their compact design, accompanied by the fact that no additional computation is required to produce far-field radiation patterns. At THz frequencies, a different type of devices has been realized, namely hologram-type THz CATRs [166], [167], which are advantageous in terms of size. In this chapter, a novel THz CATR concept using the previously discussed CMOS THz camera is presented for single-shot radiation pattern characteristics determination of sources. The main advantage over existing solutions is that the time required to produce a far-field radiation pattern is substantially reduced since no mechanical sampling is needed, in principle. Moreover, only one measurement setup is required to measure all far-field characteristics of radiation sources, as the camera pixels are direct power detectors, which perform absolute power measurements.

This chapter examines how suitable this solution is. To this end, the THz CATR was tested for its performance in terms of determining the far-field characteristics using a broadband 0.6–1.1 THz radiation source equipped with a 23.7–28.2 dBi standard gain horn antenna. Measurements performed with the THz CATR are carefully compared to reference measurements and full-wave simulations to analyze its performance in determining directivity, HPBW, and radiation power. In this context, single-frame low- and geometrical multi-frame super-resolution are compared. Super-resolution imaging is anticipated to improve upon the determination of the far-field characteristics due to an improved pixel count coupled with an enhanced angular resolution, as per the previous discussions from Chap. 2. Camera-related limitations for measuring far-field radiation patterns using THz CATR are also discussed, such as FoV limitations, angular resolution limitations, and scan loss, with the first two compromising minimum and maximum inspectable AUT size. AUT size limitations are derived, and in this regard, the design of new devices is discussed. The contribution of this chapter to knowledge is the novel THz antenna measurement concept to facilitate a convenient means for determining far-field

radiation pattern, directivity, HPBW, and radiation power of a source—over an immense bandwidth within of just a few minutes.

This chapter is a modified version of [own9], and it is outlined as follows; other related works are [own10]–[own12]. Section 4.2 discusses the working principle of the presented THz CATR. AUT size limitations are treated in Sec. 4.3, and scan loss as well as its calibration is discussed in Sec. 4.4. Section 4.5 is about the extensive elaboration of the experimental results of the THz CATR testing. The design considerations to build new THz CATRs are discussed in Sec. 4.6, before Sec. 4.7 concludes this chapter.

4.2 Working Principle

To understand the working principle of the CMOS camera-type THz CATR, we first look at the definition of near-field and far-field approximations, following Fig. 4.1. The near-field of an antenna is associated with what a close observer sees when looking at an antenna [Fig. 4.1(a)]. In this case, an observer views each point of the antenna aperture from a different angle, or in other words, rays emitted by the antenna encounter the observer under different angles depending on their departure location from the antenna aperture. In contrast, if an observer is at a distance extremely far away from an antenna, the separate rays, which would ultimately converge at infinity, appear to be parallel [Fig. 4.1(b)]. These parallel rays can also be seen by an observer at a short distance to the antenna when focusing them onto a single spot using a collimating optic like a lens [Fig. 4.1(c)] or a reflector. That is, a lens (or a reflector) can be used to bring the far-field of an AUT much closer, which is beneficial to measuring far-field characteristics of AUTs, as large distances are inconvenient and may cause issues regarding providing sufficiently high SNR in antenna measurements. Based on the above, the working principle of a conventional lens-type CATR is explained in the following, followed by that of the camera-type THz CATR. Figures 4.2(a) and (b) serve to support the following discussions.

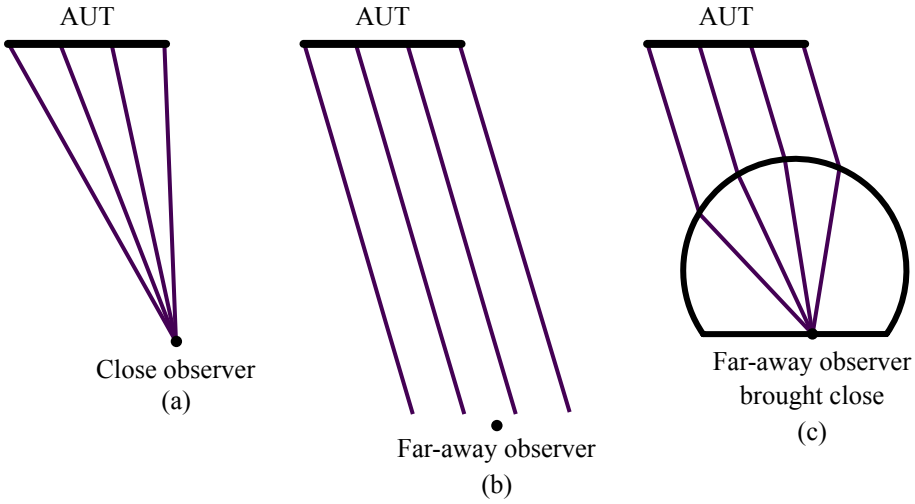

Figure 4.1. Near-field versus far-field. Radiation fields emanating from an AUT viewed by a close observer (a), a far-away observer (b), and an observer seeing the same as the far-away observer but at a short distance (c). This last case is achieved by employing a lens, which focuses parallel rays onto a focal spot. While (a) is accompanied with near-field characteristics of the AUT, the other two cases of (b) and (c) are accompanied with its far-field characteristics.

In a conventional CATR, an observer situates in the focal point of a lens, as illustrated in Fig. 4.2(a). Now, if rotating an AUT mechanically, its far-field radiation pattern can be determined at a compact, much shorter range compared to the far-field range. The same working principle can be applied to the camera-type THz CATR. Here, each camera pixel represents an observer, as illustrated in Fig. 4.2(b). The key difference compared to conventional devices is that several observers are present, namely the different camera pixels, with each pixel viewing the antenna under a different angle. Thus, when the AUT of a radiation source is placed near the camera lens, acquiring an image with the camera results in obtaining the far-field radiation pattern of the AUT through a single shot. The question of the minimum and maximum size of antennas to be measured is addressed next.

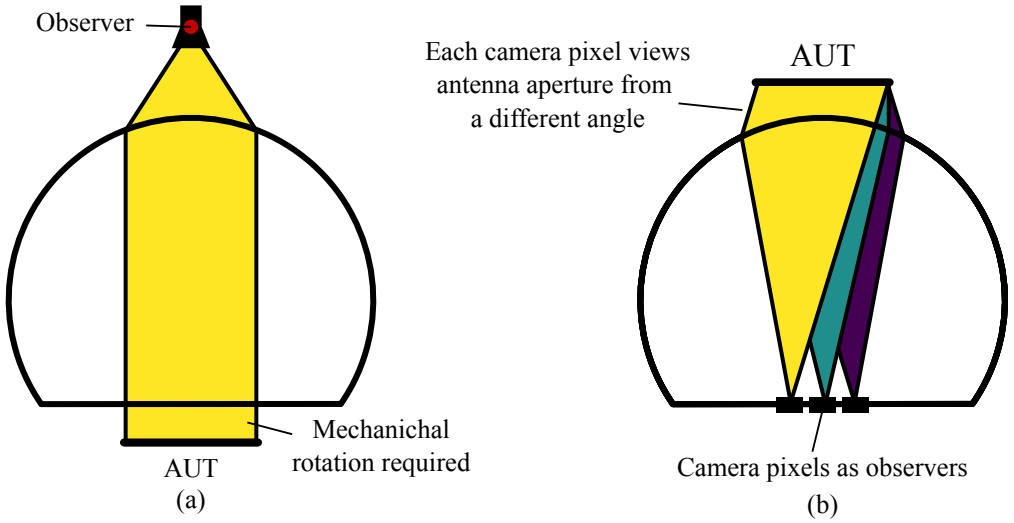

Figure 4.2. Camera-type CATR working principle. Illustrations of the working principle of a conventional CATR (a) and the proposed camera-type THz CATR (b). In a conventional CATR, an observer situates in the focal point of a lens, with mechanical rotation of the AUT allowing performing far-field measurements. In a camera-type CATR, each camera pixel represents an observer, viewing the AUT under different angles. Placing an AUT at a compact range allows inspecting an AUT for far-field characteristics—without the necessity for mechanical sampling.

4.3 AUT Size Limitations

An important aspect to be clarified in advance is the minimum and maximum AUT size suitable for measurements with the camera THz CATR. To clarify, the main job of this CATR is the determination of the far-field characteristics of an AUT, such as the radiation pattern, directivity, HPBW, and radiation power. The first parameter gives a qualitative picture of the radiation characteristics. In contrast, the last three provide a more meaningful quantitative picture, with directivity and HPBW being directly related. If either the directivity or the HPBW can be determined with high accuracy, so can the other related parameter. This point should be considered when estimating the AUT size limitations.

While small AUTs cause spillover losses, far-field conditions cannot be provided when AUTs are too large, as the camera pixels may not be able to cover the entire antenna aperture. Spillover losses essentially mean that only a tiny portion of the far-field radiation pattern can be determined. In other words, it may be the case that the main lobe can be captured since it falls just inside the camera FoV, while sidelobes do not. Since the HPBW of an AUT can be determined as long as the main lobe is captured, this should be considered when identifying the minimum AUT

size. Unlike in this case, in the case of a large AUT, most parts of the radiation pattern may fall within the camera FoV, including the main lobe, major sidelobes, and several minor sidelobes. This is because the larger an antenna, the narrower the beam it emits. Although this may sound great on the first view, there is a substantial drawback when characterizing too large AUTs. To clarify, far-field conditions are only provided at a compact range if the entire aperture of the AUT is watched by the observer, that is, by the camera pixels. To this end, ray-tracing calculations can be employed to identify the maximum AUT diameter for which all rays that are emanating from its antenna aperture land only on the portion of the chip area associated with the pixel that looks in the direction under scrutiny. This has to be studied for all camera pixels, which look into different directions, as we know.

As elaborated above, the lower limit relates to the 46° FoV of the camera. Thus, according to the HPBW criterion ($D_{\mathrm{Antenna}} = \lambda/46° \cdot 180/\pi$), the estimated minimum AUT diameter, D_{Antenna}, is 0.62–0.34 mm from 0.6–1.1 THz, where the camera is relatively sensitive to EM waves. Ray tracing was performed based on Snell's law of refraction using actual lens design parameters to study to which extent rays emanating from an AUT under different angles land on the respective camera pixels and thus estimate the maximum AUT size. Specifically, ray tracing was performed for the extended hemispherical silicon lens with a radius, R, of 7.5 mm, an extension length, L, of 2.75 mm, and a dielectric constant, $\epsilon_{r,Si}$, of 11.67[1]. Here, multiple rays emitted from an AUT—placed directly in front of the camera with a distance of 1 mm—were considered, for three angles of incidence, namely –23°, 0°, and +23°, to study two edge pixels and a fictive center pixel; fictive since there is no camera pixel situated in the lens center due to the even number of pixels and FPA centering to the lens center. Figure 4.3 shows the result. The maximum AUT diameter for which rays incident upon the camera lens always land just on a particular camera pixel, regardless of the angle of incidence, is 3.2 mm, as indicated in the figure. This number could be considered as the maximum AUT size. However, the question arises whether all camera pixels are always used in characterizing an AUT. Arguably, large AUTs may radiate their main lobes, major sidelobes, and minor sidelobes within a much smaller sector of the hemisphere than the camera FoV captures. Ray tracing calculations will show that angles within ±10° are uncritical for antennas with aperture diameters larger than 3.2 mm (up to ∼8 mm according to ray-tracing calculations). Therefore, instead of calling the 3.2 mm as maximum

[1] http://www.tydexoptics.com/products/thz_optics/thz_materials/

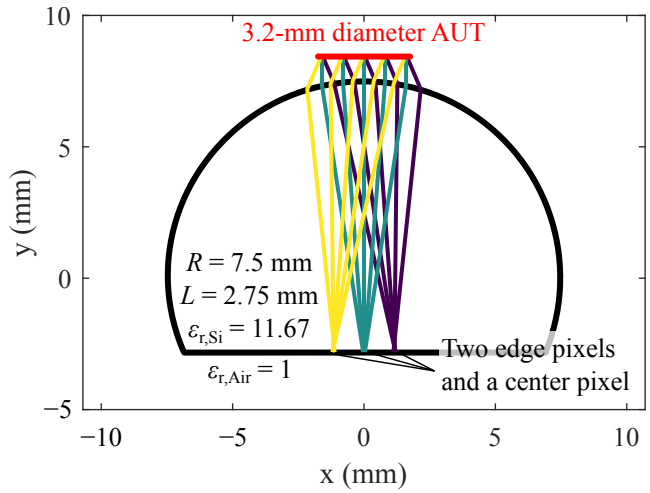

Figure 4.3. Result of ray-tracing calculations. Result of ray-tracing calculations for multiple rays emanating from an AUT with an aperture diameter of 3.2 mm under three different angles seen by edge pixels and a center pixel of the camera. All rays land in the area of the camera FPA occupied by a particular camera pixel and thus only excite the pixel that looks into the direction under scrutiny.

AUT size, the angular resolution of the camera is considered. According to the Nyquist criterion, the maximum AUT size limit refers to twice the camera angular resolution, which means half the camera lens diameter of 15 mm. In summary, the THz CATR allows determining far-field characteristics of radiation source antennas with a minimum AUT diameter of 0.62–0.34 mm from 0.6–1.1 THz and a maximum AUT diameter of 7.5 mm within this band.

4.4 Scan Loss Calibration

Off-axis displaced camera pixels experience aberrations, as we discussed in Sec. 2.5.2.1. Off-axis aberrations essentially mean deteriorated directivity for off-axis displaced pixels. Coupled with reflection losses at the lens surface, this is generally referred to as scan loss, causing an unequal weighting of the main lobe and the sidelobes. This unequal weighting introduces a systematic error in determining the far-field radiation pattern of an AUT and thus all its far-field characteristics. Scan loss must be determined for all camera pixels to calibrate this systematic error, whereby off-axis aberrations make it frequency-dependent. Thus, calibration of scan loss would result in enormous efforts because of the frequency dependence of the directivity and associated deterioration with respect to off-axis displacement. Although directivity is a frequency-dependent parameter, it can be assumed that the relative deterioration of directivity with off-axis displacement remains more or less constant with respect to

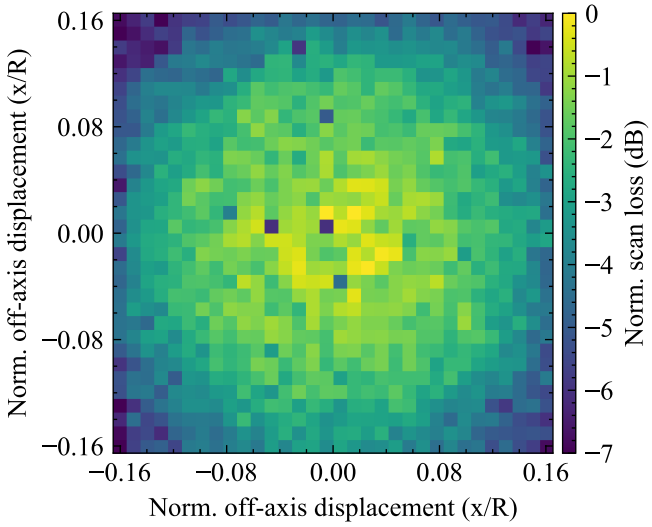

Figure 4.4. Measured scan loss. Scan loss as a 2-D function of the normalized off-axis displacement in both dimensions of the FPA. This result is obtained from single-pixel far-field radiation pattern measurements performed at 0.652 THz. Quantitatively, this result holds only for this specific case in terms of frequency and silicon lens (32.6-λ in diameter). Qualitatively, it will hold for any camera regardless of the FPA used, lens diameter, and frequency, provided that the center pixel is placed in the elliptical focus.

frequency. Therefore, a calibration performed at one frequency could help calibrate for scan loss. It is remembered that a complete single-pixel far-field radiation pattern characterization was performed in the context of Section 2.5 to determine off-axis aberrations in the form of HPBW and directivity variation across the entire FPA at 0.652 THz. Normalized scan loss was obtained from the same measured data, and the result is shown in Fig. 4.4. Normalized scan loss was determined as the power integrated within the HPBW of a single-pixel far-field radiation pattern relative to the maximum power of the complete radiation pattern scan. Based on the explanation above, the scan loss data presented can be used for calibration purposes to account for unequally weighted main lobes to sidelobes due to off-axis aberrations and pixel-to-pixel variation.

In principle, the concept of the THz CATR is not tied to using a camera. Instead, a single camera pixel or any other lens-integrated antenna-coupled THz detector could be employed. Scan loss would then be a non-issue. However, the necessity of mechanical scanning would be detrimental to the measurement time required to produce a far-field radiation pattern, which is the main advantage of the herein presented camera-type THz CATR. Also, lens-coupled sources or source arrays of THz radiation may be employed to characterize an AUT of a receiver, according

to the principle of reciprocity [168]. The scanning issue still applies to single sources, whereas source arrays are somewhat comparable to cameras. However, there are two fundamental issues with source arrays. The first issue refers to the bandwidth. Usually, high-power source arrays are narrowband. The second issue is the number of pixels due to source pixel cells being large relative to a wavelength. This issue brings another related one in terms of angular resolution. Super-resolution imaging could help improve this aspect. However, compared to employing a camera, much more scanning would be required.

4.5 THz CATR Testing

In this section, the THz CATR is investigated for its capabilities in determining far-field radiation pattern characteristics. First, the details regarding the experiment are given. Second, details for the data post-processing required to produce far-field radiation patterns from low- and super-resolution images are given. Third, reference measurements performed at a conventional far-field range and full-wave simulations are detailed. Fourth and last, the measured results are provided, focusing on the determination capabilities of the THz CATR concerning directivity, HPBW, and radiation power. The quality in determining these parameters is assessed by relating measurements performed at a compact range to reference measurements. Specifically, directivity and HPBW are related to reference measurements performed at a conventional far-field range, whereas radiation power values are related to reference measurements performed in the near-field using an absolute power meter, which is common practice.

4.5.1 Experiment

In order to test the THz CATR for its capabilities in determining far-field radiation pattern characteristics, a suitable radiation source is required. This source must match the camera in terms of radiation frequency and radiation power. In addition, the size of the antenna through which the source routes the THz signal into free space must be within the minimum and maximum AUT size previously determined. To this end, the $\times 54$ multiplier chain-based µW-level radiation source equipped with a 1.96×1.96-mm^2 diagonal horn antenna represents the most suitable candidate available. It generates a THz signal from 0.6–1.1 THz and radiates this with a directivity on the order

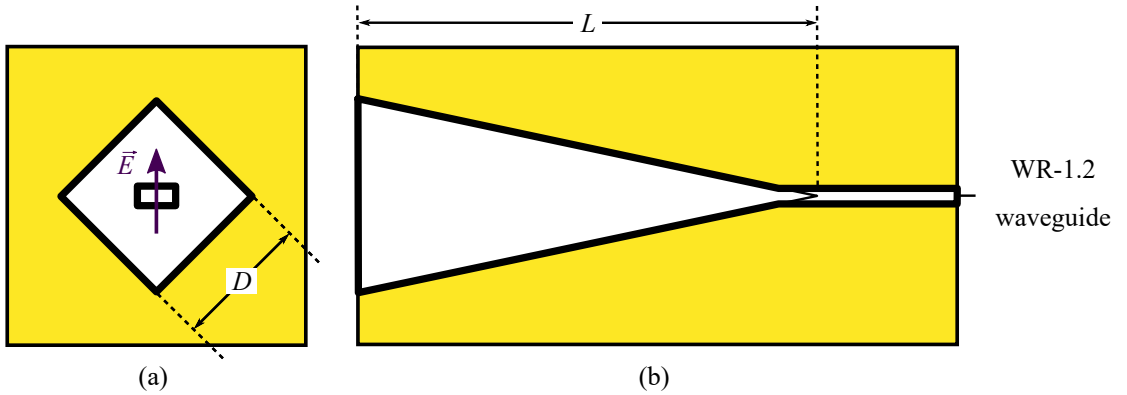

Figure 4.5. Tested diagonal horn antenna. Illustration of the tested diagonal horn antenna, with (a) top view and (b) sectional view.

of 23.7–28.2 dBi. Figures 4.5(a) and (b) illustrate top view and sectional view of the diagonal horn antenna, respectively. The antenna is linearly-polarized, with the E-field oriented along a diagonal of the antenna, as indicated in this figure. As further indicated in this figure, a WR-1.2 waveguide feeds the antenna.

During the measurements, the radiation source was fixed in place nearby the camera lens, as indicated in Fig. 4.3. More specifically, it almost touched the camera lens. Such a close configuration minimizes spillover losses. Unlike the radiation source, the camera was not fixed. Instead, it was mounted onto a six-axis table-top robot arm in order to facilitate a rotational raster scan. Recall that angularly offset low-resolution images are required to produce a super-resolution image. THz absorbers were placed wherever possible, wrapped around both the AUT and the camera lens. These absorbers are crucial in minimizing the effect of stray radiation scattered or reflected by metal objects in the surrounding.

In terms of the measurement procedure, 4×4 low-resolution images were acquired within a 2-D polar raster-scanning around the camera lens center. The angular range of rotational scanning was 1.66°, which corresponds to the beam separation angle between adjacent camera pixels. Thus, the lateral angular step size was 0.415°. At each position of this rotational raster scan, the source radiation frequency was swept from 0.6–1.1 THz at average intervals of 33 GHz. Accordingly, in data post-processing, 15 low- and super-resolution far-field radiation patterns were produced each. Drizzling to produce the super-resolution far-field radiation patterns was performed using Eqn. (2.13). At the selected frequencies, the source radiates a THz signal >1.5 µW. Peak radiation power of 8.8 µW occurs at 0.852 THz.

The camera readout was averaged over 1024 frames to improve the NEP of the camera at this frequency to $\sim\frac{22}{\sqrt{1024}}$ nW = 687.5 pW, according to [own4]. With this, the entire measurement lasted 136 min. Hence, each super-resolution far-field radiation pattern effectively took 8.5 min, while their low-resolution counterparts effectively took 30 seconds. Improved NEP aimed to realize a PSNR greater than 30 dB, which can be calculated as

$$\mathrm{PSNR} = 10 \cdot \log_{10}\left(\frac{P_{\mathrm{Pix,max}}}{\sigma}\right), \tag{4.1}$$

where σ denotes the RMS image noise, and $P_{\mathrm{Pix,max}}$ is the maximum power incident on a camera pixel. In far-field radiation pattern measurements, the PSNR determines whether or not sidelobe detection is possible, therefore being of great importance to overall measurement accuracy. Typically, a PSNR of 30 dB is sufficient to sense major and minor sidelobes of an AUT [169]. The maximum achieved PSNR is 34.8 dB, realized at a radiation frequency of 0.852 THz.

4.5.2 Data Post-Processing

From low- and super-resolution images, the far-field radiation patterns were determined as follows. First, each low-resolution image was calibrated for scan loss using the calibration matrix shown in Fig. 4.4 to remove the effect of the differences in directivity and responsivity among the pixels. For this calibration, each low-resolution far-field radiation pattern was divided by the corresponding linearly-scaled calibration matrix. More specifically, only those camera pixels that detected a THz signal were scaled using a global 0-dB SNR threshold so as not to increase noise values artificially. Second, spatial standing wave effects were removed by filtering them out after [170]. To this end, the image domain was transformed into the frequency domain utilizing fast Fourier transformation (FFT). Here, standing waves were filtered out by applying a low-pass filter, and the inverse FFT was then used to generate the low-pass filtered image. Third and last, the corresponding far-field radiation patterns were calculated from calibrated low- and super-resolution images. To this end, the directivity, D_{dBi}, was according to [169], calculated as the ratio of power per angular position divided by the sum of overall

power, normalized to the beam separation angle, ϕ:

$$D_{dBi} = 10 \cdot \log_{10} \left(\frac{4\pi \cdot P_{\text{Pix}}}{\left(\frac{\pi}{180} \cdot \phi\right)^2 \cdot \text{sum } P_{\text{Pix}}} \right), \tag{4.2}$$

where P_{Pix} is the power incident on a camera pixel. For low-resolution imaging, the beam separation angle was set to the calculated beam separation angle between two adjacent camera pixels, with $\phi = 1.66°$ [Eqn. (2.5)]. For the super-resolution imaging, it was set to the step size of the rotational raster-scanning, with $\phi = 0.415°$. As such, the directivity for all angular positions is determined, whereas the maximum yields peak directivity. It is noted the limited camera FoV does not allow to cover the entire hemisphere. For this reason, the directivity calculation neither includes all minor sidelobes nor the back lobe. Nevertheless, the main lobe, major sidelobes, and the first minor sidelobes may be covered, yielding accurate results in calculating directivity values, at least for radiation sources with decent directivity.

4.5.3 Reference Measurements and Full-Wave Simulations

To adequately assess the measured results obtained from THz CATR measurements, reference measurements performed at a far-field range were employed as well as full-wave simulations performed in HFSS from ANSYS. Reference measurements and full-wave simulations were set up as follows.

For reference measurements, the radiation source and the camera were placed at a conventional far-field range using a similar setup as shown earlier in the context of Chap. 2 [Fig. 2.14]. Specifically, the distance was 20 cm. This distance is much larger than the most significant far-field distance associated with the highest radiation frequency investigated of 1.08 THz. At this frequency, the distance of 20 cm exceeds the Fraunhofer distance of $2 \cdot D^2/\lambda = 2.88$ cm for the antenna aperture diameter of 1.96 mm. In contrast to the THz CATR measurements, only a single camera pixel was employed, while the camera was scanned around the AUT. More specifically, the camera was scanned over a $\pm 23° \times \pm 23°$-sector of the hemisphere corresponding to the camera FoV, with a 1° lateral step size. With a required time integration of 1.75 seconds to achieve sufficiently high SNR in reference measurements, it took about 1 hour to obtain a far-field radiation pattern for just a single frequency. Compared to the measurement time required in THz CATR measurements, this is substantially

longer. Quantitatively, the reference measurements performed at a conventional far-field range took about 7 times and 120 times longer than those performed at a compact range using low- and super-resolution imaging, respectively.

Regarding full-wave simulations performed in HFSS, a three-dimensional (3-D) replica of the AUT [Fig. 4.5] was built considering the antenna aperture of 1.96 × 1.96 mm^2 and the horn length of 20 mm. The EM signal was provided using a WR-1.2 waveguide feed, as implemented.

4.5.4 Measured Results and Discussions

In this section, the measured results are presented and carefully compared to reference measurements. This presentation starts with qualitative observations based on 2-D far-field radiation patterns produced by low- and super-resolution imaging and associated D-plane cuts. Given this qualitative analysis, the measurement time required for sidelobe detection is also considered. After that, a quantitative analysis is conducted concerning the directivity and HPBW determination capabilities of the THz CATR. In this context, the impact of the limited camera FoV on the directivity calculation is also considered. Then, the quantitative analysis is continued regarding the radiation power determination capabilities of the THz CATR. Finally, this section closes with a summary of the THz CATR performance.

4.5.4.1 2-D Far-Field Radiation Patterns

Figure 4.6(a) and (b) show the low- and the super-resolution far-field radiation pattern obtained from THz CATR measurements performed at 0.852 THz, as an example. This frequency is selected as an example because of the highest PSNR of 34.8 dB achieved. From inspection of these figures, it can be observed that the far-field radiation pattern obtained by super-resolution imaging features more spatial details of the far-field radiation pattern, which is due to an increased number of pixels coupled with enhanced angular resolution. While the low-resolution far-field radiation pattern has 32 × 32 pixels, the super-resolution far-field radiation pattern has 128 × 128. The far-field radiation pattern represents one low-resolution image, and the super-resolution one is the combination of 4 × 4 low-resolution images.

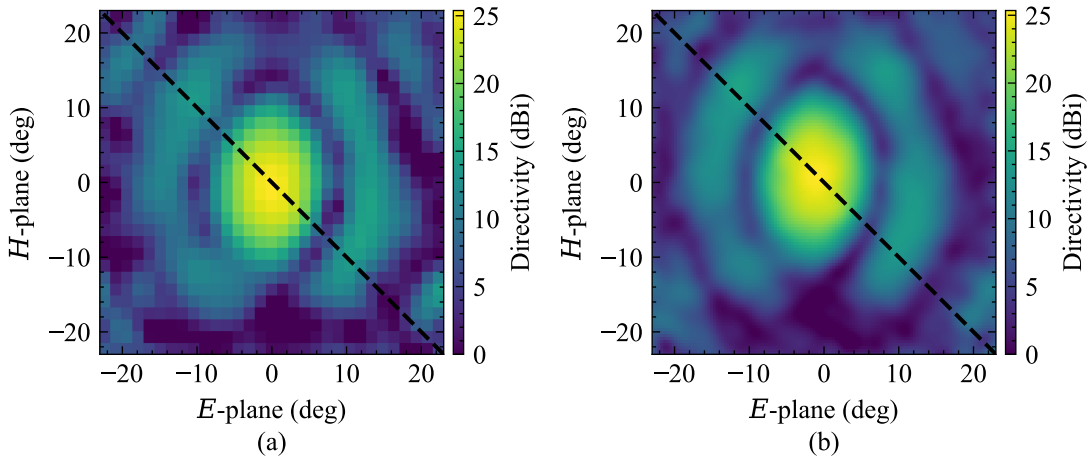

Figure 4.6. Measured low- and super-resolution far-field radiation patterns. Low-resolution (a) and super-resolution (b) far-field radiation patterns of the tested AUT measured at 0.852 THz, showing the highest PSNR of 34.8 dB. It can be observed that the super-resolution image shows more spatial details of the far-field radiation pattern. After [own9] © 2021 IEEE.

4.5.4.2 D-Plane Cuts

Figure 4.7 shows normalized D-plane cuts, i.e., cross-section cuts along the diagonals of the far-field radiation patterns, obtained from THz CATR measurements in comparison to reference measurements performed at a conventional far-field and full-wave simulations performed in HFSS; because of better measurement accuracy, super-resolution data is used. The D-plane is chosen for two reasons: the characteristic sidelobes of the tested diagonal horn antenna lie in this plane, and the angular FoV covered is largest. From inspection of Fig. 4.7, it is clear that THz CATR measurements work reasonably well. The fairest comparison is made to reference measurements performed at a conventional far-field range. In this regard, it can be qualitatively judged that THz CATR reproduces main lobes well. On the other hand, sidelobe determination does not work similarly well for all frequencies. For some, the major side lobe is rendered well, but for others, it is not. At 0.929 THz, for example, the main lobe and major sidelobes almost match perfectly. The subsequent radiation frequency at 0.960 THz represents one example where the major sidelobes are overestimated by a few dB, while the main lobe agrees with reference measurements. Also, sidelobe detection was not possible in all THz CATR measurements, which is attributed to insufficient PSNR.

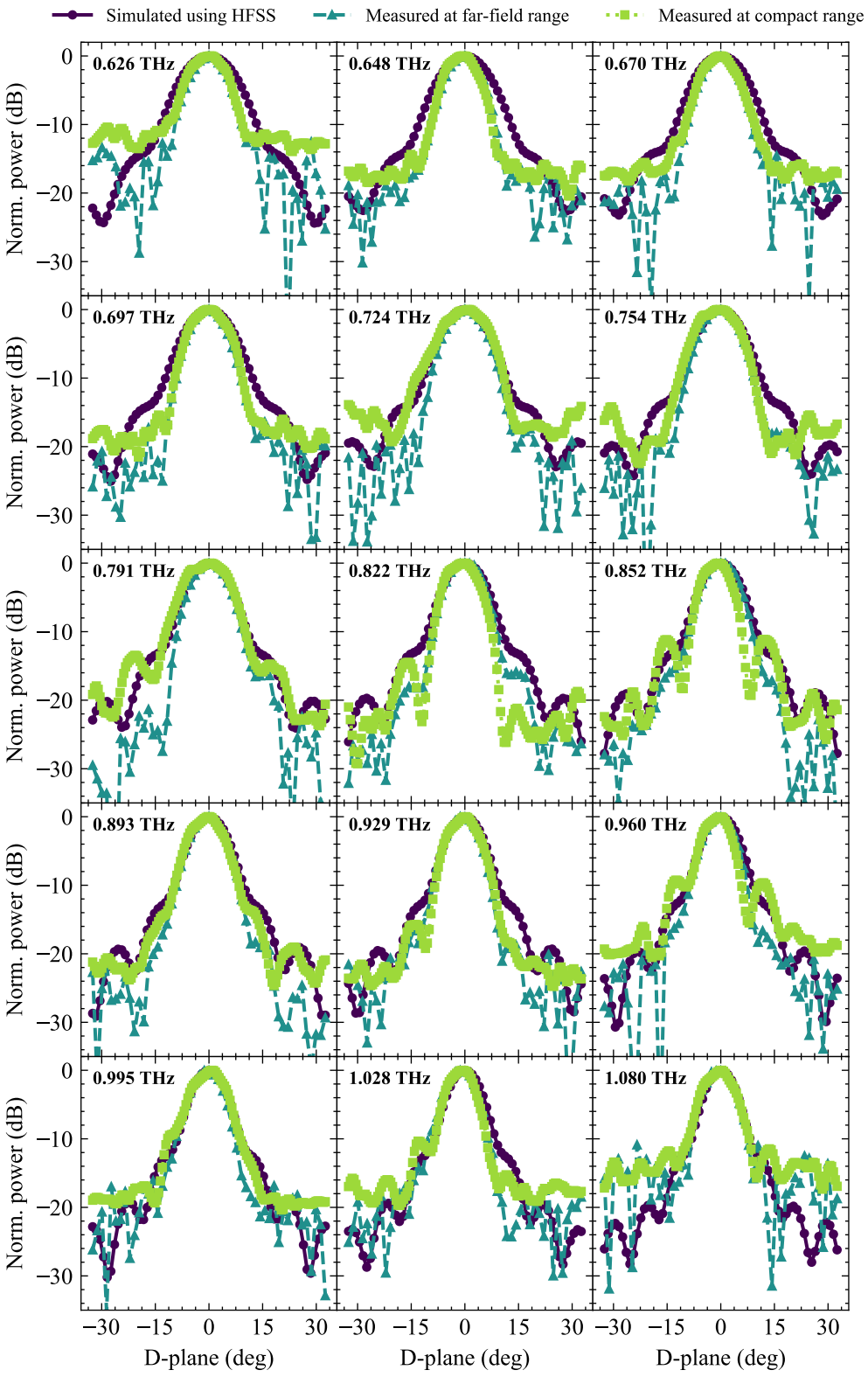

Figure 4.7. Far-field radiation pattern D-plane cuts. Normalized D-plane cross-section cuts extracted from far-field radiation patterns measured at a compact range by super-resolution imaging using the THz CATR in comparison to simulations and reference measurements. Corresponding frequencies are indicated in the upper left of the subplots. Subplots share both x- and y-axes. After [own9] © 2021 IEEE.

4.5.4.3 Evaluation of Directivity and HPBW Determination

The preceding discussions on the ability of the THz CATR to determine far-field characteristics have been qualitative, comparing associated far-field radiation pattern measurements with reference measurements performed at a conventional far-field range. It has already been confirmed that the THz CATR can determine the far-field characteristics of an AUT of a radiation source. However, the question arises of how good this works. To this end, a quantitative analysis is required. Specifically, directivity and HPBW observed from THz CATR measurements must be related to those observed from reference measurements and full-wave simulations. The fairer comparison is made to reference measurements. The directivity and HPBW obtained from THz CATR measurements by low- and super-resolution evaluated as a function of the frequency are plotted together with the respective values obtained from reference measurements and full-wave simulations in Fig. 4.8(a) and (b), respectively. From inspection of these figures, it is clear that the overall trend in directivity and HPBW variation with respect to frequency obtained from reference measurements is reflected THz CATR measurements, namely trending upward for directivity and trending downward for HPBW. These trends are also observed when inspecting simulated directivity and HPBW values. This is, again, just a qualitative observation. The quantitative picture of the directivity and HPBW determination capabilities of the THz CATR can only be given by the RMS accuracy in determining such parameters concerning values obtained from reference measurements. The directivity extracted from super-resolution far-field radiation patterns is determined within an RMS accuracy of 0.85 dB based on reference values measured at a conventional far-field range. For low-resolution imaging, the RMS directivity determination accuracy achieved is 2 dB. The RMS accuracy achieved from HPBW values related to reference measurements is 1.23° using low-resolution imaging and 1.16° using super-resolution imaging. These values can be considered quantitative because they include a wide range of frequencies (0.6–1 THz) and thus different levels in HPBW and PSNR. This analysis clearly shows that super-resolution imaging should be preferred over low-resolution imaging for the most accurate measurements.

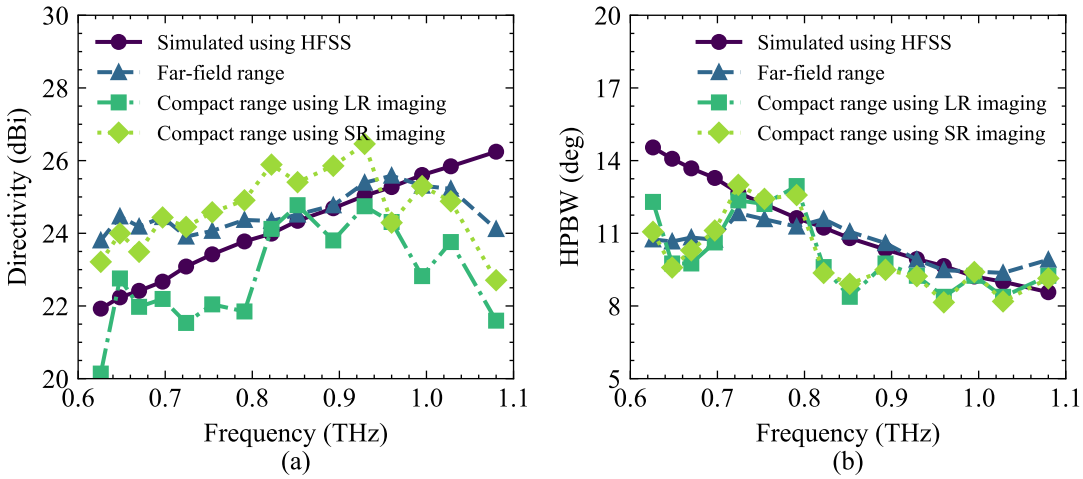

Figure 4.8. **Evaluation of the directivity and HPBW determination capabilities.** (a) Frequency-dependent directivity extracted from measured far-field radiation patterns using both low- and super-resolution imaging compared to values determined by calculations, simulations, and reference measurements performed at a conventional far-field range. (b) Frequency-dependent average HPBW extracted from low- and super-resolution imaging-based THz CATR measurements compared to values obtained from calculations, simulations, and aforementioned reference measurements. After [own9] © 2021 IEEE.

4.5.4.4 Impact of Limited FoV on Directivity Determination

The THz CATR exhibits a limited FoV. The question arises of how this impacts the determination of far-field characteristics, such as directivity, HPBW, and radiation power. While the last two parameters can be determined with sufficient accuracy as long as the available FoV captures the HPBW of the AUT, a minimum FoV may be required to determine the first parameter, namely the directivity, with sufficient accuracy. This gains importance when small AUTs are concerned. To clarify, small AUTs radiate broad beams, for which reason sidelobes cannot be sensed through the THz CATR, lowering the directivity determination accuracy. As for the first two parameters, the ratio of available FoV to HPBW of the AUT matters. This ratio increases with respect to increasing AUT size. Therefore, directivity determination is expected to be less accurate when characterizing small AUTs. In order to provide a quantitative picture, the directivity was evaluated as a function of the FoV-to-HPBW ratio and the associated achievable directivity determination accuracy. With this, the influence of the available FoV on the directivity calculation could be investigated. This investigation is crucial in verifying the minimum AUT size given earlier [Sec. 4.3].

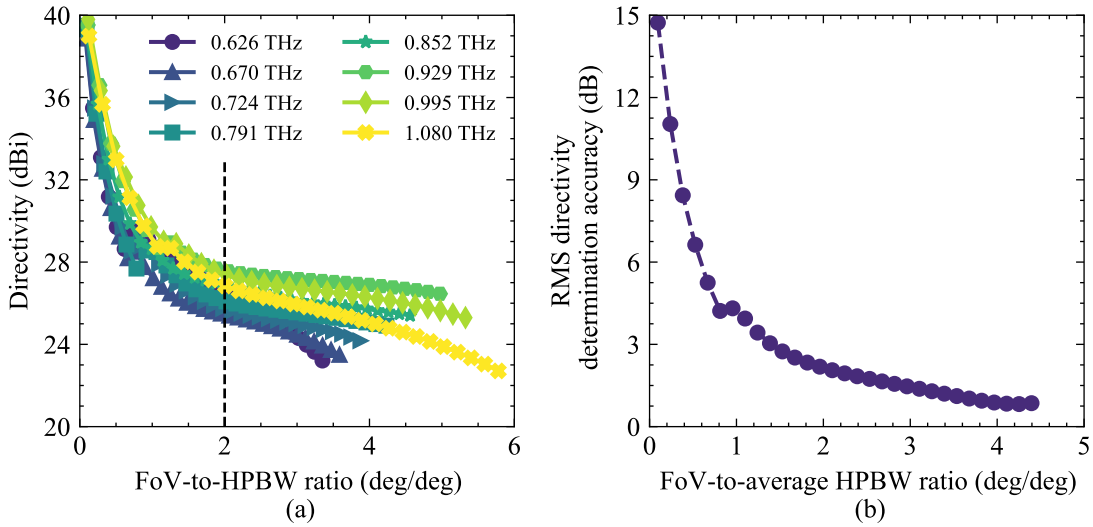

Figure 4.9. Influence of FoV on directivity determination accuracy. (a) Directivity evaluated as a function of the FoV-to-HPBW ratio for a selection of frequencies. (b) Directivity determination accuracy versus FoV-to-average HPBW ratio under consideration of all 15 frequencies investigated from 0.6–1.1 THz. In both (a) and (b), ideal HPBW values were used to relate the FoV to HPBW. After [own9] © 2021 IEEE.

The procedure for analyzing the limited FoV on the directivity determination applied is as follows. The FoV was reduced stepwise in the data post-processing, applying the directivity calculation explained earlier at each step; this analysis refers to super-resolution imaging because of the higher measurement accuracy. This calculation was performed for each frequency of investigation. Finally, the FoV was normalized to the HPBW of the associated frequency of the AUT tested here. Ideal HPBW values were used. This process should provide a comprehensive picture of the impact of the available FoV on the directivity calculation. In simpler terms, one can calculate the FoV-to-HPBW ratio based on the camera FoV and the ideal HPBW of a given AUT and know whether the THz CATR is an appropriate candidate to characterize an AUT of interest or not. The associated RMS directivity determination accuracy was calculated based on that. In this regard, an average HPBW was considered using values ranging from the lowest (0.626 THz) to the highest (1.080 THz) radiation frequency tested here.

Figure 4.9(a) shows the directivity as a function of the FoV-to-HPBW ratio. It is noted that only each second frequency out of all investigated frequencies is plotted in this figure not to clutter it. From inspection of this figure, it is clear that the directivity starts saturating for most frequencies above an FoV-to-HPBW ratio of about two. Consequently, this ratio should be considered as the minimum to

obtain reasonably accurate results regarding directivity determination. To support this qualitative observation with a quantitative one, Fig. 4.9(b) shows the RMS directivity determination accuracy as a function of the FoV-to-average HPBW ratio. The RMS directivity determination accuracy saturates to a minimum value of 0.85 dB. Therefore, the minimum AUT size for which an accurate direct determination of the directivity can be ensured is 1.24–0.68 mm from 0.6–1.1 THz considering that an FoV-to-average HPBW of at least two should be given. Nevertheless, as we know, directivity can also be determined via the HPBW, and hence smaller FoV-to-HPBW ratios are applicable as well. For a minimum ratio of one required to capture the HPBW of the source beam, the minimum inspectable AUT size scales down to 0.62–0.34 mm from 0.6–1.1 THz.

4.5.4.5 Evaluation of Radiation Power Determination Capabilities

The THz CATR allows determining the radiation power of a source by simply inspecting far-field radiation patterns. This can be done by calculating the frequency-dependent radiation power of a source, $P_{\mathrm{Rad,TX}}$, via the frequency-dependent voltage responsivity of the camera[2], R_{v}, as

$$P_{\mathrm{rad,TX}} = \frac{\sum_{pix=1}^{1024} V_{\mathrm{Pix}}}{R_{\mathrm{v}}}, \tag{4.3}$$

where V_{Pix} denotes the voltage response of a camera pixel. By this, the radiation power of the herein tested source was determined for each low-resolution image. Thus, 16 values per frequency point were determined, out of which average and RMS values were calculated. These values are plotted along with values obtained from reference measurements performed with an absolute power meter (PM4) in Fig. 4.10. To this end, the voltage responsivity, R_v, of the camera, as conducted in [own4], was used. To also provide a quantitative picture of the radiation power determination capabilities of the THz CATR, the RMS error in determining radiation power was calculated concerning values observed from reference measurements by considering the average values. Here, the RMS accuracy achieved is 0.7 µW. On another note, the σ-fluctuation around the average values is within 1 dB for all frequencies except the first one. Two statements result from this fact. First, the THz CATR allows for the radiation power characterization of sources if their far-field radiation pattern

[2]The responsivity is defined as the output voltage signal of the detector at a given incident radiation power and thus gives a ratio of voltage and power.

falls within the FoV of the camera. Second, this analysis shows that the effect of spatial standing waves for THz CATR application is negligible.

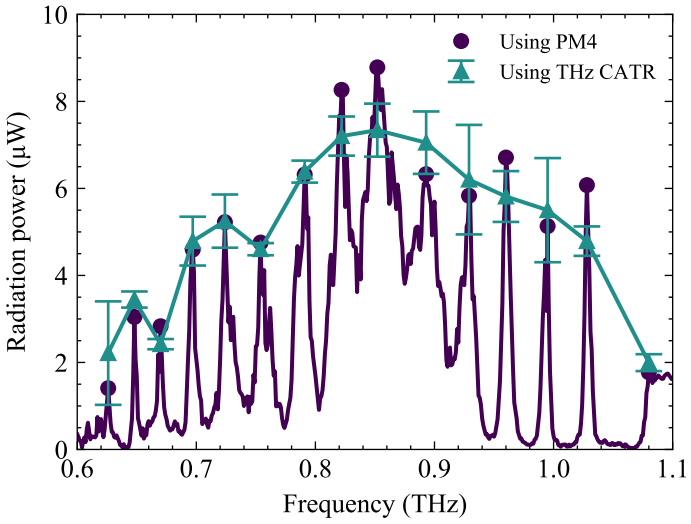

Figure 4.10. Evaluation of the radiation power determination capabilities. Radiation power as a function of the frequency measured using the THz CATR in comparison to reference measurements using a PM4—a commonly used absolute power meter. After [own9] © 2021 IEEE.

4.5.4.6 Performance Summary

Table 4.1 summarizes the THz CATR performance in terms of operating bandwidth, the minimum and maximum AUT sizes inspectable within that bandwidth, and the associated RMS accuracies in determining directivity, HPBW, and radiated power. Moreover, the estimated measurement time required to achieve sufficiently high PSNR to detect major and minor sidelobes is given.

4.6 Design of New THz CATRs

In general, CATRs are subject to several problems [158]. However, in addition to these already discussed problem areas, the camera-type THz CATR presented here deals with further problems. The experience gained through this work makes it possible now to derive problem areas that must be considered when designing and fabricating (improved) devices. To derive these problem areas, three camera-related aspects, such as FoV limitations, angular resolution limits, and scan loss, are described in the following.

Table 4.1. THz CATR performance summary. A summary of the THz CATR performance in terms of operating bandwidth, minimum and maximum AUT size, RMS accuracy in determining directivity, HPBW, and radiation power, and the measurement time required to make accurate sidelobe detection possible. It is noted that RMS accuracies in determining directivity, HPBW, and radiation power relate to the radiation source tested here. These accuracies may vary when characterizing AUTs with smaller or larger diameters. After [own9] © 2021 IEEE.

Applicability	Mobile far-field characterization of THz sources
Operating bandwidth	0.6–1.1 THz
Minimum AUT size	0.62–0.34 mm from 0.6–1.1 THz
Maximum AUT size	7.5 mm from 0.6–1.1 THz
RMS directivity determination accuracy	2 dB/0.85 dB using low-/super-resolution imaging
RMS HPBW determination accuracy	1.23°/1.16° using low-/super-resolution imaging
RMS radiation power determination accuracy	0.7 µW using low-resolution imaging
Estimated measurement time	<10 min/30 min for PSNR >30 dB for 10-µW/5-µW radiation source

Limited FoV: The limited FoV restricts the camera-type THz CATR to radiation sources with a minimum directivity of 11.9 dBi. Essentially, the HPBW of an AUT can be determined as long as it is equal to or smaller than the camera FoV. Consequently, the THz CATR is in its current form limited to AUTs with a minimum diameter ranging between 0.62–0.34 mm from 0.6–1.1 THz.

Angular resolution: The limited angular resolution of the camera given by its extended hemispherical silicon lens restricts the camera-type THz CATR to AUTs with a directivity ranging from 33.5–38.7 dBi from 0.6–1.1 THz. In other words, the THz CATR is in its current form limited to AUTs with a maximum diameter of 7.5 mm, regardless of the frequency of interest.

Scan loss: Off-axis displaced camera pixels experience scan loss, which combines directivity variation and pixel-to-pixel variation among the pixels. Corner camera pixels, for instance, show a scan loss of almost 7 dB [Fig. 4.4]. This causes the main lobes and sidelobes of an AUT to be weighted unequally. This unequal weighting causes a systematic error in determining directivity.

While scan loss is a problem that can be prevented by calibration, as performed here, there remain problem areas related to minimum and maximum AUT size that the THz CATR can inspect. The minimum AUT size refers to the camera FoV. In order to overcome FoV limitations, measuring parts of the far-field radiation pattern defines a viable solution. However, this increases the measurement time quadratically. Other options are to either use a larger FPA or employ a smaller lens. The former accompanies higher fabrication costs, whereas the latter accompanies additional problems concerning spillover losses and alignment issues. Both options have the problem of increased scan loss, which can be calibrated but is highly undesirable as it reduces the SNR. An additional problem of using a smaller lens is that this further limits the maximum AUT size inspectable due to deteriorated angular resolution. While a larger lens helps improve this aspect, this is detrimental to the minimum AUT size inspectable. Optimally, lens size and FPA size are increased simultaneously, with the latter increased due to a higher number of pixels. This combination goes hand in hand with a larger FoV and better maximum achievable angular resolution. In this case, however, the number of low-resolution images required to achieve optimal sampling may increase. This aspect may be mitigated by reducing the pixel pitch.

4.7 Chapter Conclusion

In this chapter, the application concept of the camera-type THz CATR has been presented. This concept states that a THz camera can be used to determine far-field characteristics of a THz radiation source at a compact range, including the radiation pattern, directivity, HPBW, and radiation power. For concept validation, a CMOS camera was operated as THz CATR to determine the far-field radiation characteristics of a ×54 multiplier chain-based µW-level 0.6–1.1 THz radiation source equipped with a 23.7–28.2 dBi standard gain horn antenna at a compact range. Far-field radiation patterns measured at a compact range through the CMOS camera have been compared to full-wave simulations and reference measurements performed at a conventional far-field range. This way, the far-field characteristics determination capabilities could be investigated.

The experimental results confirm that such devices allow determining far-field characteristics of THz radiation sources. However, because of limitations in terms of FoV and angular resolution, the minimum and maximum AUT size inspectable are limited. The minimum AUT size relates to the camera FoV, whereas the

maximum AUT size relates to the angular resolution of the camera. In numbers, minimum and maximum AUT sizes are 0.62–0.34 mm and 7.5 mm from 0.6–1.1 THz. A smaller camera lens would allow analyzing smaller antennas of lower directivity, limiting the maximum AUT size beyond the current state. The opposite applies to employing a larger camera lens.

Concerning the system limitations mentioned above, the benefit of super- over low-resolution imaging has been analyzed. The following has been found. Because of enhanced angular resolution, increased pixel count, and improved PSNR, super-resolution imaging outperforms low-resolution imaging in directivity and HPBW determination accuracy. With the help of super-resolution imaging, the directivity was determined within an RMS accuracy of 0.85 dB related to reference measurements performed at a conventional far-field range, whereas the HPBW was determined within an RMS accuracy of 1.16° from 0.6–1.1 THz. These numbers diminish to 2 dB and 1.23° when using low-resolution imaging. The source radiation power was determined within an RMS accuracy of 0.7 µW related to reference measurements performed with an absolute power meter. Although the performance in determining far-field characteristics suffers using low-resolution imaging, measurements performed in only a few seconds through single-shot measurements are especially valuable for initial radiation source testing.

In combination with the application concept of THz dispersive spectroscopy, as presented in Chap. 3, a CMOS camera now is capable of characterizing all far-field characteristics of THz sources, such as far-field radiation pattern, directivity, HPBW, radiation power, and harmonic content, while super-resolution imaging, as discussed in Chap. 2, helps improve the accuracy in determining these parameters. The first four parameters are ascribed to the CATR operation, whereas the last two parameters are ascribed to the spectroscope operation.

Chapter 5

THz Diffuse, Uniform Illumination Source

5.1 Chapter Introduction

Powerful illumination sources with uniform beam profiles operating at high frequencies are a much-needed but missing element in THz active imaging. Such components are required in camera-based applications to produce high-quality images with a high, homogeneously distributed SNR and a high spatial resolution. To clarify, a beam profile with uniform amplitude is desired so that an imaging target is homogeneously illuminated, resulting in a constant dynamic range across the entire imaging plane. As alluded to in the introductory discussions in Sec. 1.3.1, incoherent silicon integrated THz source arrays are pleasing candidates for practical active imaging applications due to their high scalability and the associated ability to generate large amounts of radiation power. However, in contrast to the aim of providing a uniform beam profile, contemporary incoherent THz source arrays produce several directional, non-overlapping beams [19], [20], as illustrated in Fig. 5.1(a), which will result in the undersampling of an object in THz active imaging. The reason for this is twofold: the footprint of the source pixels of such devices is large relative to a wavelength, and the source pixel pitch on-chip translates into a beam separation angle in free space. With regard to the design considerations derived from the previous investigations on incoherent silicon integrated THz cameras using an extended hemispherical silicon lens [Eqn. (2.12)], overlapping beams can be achieved with a lens-coupled THz source array of incoherent operation only if the pixel cells are

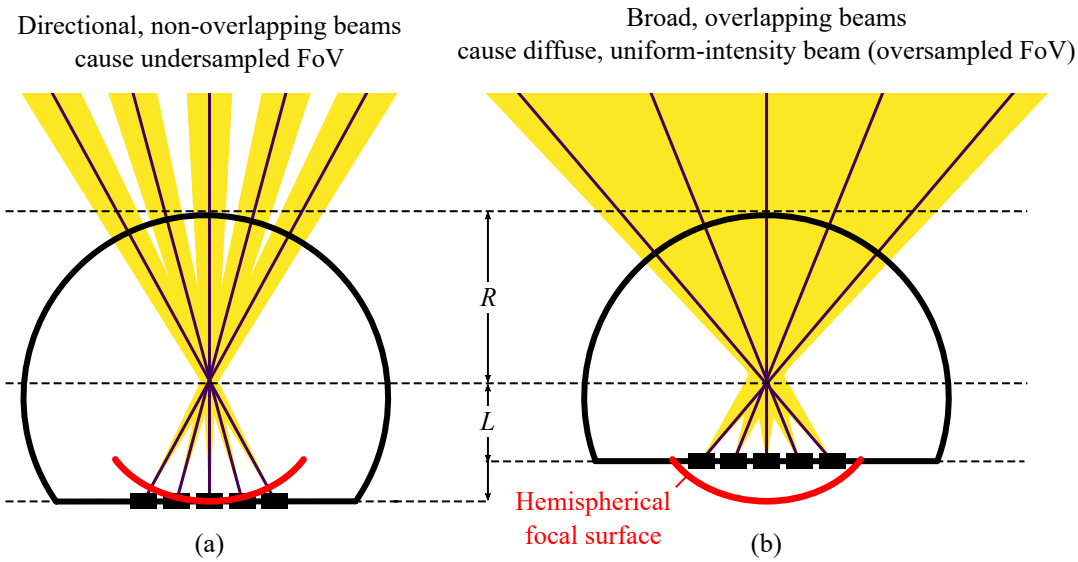

Figure 5.1. Problem statement and solution taken. Illustration of the primary motivation of this study, showing (a) how previous high-power THz incoherent source arrays [19], [20] produce directional, non-overlapping beams that lead to FoV undersampling, and (b) the primary objective of this study; a diffuse, uniform-intensity, high-power THz illumination source. Briefly, the reduction in lens extension length, L, relative to lens radius R, defocuses source pixels, which consequently overlap and combined in the far-field. It is noted that this figure is different from Fig. 2.1 in a way that the same frequency is concerned here.

small enough to be close to each other. However, the size of the source pixels cannot be easily reduced because they require a power generation network that contributes significantly to the overall footprint. Therefore, another solution is required to increase the overlap of the beams using an optimized silicon lens in order to produce a diffuse, incoherently-combined, uniform-intensity beam of THz radiation, as shown in Fig. 5.1(b). Briefly, the solution adopted here is to tailor the lens dimensions by reducing the lens extension length, L, relative to the lens radius, R, thereby defocusing the source pixels. Defocusing means broad source pixel beams, which may ultimately overlap and combine in the far-field.

Considerable research efforts have been made in the past to maximize the directivity for a single radiating element backside-coupled to an extended hemispherical silicon lens and to solve the associated problems [Sec. 1.3.1.1]. Furthermore, it has also been demonstrated that beams produced by multiple coherent sources incorporated on a single chip, which are small relative to a wavelength, can be combined into a single Gaussian-shaped beam [171]. However, the generation of diffuse, uniform-profile illumination from large-scale arrays of incoherent THz sources incorporated in a single chip has not been addressed. Moreover, although the

generation of uniform illumination is an area of research that has received much attention for visible-light imaging, for example, in the context of light-emitting diode (LED) lamps [172]–[182], not a single work has addressed this issue for THz active imaging. That said, high-power THz diffuse, uniform illumination sources are much-needed components for THz active imaging to take another step toward producing high-quality images at a video rate. Previous attempts at overlapping and combining the beams of (several) incoherently operated THz source arrays have relied upon multi-device scaling [own5] or custom-machined device-external optics [own16], both of which are detrimental to overall size and efficiency. As opposed to the cited works, this chapter presents a simple, practical, scalable, compact, and efficient single-chip-to-single lens solution to convert an arbitrary array of THz sources into a diffuse, high-power, incoherently-combined, uniform-intensity illumination source. This solution refers to tailoring the geometry of the backside-coupled lens—without the need for any modification to the IC itself—and a proof of concept is realized using a 0.42-THz device radiating 10.3 dBm. Therefore, this thesis fills a gap in THz illumination sources required for camera-based imaging. Silicon-only single-shot THz active imaging is demonstrated in conjunction with the CMOS camera. Hence, a silicon-only THz active imaging system based on source and receiver components being incoherent silicon integrated THz arrays backside-coupled to an extended hemispherical silicon lens is developed, and a demonstration of active imaging is presented. The original contribution of this chapter to knowledge is to understand how to operate a single-chip incoherent THz source array to produce high-quality images in camera-based active imaging applications.

This chapter is a modified version of [own17], and it is outlined as follows. Section 5.2 discusses the source array SoC details relevant to this study. In Sec. 5.3, the concept of incoherent power-combining in free space is discussed concerning the generation of diffuse, incoherently-combined, uniform-profile illumination from the source array SoC. The silicon lens optimization and associated pre-estimation simulations performed in this regard are treated in Sec. 5.4. Section 5.5 describes the extensive experimental characterization and the results obtained. Measured results are carefully compared with simulations. The imaging demonstration is discussed in Sec. 5.6, and a conclusion is drawn in Sec. 5.7.

5.2 Source Array SoC

The THz diffuse, uniform illumination source combines the source array SoC presented in [19] and an optimized extended hemispherical silicon lens. The following provides details of the chip relevant to this study; for more details regarding the SoC design and its RF characterization, please refer to the cited work.

The silicon source array SoC has been implemented in a commercial SG13G2[1] SiGe bipolar CMOS (SiGe-BiCMOS) process available from IHP microelectronics that facilitates SiGe-HBTs with 0.35-THz/0.45-THz f_t/f_{max}. The chip bears an 8×8-pixel array of incoherent THz sources that together emit a total power of 10.3 dBm at ∼0.42 THz. Each source pixel consists of a power generation network directly coupled to an on-chip circular slot antenna. The footprint of a source pixel is 365 µm × 365 µm, dominated by the size of the on-chip antenna and the power generation network. Each power generation network, thereby, uses a free-running fundamental Colpitts oscillator feeding a common-collector doubler. Since the oscillators are not mutually phase-locked, the source pixels emit a non-synchronized, unlocked, or incoherent THz signal. In other words, each source pixel oscillates at a different frequency. The incoherence was verified experimentally by characterizing the mutual coupling of the source pixels, with differences in radiation frequency of hundreds of megahertz (MHz), which is small relative to the absolute radiation frequency of 0.42 THz. The differences in radiation frequency are due to process variations and variations in source pixel bias. In this context, the mutual pixel coupling, which can cause two or more pixels to lock onto the same oscillation frequency, is reduced by placing ground shields around the source pixels and the use of the silicon lens. The ground shields prevent any leakage from EM fields, while the lens suppresses undesired substrate modes [Sec. 1.3.1.1]. According to [138], incoherent THz arrays backside-coupled to an extended hemispherical silicon lens underly a mutual pixel coupling of –25 dB to –30 dB. In the source array, the values should be significantly lower due to the architecture of the source pixels. In particular, the frequency doubler blocks any in- or out-coupling of the fundamental oscillation signal. In addition to suppressing undesired substrate modes to reduce mutual coupling among the source pixels, lens-coupling enables other benefits such as improving the front-to-back radiation ratio and adding mechanical rigidity and thermal stability to the silicon chip [Sec. 1.3.1.1].

[1] https://www.ihp-microelectronics.com/de/leistungen/forschungs-und-prototyping-service/mpw-prototyping-service/sigec-bicmos-technologien

5.3 Concept of Incoherent Power-Combining in Free Space

Incoherent power-combining in free space aims at combining several far-field beams additively, in contrast to the constructive or destructive superposition of such beams in coherent power-combining. For an interference pattern to be observable over an extended period of time, two nearby light sources must hold a coherent relationship with a constant phase relationship. For example, two harmonic waves of the same frequency always have a fixed phase relationship, either in phase, out of phase, or in an intermediate position. However, since source pixels have different radiation frequencies, the phase relationship is not constant. Such light is called incoherent. Interference still occurs when waves from two incoherent light sources are superimposed in space. However, the interference pattern fluctuates as the phases of the waves shift randomly. Video-rate detectors of THz light employ a time average and therefore cannot register the quickly moving interference patterns, so only the time-averaged intensity is observed (as with the sunlight and the human eye). In order to detect interference effects, overlapping waves would have to be sampled faster than the beat period, defined as the frequency difference in the associated tones, which is on the order of hundreds of MHz. Such sampling rates are far beyond the targeted real-time capabilities in THz active imaging applications. Consequently, the approach presented here describes a form of incoherent power-combining in free space, as multiple beams are overlapped and combined into a single beam. This goes back to the fundamental of the Rayleigh criterion for incoherent light. Therefore, the source pixel beams must overlap at –3 dB or more to ensure oversampling. It is noted that the degree of overlap varies for coherent or phase-locked THz radiation and, in this case, depends on the absolute phase of the spatially overlapping harmonic waves.

5.4 Lens Design

The preceding discussions have called for backside-coupling the source array SoC to an extended hemispherical silicon lens with reduced lens extension length compared to the case optimized toward maximum directivity for central source pixels [Sec. 5.1]. Since the approach of testing several devices is very unpractical, simulations are required to pre-estimate the lens dimensions that enable the creation of the desired uniform beamform. To this end, the most accurate candidate are full-wave simulations,

for example, performed in HFSS. However, the electrically large silicon lens makes it impossible to perform such simulations due to insufficient memory. For this reason, a different approach must be taken. Mathematical models can be employed to this end [105], [107], and this was done within the scope of this thesis. The employed model is based on the cited works. In the following, the mathematical model is first described. Afterward, its verification is shown through a reference simulation performed in HFSS. Finally, simulation results are presented based on which a selection of different devices was manufactured and tested for their combined far-field radiation patterns.

5.4.1 Mathematical Model

Numerical simulations based on the theory from [105], [107] were used to solve the complex problem of identifying the lens extension length that optimizes the beam overlap for all source pixel pairs, which eventually has led to the generation of homogeneously distributed illumination from the THz source array. Concerning the mathematical model, the main difference to the cited works is the feed radiation pattern of the lens-internal antenna; a more abstract beam pattern was employed in the interests of generality:

$$|\mathbf{E}_{\text{Source}}(\theta', \phi')| = \left(\frac{\cos\theta' + 1}{2}\right)^{q}, \tag{5.1}$$

where the value q allows setting any lens-internal beam divergence of the feed, $\theta_{\text{HPBW,int}}$, parametrically:

$$q = \log\left(\frac{1}{2}\right) \cdot \left(\frac{2 \cdot \log\left(\frac{\cos\theta_{\text{HPBW,int}}}{2}\right)}{2}\right)^{-1}. \tag{5.2}$$

With regard to the accuracy of the mathematical model, it accounts for Fresnel losses, meaning that reflection losses at the air-to-silicon interface on the lens are taken into account. These losses depend on the spatial location, reshaping the overall far-field radiation pattern and thus affecting directivity. Apart from Fresnel losses, other effects due to any form of reflections within the lens are not modeled. In particular, lens-internal reflections are not included modeled. Nevertheless, it can be assumed that these effects contribute exclusively to the side lobes. Therefore, modeling such effects is of little importance since overlapping the main lobes of adjacent source pixels is intended by the presented method.

In order to construct the combined far-field radiation pattern of an incoherent THz source array with multiple radiating elements, all single-pixel far-field radiation patterns must be computed and then linearly summed, according to the previously discussed concept of incoherent power-combining in free space. Unnormalized single-pixel far-field radiation patterns must be considered to account for differences in directivity.

5.4.2 Verification of Mathematical Model

Before performing extensive simulations to identify the optimal lens dimensions of the extended hemispherical silicon lens, one must ensure that the mathematical model itself works as intended. In order to verify the mathematical model, a reference simulation was performed in HFSS. However, as stated earlier, the actual 71.7-λ lens that the source array employs is too large to simulate in HFSS. Therefore, a smaller lens was simulated in HFSS and compared with the corresponding results obtained from simulations based on the mathematical model to verify it. More specifically, a single radiating element backside-coupled to a 3-mm diameter 0.53-mm extended hemispherical silicon lens was simulated both in HFSS and through the mathematical model. Figure 5.2 serves for comparison between the two types of simulation. As seen from this figure, the main lobe is modeled exceptionally well by the mathematical model compared to the more accurate simulation performed in HFSS. As can also be seen, the sidelobes are underestimated. This fact can be attributed to non-modeled reflection-related effects, such as back-reflected fields into the lens volume and undergoing multiple subsequent reflections. As elaborated earlier, the main lobe is of primary interest to overlapping and combining far-field beams. Therefore, it can be said that the mathematical model satisfies the requirements to be met for the targeted optimization of the extended hemispherical silicon lens to produce an incoherently-combined, uniform-intensity beam from the incoherent THz source array.

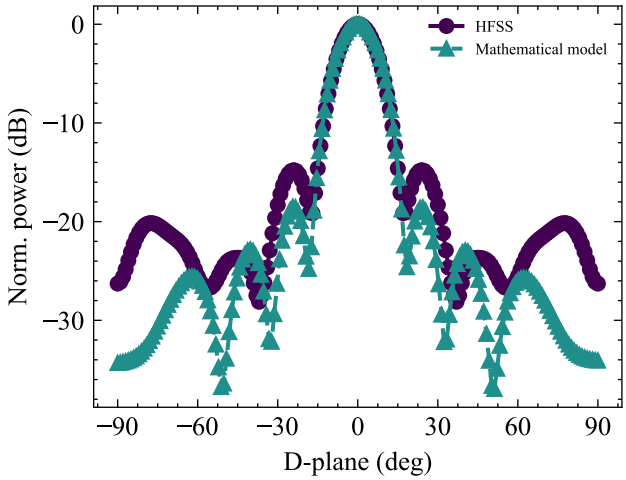

Figure 5.2. Verification of mathematical model. The mathematical model was verified by comparing a single-pixel far-field radiation pattern with results obtained from full-wave simulations in HFSS. Lens radius and lens extension length were set to 1.5 mm and 0.53 mm ($L/R = 0.353$), while simulations were performed at 0.42 THz, or in other words, for a 14.35-λ silicon lens.

5.4.3 Simulation Results

Combined far-field radiation patterns were computed for a range of normalized lens extension lengths from $L/R = 0.0$ to $L/R = 0.6$ at intervals of $L/R = 0.01$, where L is lens extension length, and R is lens radius. In order to numerically determine the combined beam patterns, single-pixel far-field radiation patterns were computed for all 8×8 source pixels positioned at the base of a 15-mm (71.7-λ) diameter extended hemispherical silicon lens, as indicated in the simulation setup shown in Fig. 5.3(a), and their unnormalized power was summed. The unnormalized power was considered in order to account for variations in directivity. The permittivity of the lens was set to 11.67[2]. It is noted that a precisely set permittivity is crucial to prevent a systematic offset in lens extension length.

D-plane cuts are a viable means to provide a comprehensive picture of the achievable combined far-field radiation pattern with respect to lens extension length. Therefore, the normalized combined D-plane cut was evaluated as a function of the normalized lens extension length, and the result is shown in Fig. 5.3(b). From this figure, it can be seen that the D-plane is oversampled for small and large values of the lens extension length, while medium values entail gaps in the FoV. What can also be seen is that small values of lens extension length go along with the creation of uniform or flat-top

[2]http://www.tydexoptics.com/products/thz_optics/thz_materials/

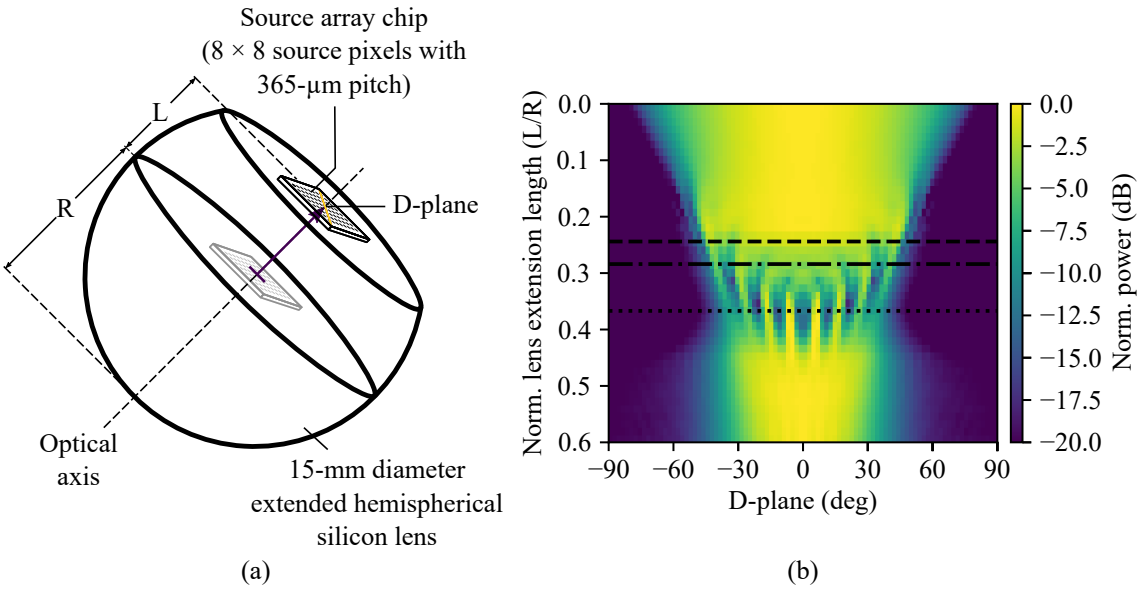

Figure 5.3. Setup and results of pre-estimation simulations. Illustration of the simulation setup employed to construct combined far-field radiation patterns (a) and combined D-plane cuts for normalized lens extension length of $L/R = 0$ to $L/R = 0.6$ (b); the D-plane is indicated in the simulation setup. In the simulations, lens radius, R, was fixed to 7.5 mm while lens extension length, L, was swept from 0–4.5 mm according to the normalized values. After [own17] © The Author(s) 2021.

illumination, as the edges of the combined beam are distinctly separated. In contrast, large values cause the beam pattern to smear toward the edges. Consequently, large lens extensions may be employed to produce a Gaussian-shaped beam intensity profile. These differences in the generated beam shape refer to the hemispherical focal surface inside the lens volume with inverted orientation to the hemispherical surface of the lens, as we know from previous discussions. To clarify, each far-field direction is associated with a different point on this surface. Off-axis displaced source pixels would have to be shifted upward (in the positive z-direction) in order to be correctly focused. This way, the curvature of the hemispherical focal surface is compensated. Shortening or increasing the lens extension essentially defocuses the center pixel, and as a consequence, its directivity is reduced. When the extension length is increased, the directivity of the off-axis displaced pixels is diminished to a larger extent than that of the center pixel because, in this case, the off-axis displaced pixels are farther away from the hemispherical focal surface. As pixel beams get broader with respect to increasing off-axis displacement, they overlap to form a Gaussian beam. However, when shortened, the off-axis displaced pixels are raised upward in the positive z-direction, again defocusing the center pixels. Therefore, off-axis displaced pixels are brought closer to the hemispherical focal surface than the center pixel. In this case,

the reduction in directivity for off-axis displaced pixels is smaller than for center pixels. As pixel beams get narrower with respect to increasing off-axis displacement, they overlap to form a uniform beam. Another noteworthy point observable from Fig. 5.3(b) is that the FoV decreases with respect to increasing lens extension length. It is remembered that the overarching aim was to create uniform illumination from the source array at a minimal FoV. For this reason, an extension just above cases associated with (partial) FoV undersampling offers the most promising prospect. Here, uniform illumination is produced at a minimal FoV; a smaller FoV is desirable concerning realizing larger f-number quasi-optical systems for applications in THz active imaging, being more accessible to align than those with very small f-numbers.

Following the above discussion, a normalized lens extension length of $L/R = 0.244$ was selected for fabrication and testing to create diffuse, incoherently-combined, uniform illumination from the THz source array. In addition, two other cases with normalized lens extension lengths of $L/R = 0.284$ and $L/R = 0.367$ were selected for fabrication and testing to transport a comprehensive picture. While the case of $L/R = 0.284$ is intended to oversample a central portion of the FoV, the $L/R = 0.367$ case is intended to undersample the entire FoV. It is noted that this second case describes the lens design implemented in previous works [19], [20].

5.5 Far-Field Radiation Pattern Characterization

This section discusses the experimental far-field characterization, thereby showing the experimental setup and the measured results.

5.5.1 Experiment

Figure 5.4 shows the experimental setup used for the far-field characterization of the three fabricated devices. The radiated THz signal of these devices was successively measured with a SiGe-HBT THz direct power detector, which shows an NEP of 8 pW/$\sqrt{\text{Hz}}$ at ∼0.42 THz [115]. A far-field distance of 70 cm, exceeding the Fraunhofer distance of $2 \cdot D^2/\lambda = 63$ cm for the 15-mm-diameter lens at 0.42 THz, separated the tested devices and the detector. While the detector was fixed in place, the source arrays were attached to a six-axis table-top robot arm to facilitate a rotational raster scan for relative power measurements. Each device was scanned over a $\pm 36° \times \pm 36°$-sector of the hemisphere.

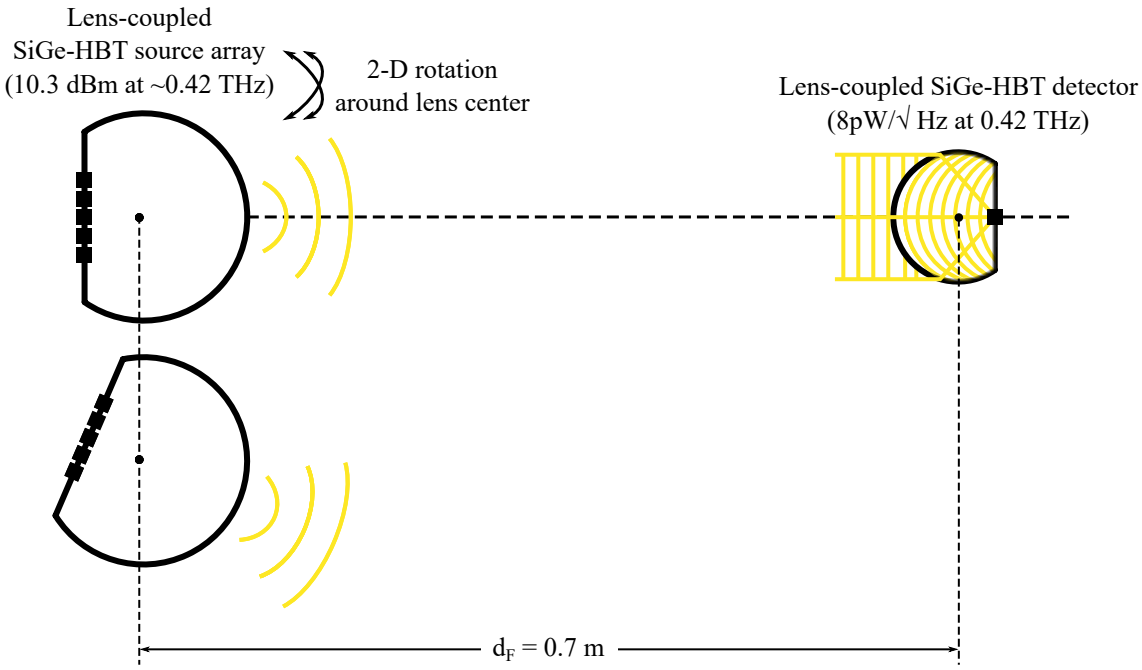

Figure 5.4. Far-field radiation pattern characterization setup. Illustration of the experimental setup used for far-field radiation characterization. The three devices with lenses of different extension lengths were subsequently employed in this setup. Thereby, all source pixels were active each.

5.5.2 Measured Results and Discussions

Figures 5.5 (a), (b), and (c) show the normalized measured combined far-field radiation patterns for lenses with normalized lens extension lengths of $L/R = 0.367$, $L/R = 0.284$, and $L/R = 0.244$, respectively. The results confirm that the beam overlap (or fill factor) increases with respect to decreasing lens extension length. The corresponding D-plane cuts are brought into perspective with simulations in Figs. 5.5(d)–(f). As can be seen, there is an excellent agreement between measurements and simulations. Quantitatively, the normalized lens extension lengths of $L/R = 0.367$, $L/R = 0.284$, and $L/R = 0.244$ allow covering experimentally-tested FoVs of 50°, 55°, and 55°, with 3-dB fill factors of 6.5%, 53.4%, and 99.98%, respectively. The corresponding values in peak-to-peak ripple are 20 dB, 8.6 dB, and 3.5 dB. Thus, the main objective, namely the realization of a high-power diffuse THz source with a uniform or flat-top beam profile, has been achieved. Since the measurements are in great agreement with simulations, it can be concluded that the mathematical model has been successfully verified.

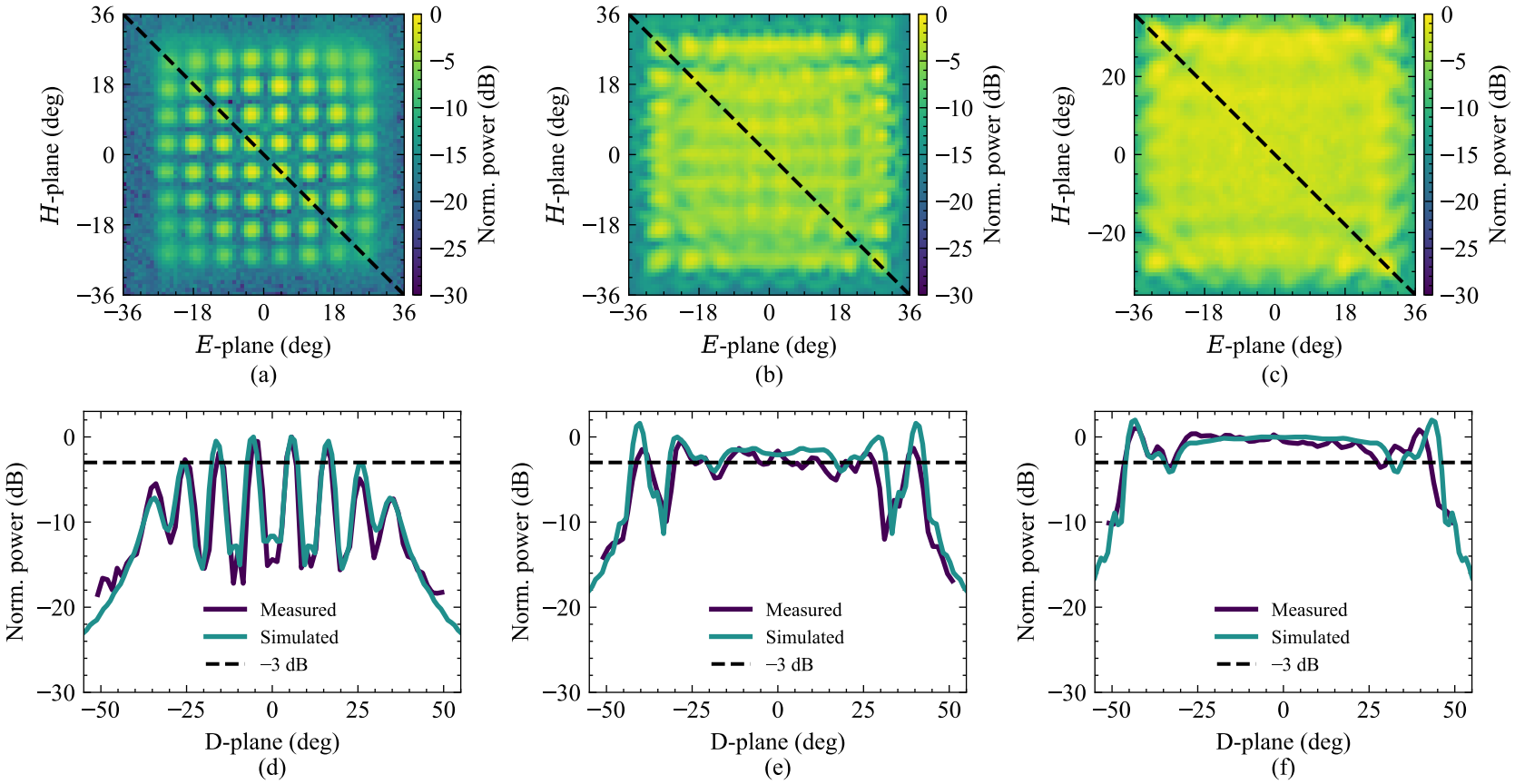

Figure 5.5. Measured combined far-field radiation patterns. Measured combined far-field radiation patterns of source arrays using lenses with different normalized lens extension lengths of $L/R = 0.367$ (a), $L/R = 0.284$ (b), and $L/R = 0.244$ (c). In (d)–(f), cuts in the D-plane along the dashed line in the corresponding combined far-field radiation patterns from (a)–(c) are compared with the results from simulations. In all subfigures, normalization is performed with respect to the maximum power within the FoV. After [own17] © The Author(s) 2021.

5.6 Demonstration of Silicon-Only THz Active Imaging

In the following, the single-shot imaging setup employed to demonstrate silicon-only THz active imaging using the uniform-beam device developed here and a CMOS camera is detailed. After that, the associated imaging results are provided.

5.6.1 Single-Shot Imaging Setup

Figure 5.6(a) and (b) shows an illustration of the single-shot imaging setup used to demonstrate silicon-only acTHz active imaging and a photo of it, respectively. The directional-beam device and the uniform-beam device were successively deployed in an imaging experiment to demonstrate the issue of undersampling and that homogeneously sampled images can be produced, respectively. The source arrays emit a total of 10.3 dBm [19] at 0.42 THz, where the video-rate NEP of the camera is 2.5 µW [own14]. Each component was fixed in a cage system to secure mechanical rigidity. The presented imaging setup spans a size of $136 \times 50 \times 50$ mm^3, thus being portable. It is noted that this single-shot imaging setup for THz active imaging is not tied to a CMOS camera. Other direct power detectors, such as microbolometers [152], CMOS-NEMS [153], SiGe HBTs [114], and Schottky barrier diodes [154], can replace the CMOS detectors, in principle.

The imaging setup bears a THz source array, a series of optics, and a THz camera. On the source array side, a 50-mm diameter collimating PTFE lens with an f-number of 0.72 (L1), which closely corresponds to the source array FoVs of 50° and 55°. The center of the source array lens, where central rays of the source pixel beams converge [75], coincides with the focal point of L1, x_0. As the source array emits divergent wavefronts emanating from this point, approximately plane waves are generated in the imaging plane, x_1. Accordingly, the center of the camera lens coincides with the focal point of the right-handed collimating PTFE lens (L2; diameter of 50 mm and f-number of 1), namely x_2. This lens closely corresponds to the 46° FoV of the camera. Therefore, the imaging plane is projected onto the camera lens. An object placed in the imaging place will appear as an inverted image on the FPA surface. Recall that this ray-optics simplification only applies to placing an object in the focus of the camera lens and that the object must be placed in such focus to produce a highly resolved image.

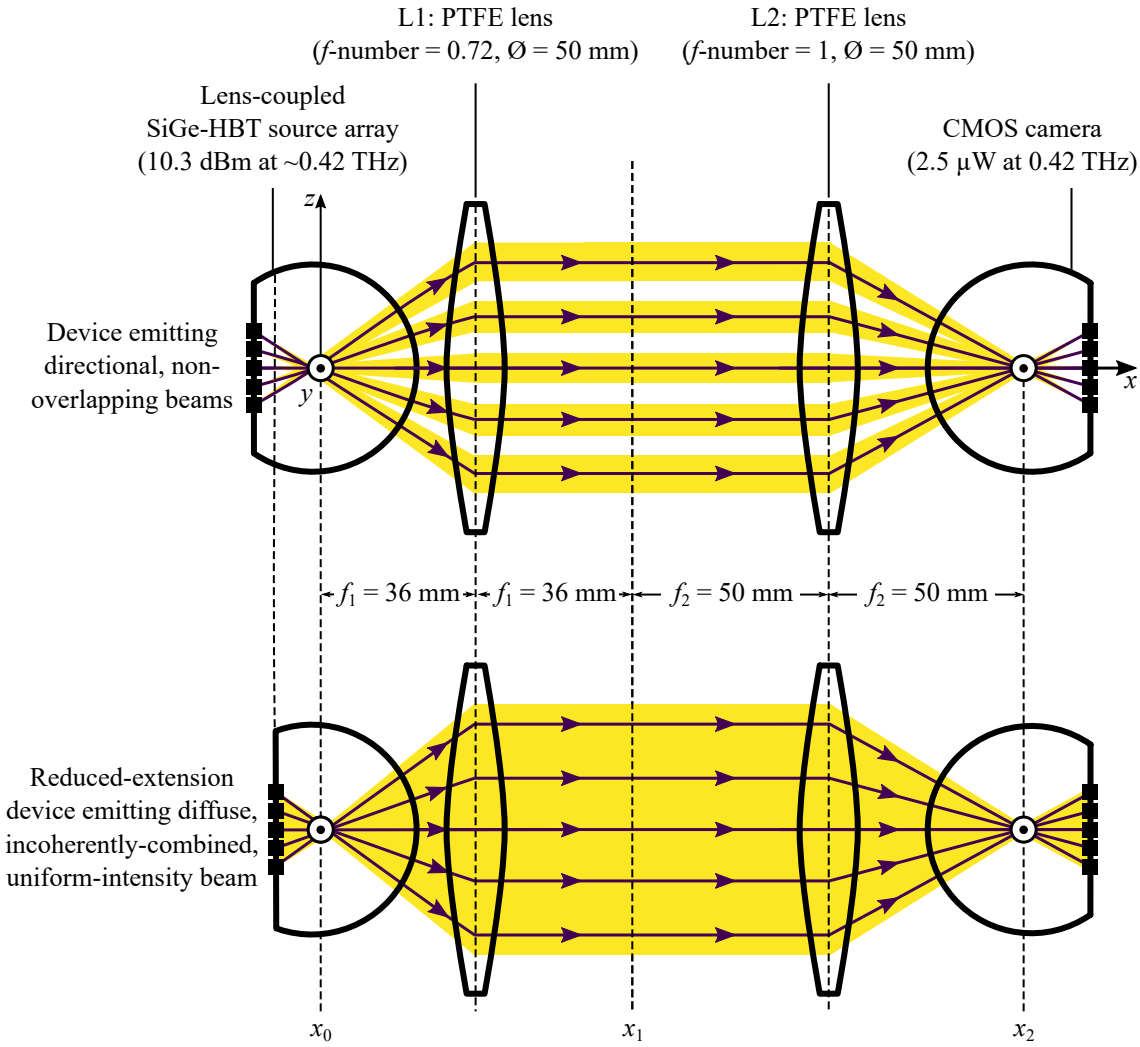

(a)

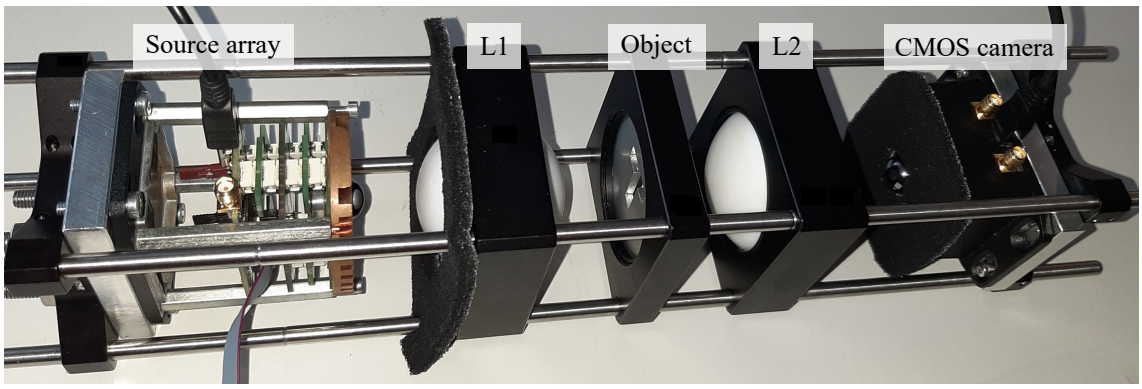

(b)

Figure 5.6. Single-shot silicon-only THz active imaging setup. (a) Illustration of the experimental setup employed for silicon-only THz active imaging using the source array emitting directional, non-overlapping beams that lead to undersampling of the imaging plane, and the diffuse, uniform-intensity device (b), as well as a representative photo for both such setups (c). Subfigure (b) is after [own17] © The Author(s) 2021.

5.6.2 Imaging Results

Figures 5.7 (a) and (b) show THz images of the imaging target. A visual image of the object that served as the imaging target is shown in figure insets. This object is a 3-mm-thick metal plate with a diameter of 50 mm and a T-shaped cutout, and it blocked most of the beam, allowing only a small fraction of it to pass. Each image was acquired throughout ∼30 seconds, since the CMOS camera was operated at 30 fps, forming an average of 1024 frames. Frame averaging was applied in order to increase SNR [own4]. The THz image shown in Fig. 5.7(a), which was generated using the directional-beam device, is undersampled. In contrast, the THz image shown in Fig. 5.7(b), which was produced using the uniform-beam device, is oversampled. Therefore, the "T" is only visible in the latter.

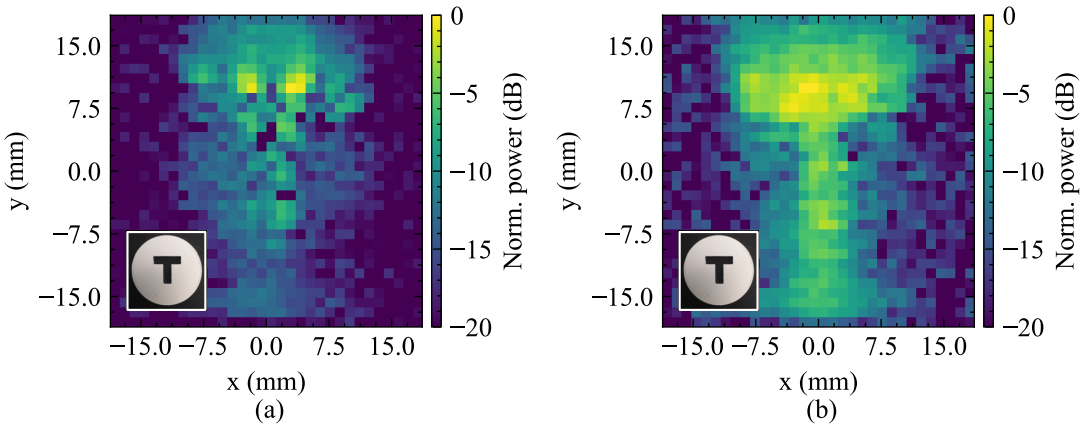

Figure 5.7. Results of single-shot silicon-only THz active imaging. THz images of the imaging target shown in figure insets using the directional-beam device (a) and the uniform-beam device (b). After [own17] © The Author(s) 2021.

5.7 Chapter Conclusion

In this chapter, a practical and scalable solution for operating a single-chip incoherent silicon integrated THz source arrays as a diffuse, uniform-intensity illumination source has been demonstrated. Briefly, this method relies upon optimizing the geometry of the backside-coupled extended hemispherical silicon lens. This method was applied to the device from [19], thereby realizing a 0.42-THz source with a homogeneously distributing 10.3 dBm over its FoV. Based on this device and a CMOS THz camera, an all-electronic, cost-effective, and compact solution for high-performing THz active imaging with real-time capabilities has been realized.

As we know, all kinds of single-element integrated THz sources suffer from low radiation power and are relatively large in terms of wavelength [Sec. 1.3.1], and lens-coupling is ubiquitous among THz sources [Sec. 1.3.1.1]. For these reasons, the technique presented here is of general utility for power-combining in free space. Moreover, power-combining in free space would also be possible with coherent devices. However, special attention must be paid to the phase relationship among the individual elements in this case. Either way, this type of scalable coherent power-combining could be essential for photo-mixing emitters that exhibit broad frequency tunability but currently suffer from low radiated power at high frequencies. An array of THz photo-mixing sources could be fed by a single high-power beating laser, leading to innate synchronization between adjacent sources of coherent radiation.

In some instances, a Gaussian-shaped intensity profile may be preferred to a uniform beam profile. This type of beam profile can also be achieved based on the silicon lens optimization facilitated here, namely by increasing instead of shortening the lens extension length with respect to the case yielding maximum directivity. In this case, the directivity of the combined beam will also increase compared to the uniform-beam case, which may be of great benefit to some applications, like THz radar or THz wireless communications.

Chapter 6

Conclusion and Outlook

6.1 Conclusion

This thesis has started with a general discussion on THz applications and available THz instrumentation. In this regard, the transition to silicon process technologies has been motivated, and the case was made for silicon integrated THz arrays of incoherently operated sources and detectors backside-coupled to an extended hemispherical silicon lens. While devices based on incoherent sources are key components in overcoming the limitations of radiation power in the THz range, devices based on incoherent detectors are essentially cameras that allow forming an image without the necessity for mechanical scanning. With this in mind, this thesis has aimed at a better understanding of how their combined far-field radiation pattern affects their performance in THz active imaging applications, which they were invented for in the first place. The original contribution of this thesis to knowledge is, on the one hand, to understand this aspect in full detail. This understanding is crucial to know how to operate such devices in THz active imaging to achieve optimal performance in terms of producing highly resolved images. Furthermore, this is crucial to know how to operate such a camera to achieve optimal performance in THz spectroscopy applications and THz antenna measurements.

The frequency-dependent limits in angular resolution and associated spatial resolution that can be achieved with silicon integrated THz cameras have been discussed. Understanding this aspect is crucial to know how to operate them to achieve the maximum achievable, diffraction-limited spatial resolution in active imaging

applications. The broadband nature of the camera pixels entails over- and undersampling frequency ranges. With undersampling, the angular resolution is geometrically limited to the beam separation angle between adjacent camera pixels. Super-resolution imaging breaks this geometrical angular resolution limit to achieve the diffraction-limited angular resolution given by the camera lens. For a device that employs a 2.75-mm extended 15-mm diameter hemispherical silicon lens, a diffraction-limited angular resolution of 1.64° was achieved in a super-resolution imaging experiment performed at 0.652 THz, which translated into a spatial resolution of 1.43 mm at a 50-mm diameter illumination aperture. Since these values align closely with a conventionally employed criterion for determining the angular or spatial resolution of optical systems, namely the Sparrow criterion, this criterion can be used for prediction purposes. At 1 THz, the predicted angular and spatial resolution achievable using super-resolution imaging is 1.1° and 0.96 mm, respectively, while a narrower illumination aperture of, say, 30 mm would result in an even better spatial resolution of 0.58 mm. The diffraction-limited angular resolution primarily depends on the radiation frequency and the silicon lens dimensions. Besides a higher radiation frequency, a larger lens is advantageous in terms of angular resolution. With this study, this thesis substantially contributes to the field of THz active imaging by providing an understanding of how to achieve optimal performance in terms of spatial resolution with such cameras in actual applications.

The application concept of the THz dispersive spectroscope combining such a camera and a series of optics, including a dispersive optic, has also been presented and experimentally verified. This incoherent application concept serves as an alternative solution to coherently operated systems for the discipline of silicon-based THz spectroscopy. Contemporary coherent solutions are rather narrowband. In contrast, the herein followed approach yields an immense bandwidth by leveraging the broadband operation of the incoherently operated camera pixels. In this regard, the device characterized here was optimized for broadband operation in the first place. Specifically, a usable operating bandwidth of 0.3–1.1 THz was achieved. Although a single dispersive optic cannot cover such large bandwidth, this was achieved by leveraging the modularity of the dispersive optic, using two different dispersive optics targeting design frequencies of 0.46 THz and 0.85 THz; other dispersive optics may be employed to extend the bandwidth even further. The capabilities of this incoherent system approach far exceed those of coherent systems in terms of operating bandwidth. However, the considerable operating bandwidth is achieved at the cost of spectral

resolution and frequency accuracy, being in the range of several tens of GHz, limited by the finite pixel count of the camera. Super-resolution imaging was employed to boost the pixel count and improve performance in these parameters while maintaining broadband capabilities. In this context, the fundamental performance limits have been determined. With the help of super-resolution imaging, the spectral resolution can be improved by at least a factor of two, thereby reaching the diffraction-limited angular resolution of the camera. Specifically, the average spectral resolution improved from 68.3 GHz to 34.2 GHz in the experiment performed from 0.75–0.9 THz. Unlike physically integrating more pixels, super-resolution imaging yields a cost-effective solution. In addition to improving spectral resolution, frequency accuracy has been shown to scale approximately with the number of low-resolution images used to produce a super-resolution image. In the experiment performed from 0.75–0.9 THz, a total of 22 low-resolution images yielded an average improvement by a factor of 18.2 from 30 GHz to 1.65 GHz. It should be noted that this performance is still not nearly enough to support applications in THz gas spectroscopy, for instance, since these require a much better spectral resolution due to the sharp spectral lines of gases, but it may be acceptable for inspecting spectral masks of solids, for example. In any case, super-resolution imaging will be of general utility as a technique to reach the maximum achievable, diffraction-limited spectral resolution of any THz dispersive spectroscope, at least by a factor of two, and substantially improve upon frequency accuracy, roughly scaling with the number of low-resolution images used to produce a super-resolution image. As the maximum achievable spectral resolution is concerned with the diffraction limit, this performance metric becomes a function of system size; physically larger systems will generally exhibit better spectral resolution. In contrast, the frequency accuracy will generally improve for camera pixels with better NEP, which relates directly to SNR. With this study, this thesis substantially contributes to the field of THz spectroscopy by providing a low-cost alternative for broadband operation at a moderate spectral resolution and frequency accuracy.

Another application concept, namely the camera-type THz CATR based upon the same sort of camera as discussed above, has been presented and experimentally verified. With this, a THz camera is employed to determine the far-field characteristics of radiation sources at a compact range, including the radiation pattern, directivity, HPBW, and radiation power. This application concept refers to conventional CATRs, with the difference that the far-field characteristics of an AUT can be determined without or by drastically reducing mechanical sampling. Without spatial sampling is

given for low-resolution imaging, whereas some sampling is required when employing super-resolution imaging. In this context, the effect of super-resolution imaging on the determination of the far-field characteristics was investigated, which aims at improved performance due to better angular resolution. Super-resolution imaging yielded determining directivity, HPBW, and radiation power from far-field radiation patterns measured at a compact range within RMS accuracies of 0.85 dB, 1.1°, and 0.7 µW. The first two values relate to reference measurements performed at a far-field range, while the third relates to a reference measurement performed with a conventionally employed absolute power meter. This performance can be expected for antennas with a diameter within the minimum and maximum AUT size identified of 0.62–0.34 mm and 7.5 mm from 0.6–1.1 THz. Minimum and maximum AUT size inspectable through the presented THz CATR relates to limitations in FoV and angular resolution of the camera, respectively. New devices may allow characterizing smaller or larger AUTs, based on the geometry of the extended hemispherical silicon lens and the FPA of the camera. Although low-resolution imaging accompanies deteriorated performance in determining these far-field characteristics, it provides a straightforward, practical, and fast method for testing the far-field characteristics by single-shot measurements since it does not require any form of mechanical scanning. Combined with the concept of THz dispersive spectral analysis, a CMOS camera is now capable of performing complete far-field characterization of THz radiation sources, such as the far-field radiation pattern, directivity, HPBW, radiation power, radiation frequency, and harmonic content. The first four parameters are attributed to the CATR operation of the THz camera, whereas the last two parameters relate to its spectroscope operation. With this application concept, this thesis substantially contributes to the field of THz antenna measurements by providing a convenient means for rapid far-field characteristics determination of radiation sources.

A practical and scalable method for operating an incoherent silicon integrated THz source array as a diffuse, uniform illumination source has also been demonstrated, representing a novel illumination concept for THz active imaging. This method refers to tailoring the dimensions of the backside-coupled extended hemispherical silicon lens—without the need for any modification to the IC itself—and a proof of concept was realized using a 0.42-THz device radiating 10.3 dBm. In this way, incoherent silicon integrated THz source arrays can now be used to realize single-shot THz active imaging systems solely based on silicon integrated components that produce high-quality images, are portable, enable high imaging speed, and

are cost-effective. Silicon-only THz active imaging using the proof-of-concept diffuse, incoherently-combined, uniform-intensity beam device presented here has been demonstrated along with a CMOS THz camera. The concept of incoherent power-combining in free space by tailoring the geometry of the backside-coupled extended hemispherical silicon lens will be of general utility as a free-space power-combining technique for all kinds of THz radiation sources, as they all suffer from a low radiation power. With this illumination concept, this thesis substantially contributes to the discipline of THz active imaging by significant improvements in the field of illumination sources. The discussions conducted in this work cover how to generate a uniform beam profile, as intended here with respect to THz active imaging, as well as how to create a Gaussian beam profile, which may be desirable for other applications in the fields of THz communications, THz radar, and THz spectroscopy. Therefore, with this study, this thesis also contributes to the field of THz radiation sources by providing a viable means for high-power single-beam operation of incoherent THz source arrays.

6.2 Outlook

The question arises regarding a common ground concerning future directions for the various investigations carried out in this work. This common ground is defined in the research project T-MAP funded by DFG. Briefly, T-MAP is concerned with realizing a mobile, lightweight, and low-cost THz dispersive spectroscope operating from 0.15–1.5 THz with minimum SNR of 30 dB and a spectral resolution and frequency accuracy of a few GHz each. The THz dispersive spectroscope envisaged in this project will consist of a silicon integrated camera using an extended hemispherical silicon lens and a series of optics involving a dispersive element, like the one presented and tested here. In addition to realizing this spectroscope, T-MAP aims to realize an all-silicon THz dispersive spectrometer by upgrading it with a suitable radiation source integrated into silicon process technologies.

The research presented in this dissertation helps T-MAP understand the optimal subcomponent and system design tradeoffs of silicon-based THz dispersive spectroscopes. To this end, the detailed characterization of the THz dispersive spectroscope was performed in the scope of this thesis. The system studied here works as intended. Although the modularity of the dispersive component of the spectroscope allows covering different frequency bands and thus to optimize the SNR

in these bands, this may not be sufficient to cover a decade of the THz bandwidth with an SNR of 30 dB. This is because the CMOS camera employed for initial testing is relatively insensitive to frequencies below 0.6 THz. T-MAP will need to develop a detector array that constitutes several columns of detectors optimized for different subbands of THz radiation in terms of NEP.

Super-resolution imaging, which has been a subject of this thesis, was also employed as a tool to analyze the fundamental spectral resolution and frequency accuracy limits of THz dispersive spectroscopes. It has been found that a detector array of far-superior pixel count compared to state-of-the-art devices would be required to realize the proposed spectral resolution and frequency accuracy of a few GHz, which would be a costly solution. On the other hand, super-resolution imaging is, in principle, free of charge and thus represents a practical solution to achieve the spectroscope performance required for practical applications in terms of spectral resolution and frequency accuracy. In this analysis, the source of the THz dispersive spectrometer proposed in T-MAP is omitted and therefore needs to be considered in the future, as it will also contribute to these performance metrics.

Most importantly, a suitable silicon integrated source is missing to convert the spectroscope into a spectrometer solely based on silicon integrated components, which will be capable of analyzing already packaged goods for material properties. To this end, T-MAP envisages the implementation of a silicon integrated broadband THz pulsed source. One obstacle that T-MAP will face in this regard is radiation power constraints. Recall that this thesis has presented a novel concept of incoherent power-combining in free space by tailoring the dimensions of the backside-coupled extended hemispherical silicon lens. An array of antenna-coupled pulsed sources integrated into a single silicon chip may be equipped with such an optimized lens, demonstrating some form of a power-combining antenna to achieve greater overall radiation power; the use of a power-combining antenna was envisaged by T-MAP, albeit based upon a different method. In this context, increasing the lens extension length of the extended hemispherical silicon lens is recommended instead of shortening it to generate a Gaussian beam narrower than the uniform beam produced here.

Bibliography

Own Publications

[own1] R. Jain, P. Hillger, J. Grzyb, *et al.*, "34.3 A 32×32 Pixel 0.46-to-0.75THz Light-Field Camera SoC in 0.13µm CMOS," in *Proc. IEEE Int. Solid-State Circ. Conf.*, vol. 64, San Francisco, CA, USA, 2021, pp. 484–486. DOI: 10.1109/ISSCC42613.2021.9365832.

[own2] R. Zatta, R. Jain, J. Grzyb, and U. R. Pfeiffer, "Resolution Limits of Hyper-Hemispherical Silicon Lens-Integrated THz Cameras Employing Geometrical Multiframe Super-Resolution Imaging," *IEEE Trans. Terahertz Sci. Technol.*, vol. 11, no. 3, pp. 277–286, 2021. DOI: 10.1109/TTHZ.2021.3063839.

[own3] R. Zatta, R. Jain, J. Grzyb, and U. R. Pfeiffer, "Resolution Limits in Lens-Integrated CMOS THz Cameras Employing Super-Resolution Imaging," in *Proc. Int. Conf. Infrared, Millimeter, Terahertz Waves*, Paris, France, Sep. 2019, pp. 1–2. DOI: 10.1109/IRMMW-THz.2019.8874510.

[own4] R. Zatta, R. Jain, and U. R. Pfeiffer, "Characterization of the noise behavior in lens-integrated CMOS terahertz video cameras," *J. Terahertz Sci. Technol.*, vol. 11, no. 4, pp. 102–123, Dec. 2018. DOI: 10.11906/TST.102-123.2018.12.10.

[own5] R. Zatta, R. Jain, D. Headland, and U. R. Pfeiffer, "Incoherent Power Combining of THz Source Arrays," in *Proc. Int. Conf. Infrared Millim. Terahertz Waves*, Paris, France, Sep. 2019, pp. 1–2. DOI: 10.1109/IRMMW-THz.2019.8874075.

[own6] D. Headland, R. Zatta, P. Hillger, and U. R. Pfeiffer, "Terahertz Spectroscope Using CMOS Camera and Dispersive Optics," *IEEE Trans. Terahertz Sci. Technol.*, vol. 10, no. 5, pp. 513–523, Jun. 2020. DOI: 10.1109/TTHZ.2020.3004516.

[own7] R. Zatta and U. R. Pfeiffer, "Performance Limits of THz Dispersive Spectroscopes Employing Super-Resolution Imaging," *IEEE Trans. Terahertz Sci. Technol.*, vol. 11, no. 6, pp. 1–8, 2021. DOI: 10.1109/TTHZ.2021.3088278.

[own8] D. Headland, P. Hillger, R. Zatta, and U. Pfeiffer, "Incoherent, spatially-mapped THz spectral analysis," in *Proc. Int. Conf. Infrare, Millim. Terahertz Waves*, Nagoya, Japan, Sep. 2018, pp. 1–2. DOI: 10.1109/IRMMW-THz.2018.8510246.

[own9] R. Zatta, V. Jagtap, J. Grzyb, and U. R. Pfeiffer, "Broadband Lens-Integrated CMOS Camera-Type THz Compact Antenna Test Range," *IEEE Trans. Terahertz Sci. Technol.*, vol. 11, no. 5, pp. 527–537, 2021. DOI: 10.1109/TTHZ.2021.3088286.

[own10] R. Zatta, V. S. Jagtap, J. Grzyb, and U. R. Pfeiffer, "CMOS THz Camera Used as Compact Antenna Test Range," in *Proc. Int. Worksh. Mob. Terahertz Syst.*, Essen, Germany, 2020, pp. 1–4. DOI: 10.1109/IWMTS49292.2020.9166379.

[own11] R. Zatta, V. S. Jagtap, J. Grzyb, and U. R. Pfeiffer, "CMOS Camera-Type THz Compact Antenna Test Range for Far-Field Radiation Pattern Analysis," in *Proc. Int. Conf. Infrared Millim. Terahertz Waves*, Buffalo, NY, USA, Nov. 2020, pp. 1–2. DOI: 10.1109/IRMMW-THz46771.2020.9370372.

[own12] V. S. Jagtap, R. Zatta, S. Nellen, B. Globisch, J. Grzyb, and U. R. Pfeiffer, "Broadband Spectro-Spatial Characterization of CW Terahertz Photoemitter Using CMOS Camera," in *Proc. Int. Conf. Infrared Millim. Terahertz Waves*, Buffalo, NY, USA, Nov. 2020, pp. 1–2. DOI: 10.1109/IRMMW-THz46771.2020.9370841.

[own13] R. Jain, R. Zatta, J. Grzyb, D. Harame, and U. R. Pfeiffer, "A Terahertz Direct Detector in 22nm FD-SOI CMOS," in *Proc. Eur. Microw. Integr. Circuits Conf.*, Madrid, Spain, 2018, pp. 25–28. DOI: 10.23919/EuMIC.2018.8539908.

[own14] V. S. Jagtap, R. Zatta, J. Grzyb, and U. R. Pfeiffer, "Performance Characterization Method of Broadband Terahertz Video Cameras," in *Proc. Int. Conf. Infrared Millim. Terahertz Waves*, Paris, France, Sep. 2019, pp. 1–2. DOI: 10.1109/IRMMW-THz.2019.8874478.

[own15] R. Zatta and U. R. Pfeiffer, "Radial Distortion in Silicon Lens-Integrated THz Cameras," in *Proc. Int. Conf. Infrared Millim. Terahertz Waves*, IEEE, Sep. 2021, pp. 1–2. DOI: 10.1109/IRMMW-THz50926.2021.9567497.

[own16] D. Headland, R. Zatta, and U. R. Pfeiffer, "Diffuse beam with electronic THz source array," in *Proc. Int. Conf. Infrared Millim. Terahertz Waves*, Nagoya, Japan, Sep. 2018, pp. 1–2. DOI: 10.1109/IRMMW-THz.2018.8509901.

[own17] R. Zatta, D. Headland, E. Ashna, *et al.*, "Silicon Lens Optimization to Create Diffuse, Uniform Illumination from Incoherent THz Source Arrays," *J. Infrared Millim. Terahertz Waves*, pp. 1–13, 2021. DOI: 10.1007/s10762-021-00828-0.

Cited References

[1] D. Abbott and X.-C. Zhang, "Special Issue on T-ray Imaging, Sensing, and Retection," *Proc. IEEE*, vol. 95, no. 8, pp. 1509–1513, 2007. DOI: 10.1109/JPROC.2007.900894.

[2] J. C. Wiltse, "History of Millimeter and Submillimeter Waves," *IEEE Trans. Microw. Theory Techn.*, vol. 32, no. 9, pp. 1118–1127, 1984. DOI: 10.1109/TMTT.1984.1132823.

[3] A. Glagolewa-Arkadiewa, "Short Electromagnetic Waves of Wave-length up to 82 Microns.," *Nat.*, vol. 113, no. 2844, pp. 640–640, 1924. DOI: 10.1038/113640a0.

[4] P. H. Siegel, "Terahertz technology," *IEEE Trans. Microw. Theory Techn.*, vol. 50, no. 3, pp. 910–928, 2002. DOI: 10.1109/22.989974.

[5] A. Goldsmith, *Wireless communications*. Cambridge university press, 2005.

[6] M. Oliveira and A. Franca, "Microwave heating of foodstuffs," *J. Food Eng.*, vol. 53, no. 4, pp. 347–359, 2002. DOI: 10.1016/S0260-8774(01)00176-5.

[7] L. Weinstein, "Electromagnetic waves," *Radio i svyaz', Moscow*, 1988.

[8] J. M. Lloyd, *Thermal imaging systems*. Springer Science & Business Media, 2013.

[9] T. M. Buzug, "Computed Tomography," in *Springer Handb. Med. Technol.* Springer, 2011, pp. 311–342. DOI: 10.1007/978-3-540-74658-4_16.

[10] K. Cheung and D. Auston, "A novel technique for measuring far-infrared absorption and dispersion," *Infrared Phys.*, vol. 26, no. 1, pp. 23–27, 1986. DOI: 10.1016/0020-0891(86)90043-6.

[11] D. Grischkowsky, S. Keiding, M. Van Exter, and C. Fattinger, "Far-infrared time-domain spectroscopy with terahertz beams of dielectrics and semiconductors," *JOSA B*, vol. 7, no. 10, pp. 2006–2015, 1990. DOI: 10.1364/JOSAB.7.002006.

[12] W. Withayachumnankul and M. Naftaly, "Fundamentals of Measurement in Terahertz Time-Domain Spectroscopy," *J. Infrared Millim. Terahertz Waves*, vol. 35, no. 8, pp. 610–637, 2014. DOI: 10.1007/s10762-013-0042-z.

[13] A. Roggenbuck *et al.*, "Coherent broadband continuous-wave terahertz spectroscopy on solid-state samples," *New J. Phys.*, vol. 12, no. 4, 2010. DOI: 10.1088/1367-2630/12/4/043017.

[14] S. Matsuura, M. Tani, and K. Sakai, "Generation of coherent terahertz radiation by photomixing in dipole photoconductive antennas," *Appl. Phys. Lett.*, vol. 70, no. 5, pp. 559–561, 1997. DOI: 10.1063/1.118337.

[15] M. Tani, P. Gu, M. Hyodo, K. Sakai, and T. Hidaka, "Generation of coherent terahertz radiation by photomixing of dual-mode lasers," *Opt. Quantum Electron.*, vol. 32, no. 4, pp. 503–520, 2000. DOI: 10.1023/A:1007070931314.

[16] S. Preu, G. Döhler, S. Malzer, L. Wang, and A. Gossard, "Tunable, continuous-wave terahertz photomixer sources and applications," *J. Appl. Phys.*, vol. 109, no. 6, pp. 4–61, 2011. DOI: 10.1063/1.3552291.

[17] NICT/RIKEN, *Terahertz spectral database*, http://thzdb.org/.

[18] NICT, *Terahertz spectral database*, https://webbook.nist.gov/chemistry/thz-ir/.

[19] R. Jain, P. Hillger, E. Ashna, J. Grzyb, and U. R. Pfeiffer, "A 64-Pixel 0.42-THz Source SoC With Spatial Modulation Diversity for Computational Imaging," *IEEE J. Solid-State Circuits*, vol. 55, no. 12, pp. 3281–3293, 2020. DOI: 10.1109/JSSC.2020.3018819.

[20] U. R. Pfeiffer, Y. Zhao, J. Grzyb, *et al.*, "A 0.53 THz reconfigurable source module with up to 1 mW radiated power for diffuse illumination in terahertz imaging applications," *IEEE J. Solid-State Circuits*, vol. 49, no. 12, pp. 2938–2950, 2014. DOI: 10.1109/JSSC.2014.2358570.

[21] R. Al Hadi, H. Sherry, J. Grzyb, *et al.*, "A 1 k-Pixel Video Camera for 0.7–1.1 Terahertz Imaging Applications in 65-nm CMOS," *IEEE J. Solid-State Circuits*, vol. 47, no. 12, pp. 2999–3012, 2012. DOI: 10.1109/JSSC.2012.2217851.

[22] D. M. Mittleman, "Twenty years of terahertz imaging," *Opt. Express*, vol. 26, no. 8, pp. 9417–9431, 2018. DOI: 10.1364/OE.26.009417.

[23] M. Tonouchi, "Cutting-edge terahertz technology," *Nat. Photonics*, vol. 1, no. 2, pp. 97–105, 2007. DOI: 10.1038/nphoton.2007.3.

[24] R. E. Miles, X.-C. Zhang, H. Eisele, and A. Krotkus, *Terahertz Frequency Detection and Identification of Materials and Objects*. Springer Science & Business Media, 2007. DOI: 10.1007/978-1-4020-6503-3.

[25] J. F. Federici, B. Schulkin, F. Huang, *et al.*, "THz imaging and sensing for security applications—explosives, weapons and drugs," *Semicond. Sci. Technol.*, vol. 20, no. 7, S266, 2005.

[26] G. Tzydynzhapov, P. Gusikhin, V. Muravev, A. Dremin, Y. Nefyodov, and I. Kukushkin, "New Real-Time Sub-Terahertz Security Body Scanner," *J. Infrared Millim. Terahertz Waves*, vol. 41, no. 6, pp. 632–641, 2020. DOI: 10.1007/s10762-020-00683-5.

[27] D. Etayo, J. Iriarte, I. Palacios, *et al.*, "THz Imaging System for Industrial Quality Control," in *Proc. IEEE MTT-S Int. Microwave Workshop Ser, Millim. Wave Integr. Technol.*, IEEE, Sitges, Spain, 2011, pp. 172–175. DOI: 10.1109/IMWS3.2011.6061867.

[28] D. L. Woolard, R. Brown, M. Pepper, and M. Kemp, "Terahertz Frequency Sensing and Imaging: A Time of Reckoning Future Applications?" *Proc. IEEE*, vol. 93, no. 10, pp. 1722–1743, 2005. DOI: 10.1109/JPROC.2005.853539.

[29] P. Hillger, "Silicon-based Systems for Microscopic and Volumetric Terahertz Imaging," Ph.D. dissertation, 2017. DOI: 10.25926/346h-5p75.

[30] G. Valušis, A. Lisauskas, H. Yuan, W. Knap, and H. G. Roskos, "Roadmap of Terahertz Imaging 2021," *Sens.*, vol. 21, no. 12, p. 4092, 2021.

[31] Q. Sun, Y. He, K. Liu, S. Fan, E. P. Parrott, and E. Pickwell-MacPherson, "Recent advances in terahertz technology for biomedical applications," *Quant. Imaging Med. Surg.*, vol. 7, no. 3, p. 345, 2017. DOI: 10.21037/qims.2017.06.02.

[32] P. Hillger, R. Jain, J. Grzyb, *et al.*, "A 128-Pixel System-on-a-Chip for Real-Time Super-Resolution Terahertz Near-Field Imaging," *IEEE J. Solid-State Circuits*, vol. 53, no. 12, pp. 3599–3612, 2018. DOI: 10.1109/JSSC.2018.2878817.

[33] Q. Cassar, A. Al-Ibadi, L. Mavarani, *et al.*, "Pilot study of freshly excised breast tissue response in the 300–600 GHz range," *Biomed. Opt. Express*, vol. 9, no. 7, pp. 2930–2942, 2018. DOI: 10.1364/BOE.9.002930.

[34] U. R. Pfeiffer, P. Hillger, R. Jain, *et al.*, "Ex vivo breast tumor identification: Advances toward a silicon-based terahertz near-field imaging sensor," *IEEE Microw. Mag.*, vol. 20, no. 9, pp. 32–46, 2019. DOI: 10.1109/MMM.2019.2922119.

[35] H. Lin, B. M. Fischer, S. P. Mickan, and D. Abbott, "Review of THz near-field methods," in *Smart Struct. Devices Syst. III*, International Society for Optics and Photonics, vol. 6414, 2007, p. 64140L. DOI: 10.1117/12.695309.

[36] A. J. L. Adam, "Review of Near-Field Terahertz Measurement Methods and Their Applications," *J. Infrared Millim. Terahertz Waves*, vol. 32, no. 8, pp. 976–1019, 2011. DOI: 10.1007/s10762-011-9809-2.

[37] B. M. Fischer, M. Walther, and P. U. Jepsen, "Far-infrared vibrational modes of DNA components studied by terahertz time-domain spectroscopy," *Phys. Med. Biol.*, vol. 47, no. 21, pp. 3807–3814, Oct. 2002. DOI: 10.1088/0031-9155/47/21/319.

[38] M. Walther, B. M. Fischer, and P. U. Jepsen, "Noncovalent intermolecular forces in polycrystalline and amorphous saccharides in the far infrared," *Chem. Phys.*, vol. 288, no. 2-3, pp. 261–268, 2003. DOI: 10.1016/S0301-0104(03)00031-4.

[39] H. Harde, R. Cheville, and D. Grischkowsky, "Terahertz Studies of Collision-Broadened Rotational Lines," *J. Phys. Chem. A*, vol. 101, no. 20, pp. 3646–3660, 1997. DOI: 10.1021/jp962974c.

[40] M. Naftaly and R. E. Miles, "Terahertz Time-Domain Spectroscopy for Material Characterization," *Proc. IEEE*, vol. 95, no. 8, pp. 1658–1665, 2007. DOI: 10.1109/JPROC.2007.898835.

[41] J. Barowski, J. Jebramcik, I. Alawneh, F. Sheikh, T. Kaiser, and I. Rolfes, "A Compact Measurement Setup for In-Situ Material Characterization in the Lower THz Range," in *Proc. Int. Worksh. Mob. Terahertz Syst.*, IEEE, 2019, pp. 1–5. DOI: 10.1109/IWMTS.2019.8823700.

[42] M. Van Exter, C. Fattinger, and D. Grischkowsky, "Terahertz time-domain spectroscopy of water vapor," *Opt. Lett.*, vol. 14, no. 20, pp. 1128–1130, 1989. DOI: 10.1364/OL.14.001128.

[43] P. F. Taday, I. Bradley, D. Arnone, and M. Pepper, "Using Terahertz Pulse Spectroscopy to Study the Crystalline Structure of a Drug: A Case Study of the Polymorphs of Ranitidine Hydrochloride," *J. Pharm. Sci.*, vol. 92, no. 4, pp. 831–838, 2003. DOI: 10.1002/jps.10358.

[44] J. Xu, K. W. Plaxco, and S. J. Allen, "Probing the collective vibrational dynamics of a protein in liquid water by terahertz absorption spectroscopy," *Protein Sci.*, vol. 15, no. 5, pp. 1175–1181, 2006. DOI: 10.1110/ps.062073506.

[45] D. J. Cook, B. K. Decker, and M. G. Allen, "Quantitative THz Spectroscopy of Explosive Materials," in *Optical Terahertz Science and Technology*, Optical Soc. Am., 2005, MA6. DOI: 10.1364/OTST.2005.MA6.

[46] A. G. Davies, A. D. Burnett, W. Fan, E. H. Linfield, and J. E. Cunningham, "Terahertz spectroscopy of explosives and drugs," *Mat. Today*, vol. 11, no. 3, pp. 18–26, 2008. DOI: 10.1016/S1369-7021(08)70016-6.

[47] H. Wu and M. Khan, "THz spectroscopy: An emerging technology for pharmaceutical development and pharmaceutical Process Analytical Technology (PAT) applications," *J. Mol. Struct.*, vol. 1020, pp. 112–120, 2012. DOI: 10.1016/j.molstruc.2012.04.019.

[48] V. Petrov, T. Kurner, and I. Hosako, "IEEE 802.15. 3d: First standardization efforts for sub-terahertz band communications toward 6G," *IEEE Communications Magazine*, vol. 58, no. 11, pp. 28–33, 2020. DOI: 10.1109/MCOM.001.2000273.

[49] K.-C. Huang and Z. Wang, "Terahertz Terabit Wireless Communication," *IEEE Commun. Mag.*, vol. 12, no. 4, pp. 108–116, 2011. DOI: 10.1109/MMM.2011.940596.

[50] J. Federici and L. Moeller, "Review of terahertz and subterahertz wireless communications," *J. Appl. Phys.*, vol. 107, no. 11, p. 6, 2010. DOI: 10.1063/1.3386413.

[51] H.-J. Song and T. Nagatsuma, "Present and Future of Terahertz Communications," *IEEE Trans. Terahertz Sci. Technol.*, vol. 1, no. 1, pp. 256–263, 2011. DOI: 10.1109/TTHZ.2011.2159552.

[52] B. Aazhang, P. Ahokangas, H. Alves, *et al.*, *KEY DRIVERS AND RESEARCH CHALLENGES FOR 6G UBIQUITOUS WIRELESS INTELLIGENCE*. Sep. 2019.

[53] P. Rodriguez-Vazquez, J. Grzyb, B. Heinemann, and U. R. Pfeiffer, "A QPSK 110-Gb/s Polarization-Diversity MIMO Wireless Link with a 220–255 GHz Tunable LO in a SiGe HBT Technology," *IEEE Trans. Microw. Theory Techn.*, vol. 68, no. 9, pp. 3834–3851, 2020. DOI: 10.1109/TMTT.2020.2986196.

[54] S. Jia, X. Pang, O. Ozolins, *et al.*, "0.4 THz Photonic-Wireless Link With 106 Gb/s Single Channel Bitrate," *J. Lightwave Technol.*, vol. 36, no. 2, pp. 610–616, Jan. 2018. DOI: 10.1109/JLT.2017.2776320.

[55] M. Kowalski, M. Kastek, M. Walczakowski, N. Palka, and M. Szustakowski, "Passive imaging of concealed objects in terahertz and long-wavelength infrared," *Appl. Opt.*, vol. 54, no. 13, pp. 3826–3833, 2015. DOI: 10.1364/AO.54.003826.

[56] D. T. Petkie, C. Casto, F. C. De Lucia, *et al.*, "Active and passive imaging in the THz spectral region: phenomenology, dynamic range, modes, and illumination," *JOSA B*, vol. 25, no. 9, pp. 1523–1531, 2008. DOI: 10.1364/JOSAB.25.001523.

[57] R. Lewis, "A review of terahertz detectors," *J. Phys. D Appl. Phys.*, vol. 52, no. 43, p. 433 001, 2019. DOI: 10.1088/1361-6463/ab31d5.

[58] S. Withington, "Terahertz astronomical telescopes and instrumentation," *Philos. Trans. Royal Soc. Lond. Ser. A: Mathematical, Phys. and Eng. Sci.*, vol. 362, no. 1815, pp. 395–402, 2004. DOI: 10.1098/rsta.2003.1322.

[59] G. Chattopadhyay, "Technology, Capabilities, and Performance of Low Power Terahertz Sources," *IEEE Trans. Terahertz Sci. Technol.*, vol. 1, no. 1, pp. 33–53, 2011. DOI: 10.1109/TTHZ.2011.2159561.

[60] S. Dhillon, M. Vitiello, E. Linfield, *et al.*, "The 2017 terahertz science and technology roadmap," *J. Phys. D*, vol. 50, no. 4, p. 043 001, 2017.

[61] C. Sirtori, "Bridge for the terahertz gap," *Nat.*, vol. 417, no. 6885, pp. 132–133, 2002. DOI: 10.1038/417132b.

[62] R. A. Lewis, "A review of terahertz sources," *J. Phys. D Appl. Phys.*, vol. 47, no. 37, p. 374 001, 2014. DOI: 10.1088/0022-3727/47/37/374001.

[63] L. Samoska, "Towards terahertz MMIC amplifiers: Present status and trends," in *IEEE MTT-S Int. Microw. Symp. Dig.*, IEEE, 2006, pp. 333–336. DOI: 10.1109/MWSYM.2006.249519.

[64] M. Urteaga, Z. Griffith, M. Seo, J. Hacker, and M. J. Rodwell, "InP HBT Technologies for THz Integrated Circuits," *Proc. IEEE*, vol. 105, no. 6, pp. 1051–1067, 2017. DOI: 10.1109/JPROC.2017.2692178.

[65] M. Schröter, T. Rosenbaum, P. Chevalier, *et al.*, "SiGe HBT Technology: Future Trends and TCAD-based Roadmap," *Proc. IEEE*, vol. 105, no. 6, pp. 1068–1086, 2016. DOI: 10.1109/JPROC.2015.2500024.

[66] B. Heinemann, H. Rücker, R. Barth, *et al.*, "SiGe HBT with fx/fmax of 505 GHz/720 GHz," in *2016 IEEE International Electron Devices Meeting (IEDM)*, IEEE, 2016, pp. 3–1. DOI: 10.1109/IEDM.2016.7838335.

[67] V. d. N. Rinaldi and I. Marano, "Towards 0.5 Terahertz Silicon/Germanium Heterojunction Bipolar Technology-Internal Report of DotFive Project," *DOTFIVE–WP I–D1. 3.3, Development of a thermal resistance roadmap*, 2009.

[68] R. Lachner, "Towards 0.7 Terahertz Silicon Germanium Heterojunction Bipolar Technology – The DOTSEVEN Project," *ECS Trans.*, vol. 64, no. 6, p. 21, Aug. 2014. DOI: 10.1149/06406.0021ecs.

[69] P. Hillger, J. Grzyb, R. Jain, and U. R. Pfeiffer, "Terahertz Imaging and Sensing Applications With Silicon-Based Technologies," *IEEE Trans. Terahertz Sci. Technol.*, vol. 9, no. 1, pp. 1–19, 2019. DOI: 10.1109/TTHZ.2018.2884852.

[70] X. Yi, C. Wang, Z. Hu, *et al.*, "Emerging Terahertz Integrated Systems in Silicon," *IEEE Trans. Circuits Syst. I Regul. Pap.*, 2021. DOI: 10.1109/TCSI.2021.3087604.

[71] K. Sengupta, T. Nagatsuma, and D. M. Mittleman, "Terahertz integrated electronic and hybrid electronic–photonic systems," *Nat. Electron.*, vol. 1, no. 12, pp. 622–635, 2018. DOI: 10.1038/s41928-018-0173-2.

[72] S. H. Naghavi, M. T. Taba, R. Han, M. A. Aseeri, A. Cathelin, and E. Afshari, "Filling the Gap With Sand," *IEEE Solid-State Circuits Mag.*, vol. 11, no. 3, pp. 33–42, 2019. DOI: 10.1109/MSSC.2019.2922888.

[73] T. Hartwick, D. Hodges, D. Barker, and F. Foote, "Far infrared imagery," *Appl. Opt.*, vol. 15, no. 8, pp. 1919–1922, 1976. DOI: 10.1364/AO.15.001919.

[74] S. Malz, R. Jain, and U. R. Pfeiffer, "Towards Passive Imaging with CMOS THz Cameras," in *Proc. Int. Conf. Infrared Millim. Terahertz Waves*, Copenhagen, Denmark, Sep. 2016, pp. 1–2. DOI: 10.1109/IRMMW-THz.2016.7758858.

[75] R. Jain, J. Grzyb, and U. R. Pfeiffer, "Terahertz Light-Field Imaging," *IEEE Trans. Terahertz Sci. Technol.*, vol. 6, no. 5, pp. 649–657, 2016. DOI: 10.1109/TTHZ.2016.2584861.

[76] R. Jain, F. Landskron, J. Grzyb, and U. R. Pfeiffer, "Object Feature Extraction with Focused Terahertz Plenoptic Imaging," in *Proc. Int. Conf. Infrared Millim. Terahertz Waves*, Nagoya, Japan, pp. 1–2. DOI: 10.1109/IRMMW-THz.2018.8509974.

[77] R. Jain, M. Schellenbeck, J. Grzyb, and U. R. Pfeiffer, "Investigations on the plenoptics based image generation for THz reflection imaging," in *Proc. Int. Conf. Infrared Millim. Terahertz Waves*, Cancun, Mexico, Aug. 2017, pp. 1–2. DOI: 10.1109/IRMMW-THz.2017.8067173.

[78] R. Al Hadi, J. Lampin, and U. R. Pfeiffer, "A Real-Time Terahertz Beam Monitoring Application with a l024-pixel CMOS Terahertz Camera Module," in *Proc. Conf. Lasers Electro-Optics - Laser Sci. Photonic Appl.*, Jun. 2014. DOI: 10.1364/CLEO_AT.2014.JTu4A.107.

[79] J. Zdanevičius, M. Bauer, S. Boppel, *et al.*, "Camera for High-Speed THz Imaging," *J. Infrared Millim. Terahertz Waves*, vol. 36, no. 10, pp. 986–997, 2015. DOI: 10.1007/s10762-015-0169-1.

[80] S. Yokoyama, M. Ikebe, Y. Kanazawa, *et al.*, "5.8 A 32×32-Pixel 0.9THz Imager with Pixel-Parallel 12b VCO-Based ADC in 0.18µm CMOS," in *Proc. IEEE Int. Solid-State Circ. Conf.*, IEEE, San Francisco, CA, USA, 2019, pp. 108–110. DOI: 10.1109/ISSCC.2019.8662483.

[81] N. Oda, "Uncooled bolometer-type terahertz focal plane array and camera for real-time imaging," *C. R. Phys.*, vol. 11, no. 7-8, pp. 496–509, 2010. DOI: 10.1016/j.crhy.2010.05.001.

[82] C. Chevalier, F. Duchesne, L. Gagnon, *et al.*, "Introducing a 384x288 Pixel Terahertz Camera Core," in *Proc. Terahertz RF Millim. Submillimeter-Wave Techn. Appl. VI*, International Society for Optics and Photonics, vol. 8624, San Francisco, CA, USA, 2013, pp. 1–8. DOI: 10.1117/12.2002699.

[83] F. Simoens, J. Meilhan, and J.-A. Nicolas, "Terahertz Real-Time Imaging Uncooled Arrays Based on Antenna-Coupled Bolometers or FET Developed at CEA-Leti," *J. Infrared Millim. Terahertz Waves*, vol. 36, no. 10, pp. 961–985, 2015. DOI: 10.1007/s10762-015-0197-x.

[84] G. Steinfeld, C. Brodeur, M. Shalaby, and G. Santiso, "RIGI Camera for Real Time Ultrasensitive Terahertz Imaging," in *Proc. Int. Conf. Infrared Millim. Terahertz Waves*, IEEE, Paris, France, 2019, p. 1. DOI: 10.1109/IRMMW-THz.2019.8874087.

[85] i2S, *Imaging Solutions*, https://www.i2s.fr/en/imaging-solutions/specific-cameras-for-the-visible-and-invisible/tzcam.

[86] N. Oda, S. Kurashina, M. Miyoshi, *et al.*, "Microbolometer Terahertz Focal Plane Array and Camera with Improved Sensitivity in the Sub-Terahertz Region," *J. Infrared Millim. Terahertz Waves*, vol. 36, no. 10, pp. 947–960, 2015. DOI: 10.1007/s10762-015-0184-2.

[87] F. Simoens and J. Meilhan, "Terahertz real-time imaging uncooled array based on antenna-and cavity-coupled bolometers," *Philos. Trans. Royal Soc. Lond. Ser. A: Mathematical, Phys. and Eng. Sci.*, vol. 372, no. 2012, pp. 1–12, 2014. DOI: 10.1098/rsta.2013.0111.

[88] H. Oulachgar, P. Mauskopf, M. Bolduc, *et al.*, "Design and Microfabrication of Frequency Selective Uncooled Microbolometer Focal Plane Array for Terahertz Imaging," in *Proc. Int. Conf. Infrared Millim. Terahertz Waves*,

IEEE, Mainz, Germany, 2013, pp. 1–2. DOI: 10.1109/IRMMW-THz.2013.6665501.

[89] I. Escorcia Carranza, J. P. Grant, J. Gough, and D. Cumming, "Terahertz Metamaterial Absorbers Implemented in CMOS Technology for Imaging Applications: Scaling to Large Format Focal Plane Arrays," *IEEE J. Sel. Top. Quantum Electron.*, vol. 23, no. 4, pp. 1–8, 2017. DOI: 10.1109/JSTQE.2016.2630307.

[90] C. M. Armstrong, "The Truth About Terahertz," *IEEE Spectr.*, vol. 49, no. 9, pp. 36–41, 2012. DOI: 10.1109/MSPEC.2012.6281131.

[91] R. Han, C. Jiang, A. Mostajeran, *et al.*, "A SiGe Terahertz Heterodyne Imaging Transmitter With 3.3 mW Radiated Power and Fully-Integrated Phase-Locked Loop," *IEEE J. Solid-State Circuits*, vol. 50, no. 12, pp. 2935–2947, Feb. 2015. DOI: 10.1109/JSSC.2015.2471847.

[92] Y. Tousi and E. Afshari, "14.6 A scalable THz 2D phased array with +17dBm of EIRP at 338GHz in 65nm bulk CMOS," in *Proc. IEEE Int. Solid-State Circ. Conf. Dig. Techn. Papers*, San Francisco, CA, USA, Feb. 2014, pp. 258–259. DOI: 10.1109/ISSCC.2014.6757425.

[93] F. Golcuk, O. D. Gurbuz, and G. M. Rebeiz, "A 0.39–0.44 THz 2x4 Amplifier-Quadrupler Array With Peak EIRP of 3–4 dBm," *IEEE Trans. Microw. Theory Techn.*, vol. 61, no. 12, pp. 4483–4491, 2013. DOI: 10.1109/TMTT.2013.2287493.

[94] Z. Hu, M. Kaynak, and R. Han, "High-Power Radiation at 1 THz in Silicon: A Fully Scalable Array Using a Multi-Functional Radiating Mesh Structure," *IEEE J. Solid-State Circuits*, vol. 53, no. 5, pp. 1313–1327, 2018. DOI: 10.1109/JSSC.2017.2786682.

[95] G. Guimaraes and P. Reynaert, "29.6 A 660-to-676GHz 4×2 Oscillator-Radiator Array with Intrinsic Frequency-Filtering Feedback for Harmonic Power Boost Achieving 7.4dBm EIRP in 40nm CMOS," in *Proc. IEEE Int. Solid-State Circ. Conf.*, San Francisco, CA, USA, 2020. DOI: 10.1109/ISSCC19947.2020.9063037.

[96] H. Saeidi, S. Venkatesh, C. R. Chappidi, T. Sharma, C. Zhu, and K. Sengupta, "29.9 A 4×4 Distributed Multi-Layer Oscillator Network for Harmonic Injection and THz Beamforming with 14dBm EIRP at 416GHz in a Lensless 65nm CMOS IC," in *Proc. IEEE Int. Solid-State Circ. Conf.*, San

Francisco, CA, USA, Feb. 2020, pp. 256–258. DOI: 10.1109/ISSCC19947.2020.9063076.

[97] H. Jalili and O. Momeni, "A 0.46-THz 25-element scalable and wideband radiator array with optimized lens integration in 65-nm CMOS," *IEEE J. Solid-State Circuits*, vol. 55, no. 9, pp. 2387–2400, 2020. DOI: 10.1109/JSSC.2020.2989897.

[98] K. Guo and P. Reynaert, "29.2 A 0.59THz Beam-Steerable Coherent Radiator Array with 1mW Radiated Power and 24.1dBm EIRP in 40nm CMOS," in *Proc. IEEE Int. Solid-State Circ. Conf.*, San Francisco, CA, USA, Feb. 2020, pp. 442–444. DOI: 10.1109/ISSCC19947.2020.9063139.

[99] R. Jain, P. Hillger, J. Grzyb, and U. R. Pfeiffer, "29.1 A 0.42THz 9.2dBm 64-Pixel Source-Array SoC with Spatial Modulation Diversity for Computational Terahertz Imaging," in *Proc. IEEE Int. Solid-State Circ. Conf.*, San Francisco, CA, USA, Feb. 2020, pp. 440–442. DOI: 10.1109/ISSCC19947.2020.9063025.

[100] K. Kasagi, S. Suzuki, and M. Asada, "Large-scale array of resonant-tunneling-diode terahertz oscillators for high output power at 1 THz," *J. Appl. Phys.*, vol. 125, no. 15, pp. 1–7, 2019. DOI: 10.1063/1.5051007.

[101] N. Shimizu, K. Matsuyama, and H. Uchida, "Incoherent sub-terahertz radiation source with a photomixer array for active imaging in smoky environments," in *Proc. Terahertz RF Millim. Submillimeter-Wave Techn. Appl. VI*, San Francisco, CA, USA, 2015, pp. 1–8. DOI: 10.1117/12.2076095.

[102] K. B. Cooper, R. J. Dengler, N. Llombart, B. Thomas, G. Chattopadhyay, and P. H. Siegel, "THz Imaging Radar for Standoff Personnel Screening," *IEEE Trans. Terahertz Sci. Technol.*, vol. 1, no. 1, pp. 169–182, 2011. DOI: 10.1109/TTHZ.2011.2159556.

[103] S. Islam, J. Stiens, G. Poesen, I. Jaeger, and R. Vounckx, "Passive frequency selective surface array as a diffuser for destroying millimeter wave coherence," *Act. Passiv. Electron. Compon.*, vol. 2008, 2008. DOI: 10.1155/2008/391745.

[104] T. H. Buttgenbach, "An Improved Solution for Integrated Array Optics in Quasi-Optical mm and Submm Receivers: the Hybrid Antenna," *IEEE Trans. Microw. Theory Techn.*, vol. 41, no. 10, pp. 1750–1760, 1993. DOI: 10.1109/22.247920.

[105] D. F. Filipovic, S. S. Gearhart, and G. M. Rebeiz, "Double-Slot Antennas on Extended Hemispherical and Elliptical Silicon Dielectric Lenses," *IEEE Trans. Microw. Theory Techn.*, vol. 41, no. 10, pp. 1738–1749, 1993. DOI: 10.1109/22.247919.

[106] A. Karttunen, J. Ala-Laurinaho, R. Sauleau, and A. V. Räisänen, "A Study of Extended Hemispherical Lenses for a High-Gain Beam-Steering Antenna," in *Proc. Eur. Conf. Antennas Propag.*, IEEE, Barcelona, Spain, 2010.

[107] D. F. Filipovic, G. P. Gauthier, S. Raman, and G. M. Rebeiz, "Off-Axis Properties of Silicon and Quartz Dielectric Lens Antennas," *IEEE Trans. Antennas Propag.*, vol. 45, no. 5, pp. 760–766, 1997. DOI: 10.1109/8.575618.

[108] A. V. Boriskin and R. Sauleau, "Drastic influence of the half-bowtie resonances on the focusing and collimating capabilities of 2-D extended hemielliptical and hemispherical dielectric lenses," *J. Opt. Soc. Am.*, vol. 27, no. 11, pp. 2442–2449, 2010. DOI: 10.1364/JOSAA.27.002442.

[109] A. V. Boriskin, R. Sauleau, and A. I. Nosich, "Performance of Hemielliptic Dielectric Lens Antennas With Optimal Edge Illumination," *IEEE Trans. Antennas Propag.*, DOI: 10.1109/TAP.2009.2021979.

[110] D. B. Rutledge, D. P. Neikirk, and D. P. Kasilingam, "Integrated circuit antennas," *Infrared Millim. Waves*, vol. 10, no. 2, pp. 1–90, 1983.

[111] D. Liu, U. Pfeiffer, J. Grzyb, and B. Gaucher, *Advanced millimeter-wave technologies: antennas, packaging and circuits*. John Wiley & Sons, 2009.

[112] Y. Nishida, N. Nishigami, S. Diebold, J. Kim, M. Fujita, and T. Nagatsuma, "Terahertz coherent receiver using a single resonant tunnelling diode," *Sci. Rep.*, vol. 9, no. 18125, pp. 1–9, 2019. DOI: 10.1038/s41598-019-54627-8.

[113] L. Liebermeister, S. Nellen, R. Kohlhaas, S. Breuer, M. Schell, and B. Globisch, "Ultra-fast, High-Bandwidth Coherent cw THz Spectrometer for Non-destructive Testing," *J. Infrared Millim. Terahertz Waves*, vol. 40, no. 3, pp. 288–296, 2019. DOI: 10.1007/s10762-018-0563-6.

[114] R. Al Hadi, J. Grzyb, B. Heinemann, and U. R. Pfeiffer, "A Terahertz Detector Array in a SiGe HBT Technology," *IEEE J. Solid-State Circuits*, vol. 48, no. 9, pp. 2002–2010, 2013. DOI: 10.1109/JSSC.2013.2265493.

[115] M. Andree, J. Grzyb, R. Jain, B. Heinemann, and U. R. Pfeiffer, "A Broadband Dual-Polarized Terahertz Direct Detector in a 0.13-µm SiGe HBT Technology," in *Proc. IEEE MTT-S Int. Microw. Symp.*, Boston, MA, USA, 2019, pp. 500–503. DOI: 10.1109/MWSYM.2019.8700871.

[116] M. Andree, J. Grzyb, R. Jain, B. Heinemann, and U. R. Pfeiffer, "A Broadband Antenna-Coupled Terahertz Direct Detector in a 0.13-µm SiGe HBT Technology," in *Proc. Eur. Microw. Integr. Circuits Conf.*, Paris, France, 2019, pp. 168–171. DOI: 10.23919/EuMIC.2019.8909399.

[117] J. Grzyb, M. Andree, R. Jain, B. Heinemann, and U. R. Pfeiffer, "A Lens-Coupled On-Chip Antenna for Dual-Polarization SiGe HBT THz Direct Detector," *IEEE Antennas Wirel. Propag. Lett.*, vol. 18, no. 11, pp. 2404–2408, 2019. DOI: 10.1109/LAWP.2019.2927300.

[118] H. Frid, "Closed-Form Relation Between the Scan Angle and Feed Position for Extended Hemispherical Lenses Based on Ray Tracing," *Appl. Phys. Lett.*, vol. 15, pp. 1963–1966, 2016. DOI: 10.1109/LAWP.2016.2545858.

[119] Z. Wang and A. C. Bovik, "MODERN IMAGE QUALITY ASSESSMENT," *Synthesis Lectures on Image, Video, and Multimedia Processing*, vol. 2, no. 1, pp. 1–156, 2006. DOI: 10.2200/S00010ED1V01Y200508IVM003.

[120] W. J. Smith *et al.*, *Modern lens design*. McGraw-Hill New York, NY, USA, 2005, vol. 2.

[121] W. J. Smith and W. Smith, *Modern optical engineering*. Mcgraw-hill New York, 1966, vol. 3.

[122] M. J. Nasse and J. C. Woehl, "Realistic modeling of the illumination point spread function in confocal scanning optical microscopy," *J. Opt. Soc. Am. A*, vol. 27, no. 2, pp. 295–302, Feb. 2010. DOI: 10.1364/JOSAA.27.000295.

[123] S. W. Smith *et al.*, "The scientist and engineer's guide to digital signal processing," *California Technical Pub. San Diego*, 1997.

[124] B. Tatian, "Method for Obtaining the Rransfer Function from the Edge Response Function," *J. Opt. Soc. Am.*, vol. 55, no. 8, pp. 1014–1019, 1965. DOI: 10.1364/JOSA.55.001014.

[125] C. A. Balanis, *Antenna theory: analysis and design*. John wiley & sons, 2016.

[126] J. Grzyb, K. Statnikov, N. Sarmah, B. Heinemann, and U. R. Pfeiffer, "A 210–270-GHz Circularly Polarized FMCW Radar With a Single-Lens-Coupled SiGe HBT Chip," *IEEE Trans. Terahertz Sci. Technol.*, vol. 6, no. 6, pp. 771–783, 2016. DOI: 10.1109/TTHZ.2016.2602539.

[127] B. Huang, H. Babcock, and X. Zhuang, "Breaking the diffraction barrier: Super-resolution imaging of cells," *Cell*, vol. 143, no. 7, pp. 1047–1058, 2010. DOI: 10.1016/j.cell.2010.12.002.

[128] A. Borkowski *et al.*, "Geometrical superresolved imaging using nonperiodic spatial masking," *J. Opt. Soc. Am.*, vol. 26, no. 3, pp. 589–601, 2009. DOI: 10.1364/JOSAA.26.000589.

[129] C. Dong, C. C. Loy, and X. Tang, "Accelerating the Super-Resolution Convolutional Neural Network," in *Proc. Eur. Conf. Computer Visions*, Springer, 2016, pp. 391–407. DOI: 10.1007/978-3-319-46475-6_25.

[130] C. Qiao, D. Li, Y. Guo, *et al.*, "Evaluation and development of deep neural networks for image super-resolution in optical microscopy," *Nat. Methods*, vol. 18, no. 2, pp. 194–202, 2021. DOI: 10.1038/s41592-020-01048-5.

[131] L. Fang, F. Monroe, S. W. Novak, *et al.*, "Deep learning-based point-scanning super-resolution imaging," *Nat. Methods*, vol. 18, no. 4, pp. 406–416, 2021. DOI: 10.1038/s41592-021-01080-z.

[132] R. Hook and A. Fruchter, "Dithering, sampling and image reconstruction," in *Astronomical Data Analysis Software and Systems IX*, vol. 216, 2000, p. 521.

[133] M. Honma, K. Akiyama, M. Uemura, and S. Ikeda, "Super-resolution imaging with radio interferometry using sparse modeling," *Publ. Astron. Soc. Jpn.*, vol. 66, no. 5, p. 95, 2014. DOI: 10.1093/pasj/psu070.

[134] K. Akiyama, A. Alberdi, W. Alef, *et al.*, "First M87 event horizon telescope results. IV. Imaging the central supermassive black hole," *Astrophys. J. Lett.*, vol. 875, no. 1, p. L4, 2019.

[135] J. A. Kennedy *et al.*, "Improved Image Fusion in PET/CT Using Hybrid Image Reconstruction and Super-Resolution," *Int. J. Biomed. Imaging*, vol. 2007, 2007. DOI: 10.1155/2007/46846.

[136] P. An, J. Ma, T. Ma, *et al.*, "Two-point calibration method for a zoom camera with an approximate focal-invariant radial distortion model," *JOSA A*, vol. 38, no. 4, pp. 504–514, 2021. DOI: 10.1364/JOSAA.414504.

[137] K. Liao, C. Lin, Y. Zhao, and M. Gabbouj, "DR-GAN: Automatic Radial Distortion Rectification Using Conditional GAN in Real-Time," *IEEE Trans. Circuits Syst. Video Technol.*, vol. 30, no. 3, pp. 725–733, 2020. DOI: 10.1109/TCSVT.2019.2897984.

[138] J. Grzyb, H. Sherry, Y. Zhao, *et al.*, "Real-time video rate imaging with a 1k-pixel THz CMOS focal plane array," *Proc. Terahertz, RF Millim. Submillimeter-Wave Techn. Appl. VI*, vol. 8362, pp. 1–12, May 2012. DOI: 10.1117/12.919218.

[139] U. R. Pfeiffer, Y. Zhao, J. Grzyb, *et al.*, "14.5 A 0.53THz Reconfigurable Source Array with up to 1mW Radiated Power for Terahertz Imaging Applications in 0.13µm SiGe BiCMOS," in *Proc. IEEE Int. Solid-State Circ. Conf.*, San Francisco, CA, USA, 2014, pp. 256–257. DOI: 10.1109/ISSCC.2014.6757424.

[140] M. C. Beard, G. M. Turner, and C. A. Schmuttenmaer, *Terahertz Spectroscopy*, 2002. DOI: 10.1021/jp020579i.

[141] J. B. Baxter and G. W. Guglietta, "Terahertz Spectroscopy," *Anal. Chem.*, vol. 83, no. 12, pp. 4342–4368, 2011. DOI: 10.1021/ac200907z.

[142] S. L. Dexheimer, *Terahertz Spectroscopy: PRINCIPLES AND APPLICATIONS*. CRC press, 2017. DOI: 10.1201/9781420007701.

[143] K. Schmalz, J. Borngräber, W. Debski, P. Neumaier, R. Wang, and H. Hübers, "Tunable 500 GHz transmitter array in SiGe technology for gas spectroscopy," *Electron. Lett.*, vol. 51, no. 3, pp. 257–259, 2015. DOI: 10.1049/el.2014.4174.

[144] K. Schmalz, J. Borngräber, W. Debski, *et al.*, "245-GHz Transmitter Array in SiGe BiCMOS for Gas Spectroscopy," *IEEE Trans. Terahertz Sci. Technol.*, vol. 6, no. 2, pp. 318–327, 2016. DOI: 10.1109/TTHZ.2015.2513278.

[145] K. Schmalz, N. Rothbart, A. Glück, *et al.*, "Dual-Band Transmitter and Receiver With Bowtie-Antenna in 0.13 µm SiGe BiCMOS for Gas Spectroscopy at 222 - 270 GHz," *IEEE Access*, vol. 9, pp. 124 805–124 816, 2021. DOI: 10.1109/ACCESS.2021.3110210.

[146] K. Statnikov, J. Grzyb, B. Heinemann, and U. R. Pfeiffer, "160-GHz to 1-THz Multi-Color Active Imaging with a Lens-Coupled SiGe HBT Chip-Set," *IEEE Trans. Microw. Theory Techn.*, vol. 63, no. 2, pp. 520–532, 2015. DOI: 10.1109/TMTT.2014.2385777.

[147] S. Razavian and A. Babakhani, "Silicon Integrated THz Comb Radiator and Receiver for Broadband Sensing and Imaging Applications," *IEEE Trans. Microw. Theory Tech.*, 2021. DOI: 10.1109/TMTT.2021.3105436.

[148] S. Razavian, M. Hosseini, Y. Mehta, and A. Babakhani, "Terahertz Channel Characterization Using a Broadband Frequency Comb Radiator in 130-Nm SiGe BiCMOS," *IEEE Trans. Terahertz Sci. Technol.*, vol. 11, no. 3, pp. 269–276, 2021. DOI: 10.1109/TTHZ.2021.3059335.

[149] X. Wu and K. Sengupta, "On-Chip THz Spectroscope Exploiting Electromagnetic Scattering With Multi-Port Antenna," *IEEE J. Solid-State Circuits*, vol. 51, no. 12, pp. 3049–3062, 2016. DOI: 10.1109/JSSC.2016.2597845.

[150] X. Wu and K. Sengupta, "Single-chip source-free terahertz spectroscope across 0.04–0.99 THz: combining sub-wavelength near-field sensing and regression analysis," *Opt. Express*, vol. 26, no. 6, pp. 7163–7175, 2018. DOI: 10.1364/OE.26.007163.

[151] M. M. Assefzadeh and A. Babakhani, "Broadband Oscillator-Free THz Pulse Generation and Radiation Based on Direct Digital-to-Impulse Architecture," *IEEE J. Solid-State Circuits*, vol. 52, no. 11, pp. 2905–2919, Nov. 2017. DOI: 10.1109/JSSC.2017.2739180.

[152] L. E. Marchese, M. Terroux, M. Bolduc, *et al.*, "A 0.1 Megapixel THz Camera with 17 Degree Field of View for Large Area Single Shot Imaging," in *Proc. Int. Conf. Infrared Millim. Terahertz Waves*, Tucson, AZ, USA, 2014, pp. 1–2. DOI: 10.1109/IRMMW-THz.2014.6956039.

[153] D. Corcos, N. Kaminski, E. Shumaker, *et al.*, "Antenna-Coupled MOSFET Bolometers for Uncooled THz Sensing," *IEEE Trans. Terahertz Sci. Technol.*, vol. 5, no. 6, pp. 902–913, 2015. DOI: 10.1109/TTHZ.2015.2466470.

[154] R. Han, Y. Zhang, Y. Kim, *et al.*, "Active Terahertz Imaging Using Schottky Diodes in CMOS: Array and 860-GHz Pixel," *IEEE J. Solid-State Circuits*, vol. 48, no. 10, pp. 2296–2308, 2013. DOI: 10.1109/JSSC.2013.2269856.

[155] R. Eichholz, H. Richter, S. Pavlov, *et al.*, "Multi-channel terahertz grating spectrometer with quantum-cascade laser and microbolometer array," *Appl. Phys. Lett.*, vol. 99, no. 14, p. 141 112, 2011. DOI: 10.1063/1.3645635.

[156] N. Kanda, K. Konishi, N. Nemoto, K. Midorikawa, and M. Kuwata-Gonokami, "Real-time broadband terahertz spectroscopic imaging by using a high-sensitivity terahertz camera," *Sci. Rep.*, vol. 7, p. 42 540, 2017. DOI: 10.1038/srep42540.

[157] D. T. Paris and F. K. Hurd, *Basic electromagnetic theory*. McGraw-Hill Companies, 1969.

[158] R. C. Johnson, H. A. Ecker, and J. S. Hollis, "Determination of far-field antenna patterns from near-field measurements," *Proc. IEEE*, vol. 61, no. 12, pp. 1668–1694, 1973. DOI: 10.1109/PROC.1973.9358.

[159] M. Coulombe, T. Ferdinand, T. Horgan, R. Giles, and J. Waldman, "A 585 GHZ COMPACT RANGE FOR SCALE MODEL RCS MEASUREMENTS," Tech. Rep., 1993.

[160] J. R. Mentzer, "The Use of Dielectric Lenses in Reflection Measurements," *Proc. IRE*, vol. 41, no. 2, pp. 252–256, 1953. DOI: 10.1109/JRPROC.1953.274215.

[161] A. Olver and A. Saleeb, "LENS-TYPE COMPACT ANTENNA RANGE," *Electron. Lett.*, vol. 15, no. 14, pp. 409–410, 1979. DOI: 10.1049/el:19790293.

[162] T. Hirvonen, J. Tuovinen, and A. Raisanen, "LENS-TYPE COMPACT ANTENNA TEST RANGE AT MM-WAVES," in *Proc. Eur. Microw. Conf.*, IEEE, vol. 2, Stuttgart, Germany, 1991, pp. 1079–1083. DOI: 10.1109/EUMA.1991.336489.

[163] J. Tuovinen, "Method for Testing Reflector Antennas at THz Frequencies," *IEEE Antennas Propag. M.*, vol. 35, no. 6, pp. 7–13, 1993. DOI: 10.1109/74.248479.

[164] J. Hakli, T. Koskinen, A. Lonnqvist, *et al.*, "Testing of a 1.5-m reflector antenna at 322 GHz in a CATR based on a hologram," *IEEE Trans. Antennas Propag.*, vol. 53, no. 10, pp. 3142–3150, 2005. DOI: 10.1109/TAP.2005.856343.

[165] A. Karttunen, J. Ala-Laurinaho, M. Vaaja, *et al.*, "Antenna Tests With a Hologram-Based CATR at 650 GHz," *IEEE Trans. Antennas Propag.*, vol. 57, no. 3, pp. 711–720, 2009. DOI: 10.1109/TAP.2009.2013428.

[166] C. Liu and X. Wang, "Design and Test of a 0.3 THz Compact Antenna Test Range," *Prog. Electromagn. Res.*, vol. 70, pp. 81–87, 2017. DOI: 10.2528/PIERL17080504.

[167] A. V. Räisänen, J. Ala-Laurinaho, A. Karttunen, J. Mallat, A. Tamminen, and M. Vaaja, "Measurements of high-gain antennas at THz frequencies," in *Proc. Eur. Conf. Antennas Propag.*, Barcelona, Spain, 2010, pp. 1–3.

[168] M. S. Neiman, "The Principle of Reciprocity in Antenna Theory," *Proc. IRE*, vol. 31, no. 12, pp. 666–671, 1943. DOI: 10.1109/JRPROC.1943.233683.

[169] C. A. Balanis, *Modern antenna handbook*. John Wiley & Sons, 2011.

[170] J. S. Lim, "Two-dimensional signal and image processing," *Englewood Cliffs*, 1990.

[171] S. Preu, C. Müller-Landau, S. Malzer, *et al.*, "Fiber-Coupled 2-D ni-pn-ip Superlattice Photomixer Array," *IEEE Trans. Antennas Propag.*, vol. 65, no. 7, pp. 3474–3480, 2017. DOI: 10.1109/TAP.2017.2700039.

[172] Z. Zhenrong, H. Xiang, and L. Xu, "Freeform surface lens for LED uniform illumination," *Appl. Opt.*, vol. 48, no. 35, pp. 6627–6634, Dec. 2009. DOI: 10.1364/AO.48.006627.

[173] Y. Ding, X. Liu, Z.-r. Zheng, and P.-f. Gu, "Freeform LED lens for uniform illumination," *Opt. Express*, vol. 16, no. 17, pp. 12 958–12 966, Aug. 2008. DOI: 10.1364/OE.16.012958.

[174] Z. Su, D. Xue, and Z. Ji, "Designing LED array for uniform illumination distribution by simulated annealing algorithm," *Opt. Express*, vol. 20, no. S6, A843–A855, Nov. 2012. DOI: 10.1364/OE.20.00A843.

[175] A. J.-W. Whang, Y.-Y. Chen, and Y.-T. Teng, "Designing Uniform Illumination Systems by Surface-Tailored Lens and Configurations of LED Arrays," *J. Display Technol.*, vol. 5, no. 3, pp. 94–103, May 2009.

[176] Z.-m. Zhu, X.-h. Qu, G.-x. Jia, and J.-f. Ouyang, "Uniform Illumination Design by Configuration of LED Array and Diffuse Reflection Surface for Color Vision Application," *J. Display Technol.*, vol. 7, no. 2, pp. 84–89, Feb. 2011.

[177] D. Ramane and A. Shaligram, "Optimization of multi-element LED source for uniform illumination of plane surface," *Opt. Express*, vol. 19, no. S4, A639–A648, Jul. 2011. DOI: 10.1364/OE.19.00A639.

[178] N. H. Vu, T. T. Pham, and S. Shin, "LED Uniform Illumination Using Double Linear Fresnel Lenses for Energy Saving," *Energies*, vol. 10, no. 12, 2017. DOI: 10.3390/en10122091.

[179] Z. Zhao, H. Zhang, H. Zheng, and S. Liu, "New reversing freeform lens design method for LED uniform illumination with extended source and near field," *Opt. Commun.*, vol. 410, pp. 123–129, 2018. DOI: 10.1016/j.optcom.2017.09.101.

[180] Z.-M. Zhu, J. Yuan, X. Sun, B. Peng, X. Xu, and Q.-X. Liu, "LED diffused transmission freeform surface design for uniform illumination," *J. Opt.*, vol. 48, no. 2, pp. 232–239, 2019. DOI: 10.1007/s12596-018-0505-7.

[181] H.-l. Zhang, L. Peng, Y.-k. Luo, and S. Yu, "Rectangular illumination method using LED arrays for machine vision," *Appl. Opt.*, vol. 59, no. 11, pp. 3518–3525, Apr. 2020. DOI: 10.1364/AO.384833.

[182] L. Xu, C. C. Ming, Y. Li, *et al.*, "Uniform Illumination Realized by Large Viewing Angle of Gallium Nitride-Based Mini-LED Chip With Translucent Sublayer Pairs," *IEEE Access*, vol. 9, pp. 74 713–74 718, 2021. DOI: 10.1109/ACCESS.2021.3074653.